Structural Study of Two-dimensional Semiconductors Using Four-dimensional Scanning Transmission Electron Microscopy

Yi Wen

Supervised by Professor Jamie H. Warner



Submitted in conformity with the requirements

For the degree of DPhil in Materials Science

Department of Materials

St Cross College

University of Oxford

November 2021

Copyright © 2021 by Yi Wen

Declaration

The material contained within this thesis has not previously been submitted for a degree at the University of Oxford or any other university. The research reported within this thesis has been conducted by the author unless indicated otherwise.

Copyright Notice

The copyright of this thesis rests with the author. No quotation from it should be published without the prior written consent of the author, and any information derived from it should be acknowledged.

Abstract

Structural Study of Two-dimensional Semiconductors Using Four-dimensional Scanning Transmission Electron Microscopy

Yi Wen
St cross College, University of Oxford
Michaelmas term, 2021
Thesis submitted for the degree of Doctor of Philosophy

Graphene has shown superior mechanical properties, electronic and thermal conductivity, and room temperature quantum hall effect that enables its wide application in nanoelectronics. Due to its gapless feature, other two-dimensional (2D) materials like transition metal dichalcogenides (TMDs) have drawn attention and have been extensively studied for their application in optoelectronics and photonics. However, the atomic defect structures brought in during synthesis will affect these properties and thus a thorough understanding is needed. 4D-STEM is a characterization method that captures the convergent beam electron diffraction (CBED) pattern to allow post-acquisition reconstruction including orientation and strain mapping, position averaged CBED, and ptychography. This doctoral project focused on using 4D-STEM to characterize graphene, MoS_2, and WS_2 with atomic defective structures by producing a series of maps of the local electronic environment with atomic resolution.

Monolayer MoS_2 and WS_2 were first investigated to form the basis of this project. The projected electric field map was first extracted since it is linearly proportional to the centre of mass shift of the CBED pattern caused by the atomic electric field, which can then be used to calculate the charge density map and electrostatic potential. Simple defective structures were subsequently investigated, leading to a detailed study of the enhanced electric field on TMD zigzag edges and MoS nanowire. Next,

more complex structures, bilayer and trilayer twisted graphene were investigated. The electric field map showed that the bilayer with a large twist angle of 28.4° has decoupled based on comparison between the independent atom model (IAM) simulation and experimental results. A study on a backfolded trilayer further showed that, even though the top and bottom layer have a small twist angle of 3°, they show no strong interlayer coupling in the electric field due to a layer with large twist angle in between, though the observation may be obscured by the insufficient sensitivity of the current technique.

Post-acquisition reconstruction modes of 4D-STEM were also investigated and compared. Results showed that the annular bright field (ABF)-STEM, ptychographic phase, and divergence of differential phase contrast (DPC) can identify low and high atomic number atoms simultaneously with high resolution, surpassing the annular dark field (ADF)-STEM mode under the same imaging conditions. Series of reconstructed low angle ADF (LAADF)-STEM images from confined angular range showed potential in locating and identifying surface adsorbed atoms due to their different intensity profile as a function of reconstruction angular range, and combined with simulation, it will be possible to achieve atomic resolution elemental mapping after data acquisition.

Publications

Presented here is a list of published or under-review research accomplished during the course of this project. Four first authored works are the basis of the results chapter. Some co-author works are also listed but may not be included in the discussion of this thesis.

Chapter 4

(1) Fang S.,* **Wen Y.**,* Allen C.S., Ophus C., Han G.G.D., Kirkland A.I., Kaxiras E., & Warner J.H. Atomic electrostatic maps of 1D channels in 2D semiconductors using 4D scanning transmission electron microscopy. *Nat. Commun.* **10**, 1127 (2019). (*equal contribution)

(2) **Wen Y.**, Fang S., Lu Y., Allen C.S., Ophus C., Kaxiras E., Kirkland A.I., & Warner J.H. Mapping 1D Confined Electromagnetic Edge States in 2D Monolayer Semiconducting MoS2 Using 4D-STEM, *ACS Nano* **16**, 6657–6665 (2022)

Chapter 5

(3) **Wen Y.**, Coupin M.J., Hou L., Allen C.S., Kirkland A.I., Kaxiras E., & Warner J.H. Electric Field Oscillations in Graphene Moiré Superlattices Imaged by 4D STEM. (Close to submission)

Chapter 6

(4) **Wen Y.**, Ophus C., Allen C.S., Fang S., Chen J., Kaxiras E., Kirkland A.I., & Warner J.H. Simultaneous identification of low and high atomic number atoms in monolayer 2D materials using 4D scanning transmission electron microscopy. *Nano Lett.* **19**, 6482-6491 (2019).

Co-Author

(5) Ryu G-H., France-Lanord A., **Wen Y.**, Zhou S., Grossman J. C., & Warner J. H. Atomic Structure and Dynamics of Self-Limiting Sub-Nanometer Pores in Monolayer WS_2, *ACS Nano*, **12**, 11638–11647 (2018).

(6) Chen J., Zhou S., **Wen Y.**, Ryu G-H., Allen C. S., Lu Y, Kirkland A. I., & Warner J. H. In-situ High Temperature Atomic Level Dynamics of Large Inversion Domain Formations in Monolayer MoS_2, *Nanoscale* **11**, 1901-1913 (2019).

(7) Chen J., G. S. Jung, Ryu G-H., Chang R-J., Zhou S., **Wen Y.**, Buehler M. J., & Warner J. H. Atomically Sharp Dual Grain Boundaries in 2D WS_2 Bilayers, *Small*, **15**, 1902590 (2019).

(8) Ryu G-H., Chen J, **Wen Y.**, Zhou S., Chang R-J., & Warner J. H. Atomic Structural Catalogue of Defects and Vertical Stacking in 2H/3R Mixed Polytype Multilayer WS_2 Pyramids, *Nanoscale*, **11**, 10859-10871 (2019).

(9) Park H., **Wen Y.**, Li X.S., Choi W., Lee G-D., Strano M., & Warner J.H. Atomically Precise Control of Carbon Insertion into hBN Monolayer Point Vacancies using a Focused Electron Beam Guide, *Small*, **17**, 2100693 (2021)

Acknowledgement

I would like to express my sincere appreciation to my supervisor, Professor Jamie Warner, who had not only incubated many of my research ideas and provided me with sufficient resources to realize them, but also have been very supportive and encouraging. I would also like to thank the China Scholarship Council that granted a full scholarship to me which enables me to carry out my research without worries.

I would like to thank Dr Christopher Allen who trained me on JEOL JEM-ARM300 STEM and the Merlin Medipix pixelated detector during my STEM sessions at electron Physical Science Imaging Centre (ePSIC), Diamond light source in Harwell. He had also provided me with methods to carry out post-acquisition reconstructions and answered all my questions with patience. I would like to thank Dr Colin Ophus from Molecular Foundry user facility at Lawrence Berkeley National Laboratory who provided me with Matlab code to process the 4D-STEM data which allows me to thoroughly understand the calculation process and be able to carry out similar research on my own. I would like to thank Dr Shiang Fang (from Harvard University at the time of our collaboration) for performing the density functional theory calculation for our work in 4D-STEM with patience and meticulosity. I would also like to thank Professor Angus Kirkland who kindly revised my manuscripts and provided invaluable advice. I would also like to thank Dr Ian Griffiths from David Cockayne Centre for Electron Microscopy (DCCEM) who trained me on JEOL JEM-ARM200 STEM, Dr Matthew Spink from ePSIC who trained me on JEOL JIB4700F, and Mr Paul Pattinson from Department of Physics who trained me on Hitachi S-4300 field emission SEM.

During my time at Nanostructured Materials Group, my colleagues/friends have

always supported me and without their help I wouldn't complete my work. Dr Gyeonghee Ryu has been a great tutor and kind friend, and with my colleague Dr Jun Chen and Dr Sapna Sinha, we have spent long hours in the STEM control room and does not feel bored or lonely. My colleague Linlin Hou and Yang Lu provided me with sufficient and high quality 2D materials which I will always be grateful. My colleague and roommate, Qianyang Zhang, has always been so calm and affirmative that you couldn't ask for a better lab buddy and roommate.

Senior students in our group have taught me a lot when I started in the lab. Dr Si Zhou has trained me on JEOL JEM-ARM200 STEM and guided me to complete in-situ observation of two dimensional materials. Dr Wenshuo Xu, Dr Tongxin Chen, and Dr Martin Tweedie demonstrated CVD synthesis and transfer technique to me, which are essential for my doctoral project. Dr Yingqiu Zhou, Dr Sha Li, and Dr Renjie Chang provide me with patient help in the lab and have always been supportive and kind. Special thanks to Dr Hefu Huang who wrote an elegant Matlab code for me to convert the QSTEM simulation raw files, which I used in every simulation, and I will always be grateful for his help.

I would also like to thank my parents and childhood friends. My parents shaped me and made me who I am today, and I can never reciprocate the love I received. My lovely friends in different time zones are mostly 24/7 online when I need emotional help and advice, without them I would be much less merry.

Table of Contents

Chapter 1 Introduction 1

1.1 Project Aims 1

1.2 The Scope of this Thesis 1

Chapter 2 Literature Review 4

2.1 Introduction 4

2.2 Two Dimensional (2D) Transitional Metal Di-chalcogenides (TMDs) Materials 4

2.2.1 Properties and Application of 2D TMDs 5

2.2.2 Synthesis of TMDs 8

2.3 Characterization of TMDs using (S)TEM 11

2.3.1 Principle of (S)TEM 11

2.3.2 Resolution and Aberration in STEM 17

2.3.3 4D-STEM 19

2.3.4 Centre of Mass (CoM) and Electromagnetic Field 22

2.3.5 Phase retrieval 27

2.3.6 Virtual Detector 30

2.4 In-situ Defect Evolution in 2D TMDs 31

2.4.1 Electron beam damage and mechanisms 32

2.4.2 Point and Line Vacancy 35

2.4.3 Nanopore, Hole, and Hole Edge 38

2.4.4 Dopants and Nanocrystal 40

2.4.5 Contamination 42

2.5 Conclusion 44

Chapter 3 Methodology 53

3.1 Introduction 53

3.2 Chemical Vapour Deposition Synthesis 53

3.2.1 MoS_2 53
3.2.2 WS_2 55
3.2.3 Graphene 56
3.3 Transfer and Cleanliness of 2D materials 57
3.4 Optical Microscopy and Scanning Electron Microscopy 61
3.5 Scanning Transmission Electron Microscopy 62
3.5.1 Aberration-Corrected STEM 62
3.5.2 4D-STEM, Quantitative Conversion and Reconstruction 67
3.5.3 Image Analysis 73
3.5.4. ADF-STEM Image and CoM Simulation 76
3.5.5. Phase Reconstruction 76
3.5.6 Density Functional Theory (DFT) Calculations 76
Chapter 4 MoS_2 and WS_2 79
4.1 Introduction 79
4.2 MoS_2 and WS_2 Lattice and Simple Defects 79
4.3 Nanopore and Edges 89
4.4. Conclusions 98
Chapter 5 Graphene Moiré Superlattices 102
5.1 Introduction 102
5.2 Results and discussion 103
5.3 Conclusion 110
Chapter 6 Simultaneous Identification of Low and High Atomic Number Atoms 114
6.1 Introduction 114
6.2 Results and discussion 117
6.3 Conclusions 127
Chapter 7 Conclusion and Outlook 132
7.1 Conclusion 132
7.2 Outlook 134

Appendix A 136

Appendix B 138

Appendix C 145

Appendix D 147

List of Abbreviations

(S)TEM	(Scanning) transmission electron microscopy
1D	One-dimensional
2D	Two-dimensional
4D STEM	Four-dimensional scanning transmission electron microscopy
ABF	Annular bright field
ADF	Annular dark field
BF	Bright field
BFD	Bright field disk
CBED	Convergent beam electron diffraction
CoM	Centre of mass
DFT	Density functional theory
div(DPC)	Divergence of differential phase contrast
DPC	Differential phase contrast
ePIE	Extended phase iterative engines
FFT	Fast Fourier transform
HAADF	High angle annular dark field
hBN	Hexagonal boron nitride
HER	Hydrogen evolution reaction
IAM	Independent atom model
iCoM	Integrated centre of mass
iDPC	Integrated differential phase contrast
iDPC	Integrated differential phase contrast
IPA	Isopropyl alcohol
LV	Line sulphur vacancy
PMMA	Poly-methyl-methacrylate
POA	Phase-object approximation

SEM	Scanning electron microscopy
SNR	Signal to noise ratio
STM	Scanning tunnelling microscopy
TBG	Twisted bilayer graphene
TMDs	Transition metal dichalcogenides
TTG	Twisted trilayer graphene
V_S	Single sulphur vacancy
V_{S2}	Double sulphur vacancy
WDD	Wigner distribution deconvolution
WPOA	Weak phase-object approximation

Chapter 1 Introduction

1.1 Project Aims

This thesis is focusing on using four-dimensional scanning transmission electron microscopy (4D-STEM) to study prototype two-dimensional (2D) materials. The technique involves using a high speed, high dynamic range pixelated detector, in conjunction with an existing annular dark field (ADF) detector in aberration-corrected STEM to give a full picture of the electrostatic properties of the imaging materials. The highlight of my project is the in-situ analysis of prototype 2D materials including graphene and transition metal dichalcogenides (TMDs), e.g., molybdenum disulphide (MoS_2) and tungsten disulphide (WS_2) and the influence from the various crystal defect.

1.2 The Scope of this Thesis

The thesis covers the research over 4 years of UK Ph.D. degree at the Department of Materials, University of Oxford. The density functional theory (DFT) calculations were performed by Dr. Shiang Fang at the Department of Physics, Harvard University.

In the next chapter, I summarized the past research that contributes to the choice of my research project. The literature review starts with an overview of the family of 2D materials, their properties, applications, and mainstream synthesis methods. A common characterization method for 2D materials, (S)TEM, was explained. Actions to improve resolution and using 4D-STEM to harvest more information were explained in the following sections. In the last section, *in situ* defect evolution and

efficient imaging of electron beam-sensitive materials was discussed.

Chapter 3 listed the experimental methods I used in my doctoral project. All 2D materials used in this project were synthesized via atmospheric pressure chemical vapour deposition (CVD). Preparation and initial examination of the materials were demonstrated. The full procedure for aberration-corrected STEM imaging, *in situ* imaging, 4D-STEM imaging, post-acquisition calculation, and reconstruction were thoroughly explained.

In chapter 4, I performed 4D-STEM on pristine monolayer MoS_2 and WS_2 crystal. I calculated the electric field and charge density in these TMDs with atomic resolution. I also studied the change in these electronic properties arising from crystal defects including point and line sulphur vacancies. The abnormal edge effect in one-dimensional (1D) TMDs edges was also discussed in this chapter. Ultra-long 1D MoS nanowire was also studied and the edge enhancement in the nanowire was found to be different from the lattice edge, supported by 4D-STEM simulation.

The fifth chapter involves turbostratic graphene, where two or more layers of graphene with random twist angles form periodic Moiré patterns and induce altered electronic properties. I studied a bilayer with a large twist angle and trilayer graphene with large and small twist angles and used 4D-STEM and independent atom model (IAM) simulation to analyse the different behaviour due to the different twist angles.

The sixth chapter is focusing on the possible imaging modes that can be reconstructed from a single set of 4D-STEM data. I reconstructed and compared the ptychographic phase, the divergence of differential phase contrast (div(DPC)), centre of mass (CoM), bright field (BF-), annular bright field (ABF-), low angle ADF (LAADF-), and simultaneous high angle ADF (HAADF-) STEM modes. I also

showed the possibility of identifying the species of dopant and adsorbed atoms using LAADF-STEM images reconstructed from varying angular ranges.

The final chapter concludes this doctoral project. Limitations of 4D-STEM and possible future work were also discussed.

Chapter 2 Literature Review

2.1 Introduction

Graphene, hexagonal boron nitride (hBN), and TMDs, layered oxides and perovskite have received a lot of attention due to their ability to exist as a 2D structure, where dimensionality changes dramatically how a material will behave, as seen in zero-dimensional (0D) quantum dot and 1D nanowire. The number of publications concerning graphene and graphene analogues is increasing exponentially since the re-discovery of graphene, but the electronic and optoelectronic application of such materials is always focusing on the perfect lattice, while the interesting behaviours rising from atomic defects are not fully utilized and require further understanding beyond conventional imaging technique.

In the first section, the properties of graphene and prototype TMDs MoS_2 and WS_2 as well as the synthesis methods were briefly discussed. In the next section, atomic resolution imaging of 2D materials using (scanning) transmission electron microscopy ((S)TEM) was examined. The focus of this section is to combine the common Z-contrast HAADF-STEM imaging with 4D-STEM imaging. The latter is based on acquiring the full CBED pattern at each probe position, comprising a '4D data set', which provides more information beyond traditional ADF-STEM imaging. The final section is focusing on imaging of beam-sensitive materials and how the intrinsic and beam-induced defects will evolve under continuous irradiation.

2.2 Two Dimensional Transition Metal Dichalcogenides Materials

2.2.1 Properties and Application of 2D TMDs

2D materials are a family of materials that can exist in one or few-atomic-layer forms. For example, layered materials contain layers that are weakly attracted to adjacent layers via van der Waals force, thus individual layer can be isolated from the bulk. These materials are considered 2D as the thickness is negligible compared to the dominant surface.[1]

The idea of 2D materials is intriguing as anomalous behaviours occur when it becomes 2D. Take graphite for example, when a lateral force is exerted on such materials, the atomic plane can slide against each other, thus historically graphite has been used as dry lubricant. It was long thought that its monolayer polymorph, graphene, is a theoretical idea and would not be stable upon isolation. However, in 2004, Andre Geim and Konstantin Novoselov first reported isolating graphene using duct tape to strip layers from graphite. By repeating this process, finally, they obtained monolayer graphene, which was found to have several superior properties: high charge carrier mobility and long mean free path, heat and electrical transport ability, and room temperature quantum hall effect.[2] These properties make graphene a strong candidate for future ultrathin transparent electronic devices, but the gapless feature of graphene hinders its wide application in optoelectronics and photocatalysis, where a semiconductor with band-gap engineering possibility is essential.[1]

The rise of graphene-analogues, 2D TMDs fills in the gap. TMDs are a family of van der Waals layered materials composed of elements from transition metal M (Mo, W, Ti, Zr, Hf, Ta, etc) and chalcogenides X (S, Se, Te) in the stoichiometry of MX_2, each metal atom is bonded to six chalcogenide atoms, and a chalcogenide atom is bonded to three metal atoms. Each monolayer contains three atomic planes in the

order of X-M-X (fig. 2.1b). They are analogues to graphene as they are both van der Waals 2D materials, thus MoS_2 has also been used as a dry lubricant like graphite.[3] The numerous combinations of M and X, stacking orders, and coordination offer sumptuous choices in terms of electronic properties from semiconducting (MoS_2, WS_2[4]), metallic (NbX_2, ReS_2,[5] TaX_2[6]), to magnetic (VX_2[7,8]) (fig. 2.1a), combined with semi-metal graphene and insulating multi-layer hBN,[9] open up a whole new era in 2D electronic and optoelectronic devices. The golden age of graphene has promoted the development on techniques in the field of synthesis, transfer, characterization, and device-fabrication which accelerate the study and application of 2D TMDs. Among them, MoS_2 and WS_2 are the prototype TMDs that have received attention following the rush of graphene. MoS_2 and WS_2 exhibit similar properties: they both have an indirect band gap (~1.29 eV) when in bulk form, and a direct band gap (~1.9 eV) as monolayer (fig. 2.1c).[5]

For monolayer MoS_2 and WS_2, there are two polymorphs 1T and 1H. The digit denotes the number of layers in a unit cell, the letter denotes the crystal structure, the 'T' indicates trigonal symmetry, and 'H' hexagonal. For bilayer and multilayer MoS_2 and WS_2, there are two common polytypes, 2H and 3R, where the digits follow the same fashion, 'H' denotes hexagonal, and 'R' denotes rhombohedral. 2H is two superimposed 1H monolayers and one layer having a 60° rotation, thus from the (001) direction, the S column in one layer coincides with the Mo column in the other layer, and vice versa. 3R structure is a stack of three 1H monolayers, where layers 1 and 2, 2 and 3, 3 and 1 have a respective displacement of an M-X distance. 1T is the octahedral coordination, and 1H, 2H, and 3R are trigonal prismatic coordination (fig. 2.1b). 1T phase is metastable and 1H phase is the energetically favoured monolayer structure. 2H and 3R are the stable phases naturally exist.[10] These phases can be switched to one another via phase transition initiated by strain and defect: 2H-3R

transition needs a gliding between monolayers, 2H-1T requires an S plane gliding,[11] and annealing metallic 1T phase can change it to semiconducting 2H phase[14].

Because of the direct band gap behaviour shown in monolayer TMDs, they have been used as a substitution for graphene in electronics. In 2010, Kis et al. fabricated a transistor with MoS_2 that achieve mobility of 200 $cm^2\ V^{-1}\ s^{-1}$, comparable to graphene nanoribbon.[12] The direct band gap also results in photoluminescence,[13] combined with their excellent transparency and flexibility, they can also be used in optoelectronics e.g. displays and wearable devices.[14] They are also a promising candidate for electrodes in solar cells and batteries. Recent attempts also include manipulating TMDs via e^-/h^+ doping to alter the electronic valley degree of freedom to store binary information.[15] Graphene and 2D TMDs also have a high surface area with no surface dangling bonds, making them suitable for membrane and molecular sieves for water filtering. MoS_2 edge is be catalytic for hydrogen evolution reaction (HER),[16] making them suitable for catalyst support in energy storage and membrane application.

To further utilize the broad family of 2D TMDs and various properties, van der Waals heterostructure can be made by stacking different TMDs materials. By selecting the candidate with suitable conduction band maximum and valence band minimum to achieve electron/hole separation in 2D devices. However, polymer contamination may be brought in during transfer steps, also the different crystallographic orientation of different layers requires precision in alignment, which urges researchers to find a more controllable transfer method.

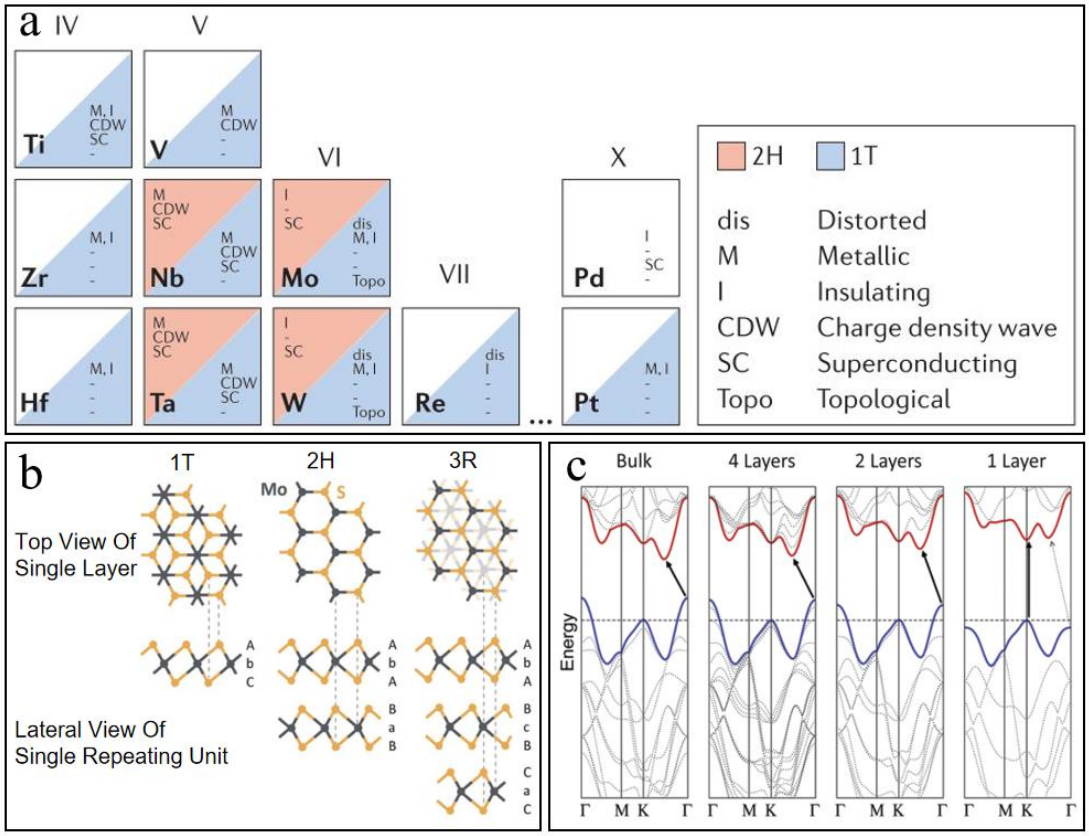


Figure 2.1. (a) Known layered TMDs arranged based on their transition metal element, labeled with their structural (2H, 1T or other) and electronic phases.[17] (b) Polymorph of MoS_2 in top view and side view,[11] (c) Calculated band structure of MoS_2, showing the change of transition in conduction band minimum and valence band maximum as a function of the number of layers.[13] Figures adapted with permission from: (a) ref 17. © 2017 Macmillan Publishers Limited, (b) ref 11, Creative Commons Attribution 3.0 Unported Licence, (c) ref 13. © 2010 American Chemical Society.

2.2.2 Synthesis of TMDs

The synthesis of 2D materials is always aiming for finding a scalable, reliable, and controllable process. For TMDs, from top down (fig. 2.2a), one can use mechanical and liquid exfoliation or chemical etchant that separate a few layers of TMDs by

cleaving a bulk crystal. This method is widely used to produce large-scale material, but the number of layers cannot be controlled. [1,18]

Another more prevalent method to produce high-quality 2D TMDs is from bottom up, to chemically synthesize them through vapour phase reaction, thermolysis, and layer-by-layer conversion. The vapour phase synthesis methods are summarised in fig. 2.2b. The sulphurization method vaporizes the chalcogenide source upstream which reacts with solid phase precursor downstream (fig. 2.2b top). Direct phase transport vaporizes TMDs powder for vapour phase deposition, and by using a mixture of TMDs as precursors, it can produce an intrinsic heterostructure (fig. 2.2b bottom).[19] Take MoS_2 as an example, the layer-by-layer surface sulphurization method uses MoO_2 microcrystal template that undergoes controlled surface sulphurization, the highly crystalline surface MoS_2 can then be detached by poly-methyl-methacrylate (PMMA) transfer (fig. 2.2c).[20] Thermolysis methods use ammonium thiomolybdate ($(NH_4)_2MoS_4$) as the sole precursor and thermally decompose the salt to obtain MoS_2 (fig. 2.2d).[21] Among all, chemical vapour deposition (CVD) is regarded as the most suitable approach for large scale synthesis. In the CVD approach, both the metal source and the chalcogenides source are vaporized, and the reactant are deposited on the substrate downstream (fig. 2.2b middle). The vapour-phase synthesis widens up the substrate choice, e.g. glassy carbon, quartz, Si/SiO_2, and notably graphene and c-plane sapphire, for they have the same hexagonal lattice symmetry for van de Waals epitaxial growth.[22] The sumptuous selection of substrate allows the device production time to be reduced because the transfer step can be eliminated.

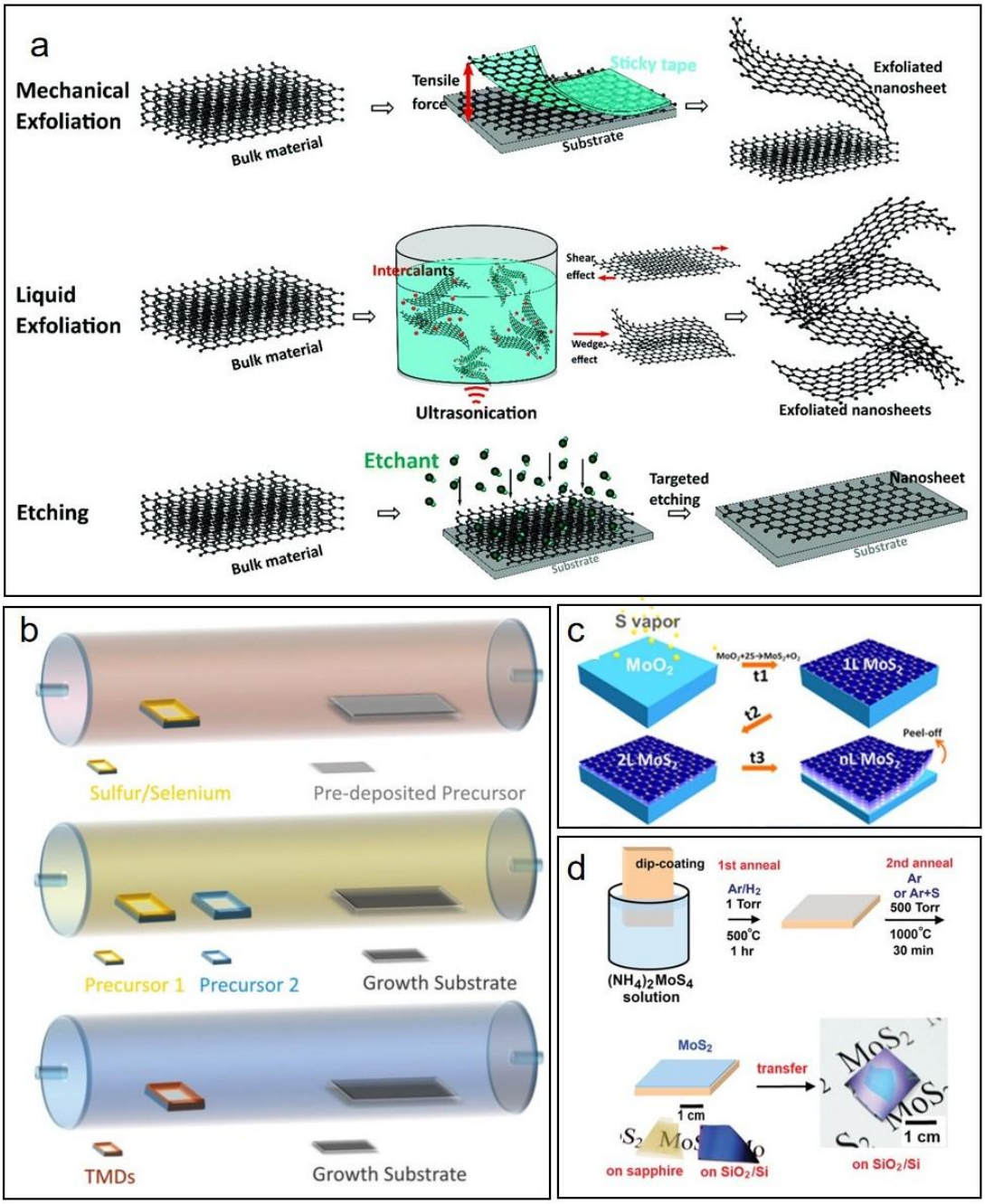


Figure 2.2. Synthesis methods for 2D materials. (a) Top-down methods, from top to bottom are mechanical exfoliation, liquid exfoliation, and chemical etching.[23] (b) Schematic vapour phase synthesis method, from top to bottom are sulphurization, chemical reaction, direct transport, respectively.[19] (c) Layer-by layer surface sulphurization.[20] (d) Thermolysis and subsequent peeling-off.[21] Figures adapted with permission from: (a) ref 23, © Creative Commons Attribution 3.0 Unported Licence, (b) ref 19, © 2015 The Royal Society of

Chemistry (c) ref 20, © 2013 American Chemical Society (d) ref 21, © 2012 American Chemical Society.

2.3 Characterization of TMDs using (S)TEM

Electron microscopy (EM) is a powerful tool that provides information on crystal/atomic structure and electronic information of the specimen. This is enabled by the diverse signals generated from the interaction between the incident electron beam/probe with the specimen, aided by various signal detectors.[24] The other benefit of using (S)TEM is its ability to reach atomic resolution (~ 0.1 nm). The (S)TEM sample must be electron-transparent (~100 nm thick) to prevent multiple scattering events, which can be a great task for metal and perovskite samples that require extensive machining, but 2D materials are inherently suitable for (S)TEM imaging. However, they are also prone to electron beam irradiation damage. To achieve does-efficient imaging, the operation of the EM and *in situ* defect evolution and prevention must be fully understood. In this section, principles and precautions of imaging 2D TMDs using (S)TEM will be explained, along with a new STEM technique, 4D-STEM.

2.3.1 Principle of (S)TEM

The principle of an EM is parallel to a visible light microscope; thus, the former is often demonstrated with a ray diagram and ellipsoidal lenses (fig. 2.3a, b). Instead of photons, EM uses accelerated electrons as an imaging probe. After emission, the electrons pass through several fixed-position electromagnetic lenses. The strength of these condenser lenses and upper objective lens can be adjusted by adjusting the

current (thus magnetic field) which affects the trajectories of electrons passing through.[25]

The image contrast in an (S)TEM image is formed by the interaction between the incident electrons and the specimen. Electrons can be regarded as a particle and as a wave. As a particle, it has a mass and a momentum. It passes through the specimen and is scattered by the atom nuclei or atomic electron cloud. As a wave, it propagates and is diffracted by the specimen, its wavefunction at a coordinate $\boldsymbol{r}$ in real space, $\Psi(\boldsymbol{r})$, is modulated by the object transmission function $f(\boldsymbol{r})$ with amplitude a and/or phase φ, rendering an object exit wavefunction, $obj(\boldsymbol{r})$

$$obj(\boldsymbol{r}) = \underbrace{a(\boldsymbol{r}) \exp\left(i\varphi(\boldsymbol{r})\right)}_{object\ transmission\ function} \cdot \Psi(\boldsymbol{r}) (eq.\ 2.1)$$

The phase preserves structural information of the specimen, but it cannot be recorded by detector. Historically, several attempts have been made to retrieve the phase of the object transmission function. Phase-contrast high-resolution TEM (HRTEM) is based on phase-object approximation (POA), which assumes the specimen is thin enough that only the phase is modulated after propagation through the specimen. Simplify the amplitude to $a(\boldsymbol{r}) = 1$, the change in phase, $d\varphi$, is related to the projected potential $V_{\perp}$ via the change in wavelength,

$$d\varphi = \sigma V_{\perp}(\boldsymbol{r})\ (eq.\ 2.2)$$

where $\sigma = \frac{\pi}{\lambda E}$ is the interaction constant defined by wavelength and accelerating voltage, thus the object transmission function can be re-written as

$$f(\boldsymbol{r}) = \exp\left(i\sigma V_{\perp}(\boldsymbol{r})\right)\ (eq.\ 2.3)$$

assuming the absorption is negligible. If the specimen is thin enough that $V_{\perp}(\boldsymbol{r}) \ll 1$, then it gives the weak phase-object approximation (WPOA) that the phase is linearly proportional to the projected potential

$$f(\boldsymbol{r}) = 1 - i\sigma V_{\perp}(\boldsymbol{r}) \ (eq.\ 2.4)$$

However, there is a $90°$ phase shift between the scattered and unscattered beam,[24] thus the scattered beam will not contribute to the object exit wavefunction, i.e., no contrast. The lens aberrations add additional phase shift to the scattered beam; thus, it is no longer out of phase with the unscattered beam, and the phase shift can be recorded as an intensity variation of the object exit wave. Following WPOA, the contrast transferred to the detector is dependent on the aberrations, which can be expressed in phase-contrast transfer function (PCTF).

$$PCTF = sin(\chi(u)) \ (eq.\ 2.5)$$

where $\chi(\mathrm{u})$ is the phase-distortion function, and u is the reciprocal-lattice vector (spatial frequency). $\chi(\mathrm{u})$ is defined by defocus (Δf), wavelength of incident electrons (λ), and the spherical aberration coefficient (Cs)

$$\chi(u) = \pi\Delta f\lambda u^2 + \frac{1}{2}\pi C_s\lambda^3 u^4 \ (eq.\ 2.6)$$

PCTF is an indication of the contrast and resolution at given Δf and Cs: a negative PCTF indicates a negative contrast (dark atoms), and vice versa.[26] The sinusoidal nature of PCTF gives a low contrast at low u, which was tackled by using a phase plate that adds a $\pi/2$ phase shift which increased the contrast for imaging long-range features in amorphous materials.[27]

The first crossover of the PCTF with the spatial frequency axis was denoted as the point resolution. To increase the point resolution, Scherzer proposed that the PCTF can be optimized by the balance between Δf and Cs, where a near-ideal PCTF can be obtained if $d\chi/du$ is near 0 for an extended range of u

$$\frac{d\chi}{du} = 2\pi\Delta f\lambda u + 2\pi C_s\lambda^3 u^3 \ (eq.\ 2.7)$$

$\frac{d\chi}{du}$ approaching 0 gives 'Scherzer defocus' for an ideal PCTF

$$\Delta f_{Sch} = -\left(\frac{4}{3}C_s\lambda\right)^{1/2} \ (eq.\ 2.8)$$

Combining eq.2.6 and 2.8, one can obtain the resolution at Scherzer defocus (reciprocal of corresponding u_{Sch})

$$r_{Sch} = 0.66{C_s}^{1/4}\lambda^{3/4} \ (eq.\ 2.9)$$

Besides Cs and λ, the resolution will also be limited by the spatial and temporal coherence of the electron source. These effects can be included in the PCTF in the form of multiplication of envelope functions, which gives the effective PCTF.

$$PCTF_{eff} = \sin(\chi(u))E_aE_c \ (eq.\ 2.10)$$

where E_a is the spatial coherence envelope, and E_c is the chromatic aberration (temporal) envelope. The envelope functions are equivalent of a virtual aperture at the at the back focal plane of the objective lens, thus at high spatial frequency, the PCTF is reduced, imposing a new resolution limit known as 'information limit'. Based on equations 2.9 and 2.10, there are several factors that can be mitigated to improve the resolution: wavelength of incident electrons, spherical aberration, spatial and temporal coherence, which will be discussed in section 2.3.2. To sum up, PCTF before the Scherzer resolution can be easily interpreted, and if the information limit is at spatial frequency beyond that of Scherzer focus, interpretation of such information is not straightforward and will require image simulation.

STEM is another powerful imaging tool that is essential to materialists. The benefit of STEM is that it offers various information facilitated by multiple post-specimen detectors. The contrast formation in ADF-STEM is more straightforward. STEM uses a convergent electron beam (probe) focused on the specimen that forms a disk diffraction pattern called a convergent beam electron diffraction (CBED) pattern at the far field with a convergence semi-angle α, defined by the condenser lens

aperture and the probe-forming optics of the microscope. The probe is deflected by scan coils to scan across the region of interest. The central part of the CBED pattern is also referred to as the bright field disk (BFD) because of the high intensity of the direct beam and the spherical shape of the aperture.

Signals outside and inside the direct scattering cone have both been used to construct STEM images. A widely used imaging mode in STEM is to integrate the intensity of scattered electrons which form mass-thickness contrast and atomic resolution Z-contrast, as thicker specimens and heavier atoms scatter more electrons.[24] If a concentric ADF detector is used to capture electrons scattered by the atom nucleus to a large scattering angle (Rutherford scattering) and exclude the coherent BF signals, a HAADF-STEM image will be obtained, which intensity is strongly dependent on the atomic number of the atoms ($I \sim Z^{1.7}$-Z^2) which provide intuitive elemental information.[28] However, HAADF-STEM imaging mode only collects a small proportion of the transmitted electrons. To collect more signals, the collection angle can be adjusted by changing the camera length to form medium angle- and low angle-ADF images, which are less Z-dependent and improve contrast for low atomic number atoms,[30] but the intensity is less interpretable as the intensity is from a mixture of coherent and incoherent imaging.

By using an axial BF detector of outer collection angle from $0 - \sim 0.5\,\alpha$ to collect the elastically scattered electrons inside BFD, a coherent phase-contrast BF-STEM image similar to conventional TEM can be recorded. However, it is difficult to interpret the contrast in BF-STEM images of thick specimens and requires prior knowledge of crystal structure and simulation. An improved BF imaging mode used an annular detector of inner and outer angles β_1 and β_2, where $0.5\alpha < \beta_1 < \beta_2 \leq \alpha$, to record an ABF image. Previous study have also used a BF detector and a

beam-stop to achieve similar results.[29] The ABF-STEM image contrast is from the coherent phase contrast and the incoherent channelling effect of atomic columns focuses the probe. ABF-STEM imaging was found to be efficient in resolving low-atomic-number elements.[30] Both ABF-STEM and HAADF-STEM modes were found to be insensitive to specimen thickness at suitable defocus value, but ABF-STEM imaging is not Z-contrast due to mixed contrast mechanism, its interpretation may need parallel recording of HAADF-STEM images.[29,31,32] Note that similar to TEM imaging, the atoms under ADF-STEM imaging mode have a positive contrast (bright atoms), while BF- and ABF-STEM mode render negative contrast (dark atoms), as shown in chapter 6.

Though not employed in this thesis, it should be noted that one important feature of STEM is that it collects signals from the beam/specimen interaction that provide information beyond conventional imaging. The inelastic scattering of electrons through the specimen generates signature signals of elemental species and electronic structures. For example, an electron energy loss spectroscopy (EELS) detector placed underneath the imaging detector probes the electronic state of the specimen by measuring the energy spectrum of the transmitted electrons.[33] Energy-dispersive X-ray spectroscopy (EDX) placed above the specimen collects the characteristic X-ray induced by the incident electrons which is used to for elemental mapping.[34]

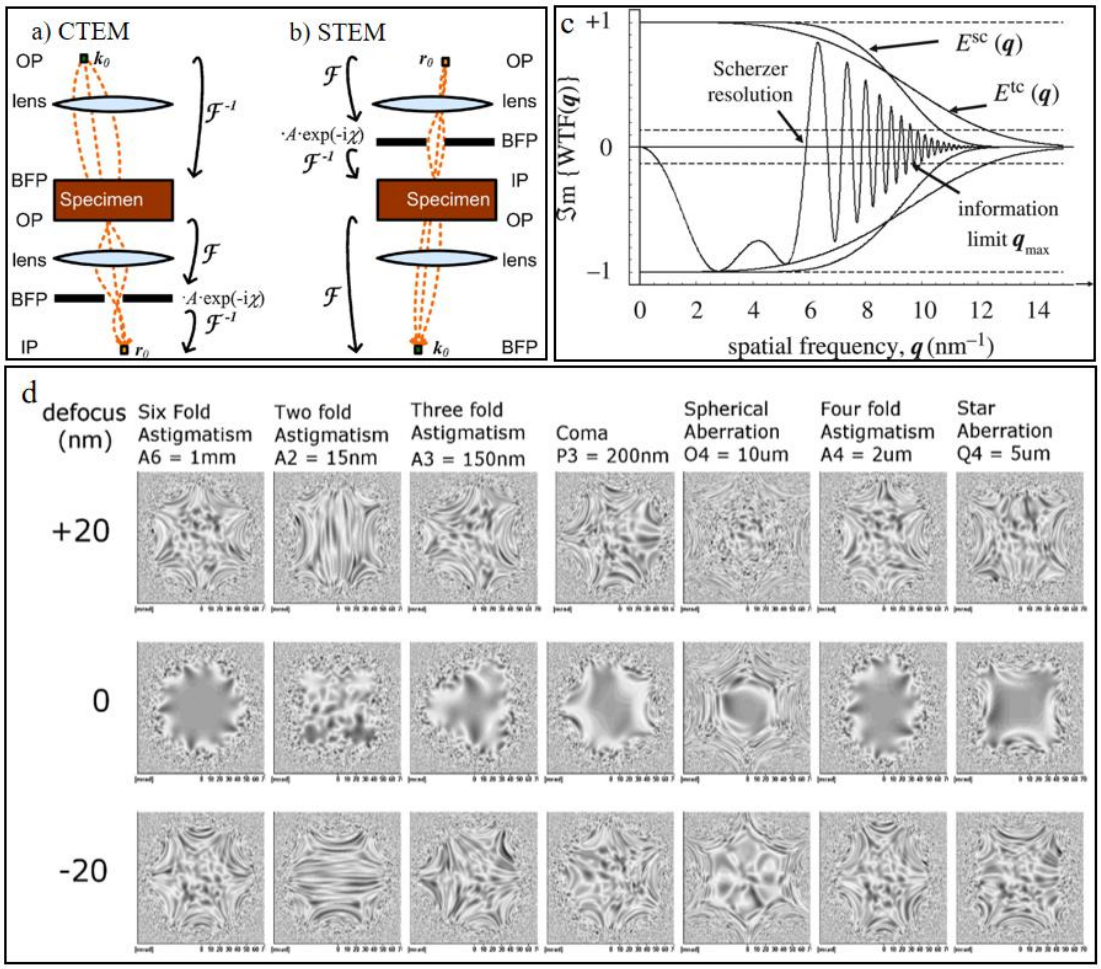


Figure 2.3. Schematic diagram of the reciprocity relation between (a) conventional transmission electron microscopy (CTEM) and (b) scanning transmission electron microscopy (STEM).[35] OP is the abbreviation of object plane, BFP back focal plane, IP image plane. (c) Phase-contrast transfer function damped by envelope functions E^{sc} and E^{tc} of the spatial and temporal coherence.[36] (d) Types of astigmatism and aberration on either side of the focal point simulated by COSMO software, showing their effects on distorting the ronchigram.[37] Figures adapted with permission from: (a-b) ref 35, © 2016 Elsevier Ltd (c) from ref 36, © 2009 Royal Society (d) ref 37, acquired from Dr. Christopher Allen, electron Physical Science Imaging Centre (ePSIC).

2.3.2 Resolution and Aberration in STEM

In a STEM experiment, to successfully distinguish signals from adjacent atoms, the probe size must be smaller than the separation between them. In graphene, the C-C distance is 0.142 nm, in MoS_2 z-projection Mo-S distance is 0.18 nm, which can be achieved by aberration-corrected (S)TEM. The resolution of STEM is determined by the size of the incident probe, which is dependent on the performance of the probe-forming electromagnetic lenses and the coherence of the electrons. The coherence of the electrons can be quantified by spatial and temporal coherence. Spatial coherence describes the intensity distribution of the source, related to the effective source size and the finite detector size. Varying external electromagnetic fields also decrease the effective spatial coherence of the beam. Temporal coherence is from the energy spread of the source, and the chromatic aberration of the lenses.

In STEM, a condenser lens is used to demagnify the electron source to reduce the effect of partial source spatial coherence, thus to achieve a small probe with reasonable current, the brightness of the gun, which is defined as the current per unit area per unit solid angle subtended by the beam, has to be high.[38] This requires a stable electron source e.g., a cold field emission gun (FEG) and Schottky FEG, which generate electron probes with small energy spread and high brightness.

Besides the electron source, lens aberration is the major limitation of (S)TEM resolution.[25] Lens aberration means the probe is not in focus as the probe-forming lenses are not perfect. Apertures were used to exclude high-angle beams where the aberration is most severe, and high-end (S)TEM always have aberration correctors. The common types of aberrations are:

1) Astigmatism: because the magnetic lens is not perfect, the magnetic field it creates is not uniform and will bend the beam. These variations in field

strength can be easily corrected using a stigmator that provides compensating field.

2) Spherical aberration (Cs): increase refraction at the edge of lens compared to those around the optical axis, which means a point source will be blurred to be a disk, thus limiting the resolution. This is compensated by additional multipole electromagnetic lenses which break the axial symmetry and slightly diverges the beam. Usually a pair of double-hexapole lenses was used to induce a negative Cs which compensate the inherent positive Cs.
3) Chromatic aberration (Cc) of objective lens: the objective lens has different refractive index for electrons with different wavelength (energy), so if the accelerated electrons have different wavelength (energy spread), they will not be focused onto the same point on the focal plane, causing a blurred image. Monochromator is used for EELS and energy filtering to limit the energy spread of the incident electrons. Cc corrector is an additional optical component which actively corrects for the change in focal distance over the range of energies.

Geometric aberrations in the STEM beam can be imaged in the Ronchigram (shadow image at infinite magnification) of an amorphous sample (fig. 2.3d). The operator can manually correct astigmatism and some low-order aberrations as they can be easily spotted as asymmetry at defocus and overfocus in the Ronchigram, but the high-order aberration requires aberration correction software. However, due to the instability of the corrector and the microscope, the corrected aberrations will resurface during imaging which must be considered during (S)TEM image simulation.

2.3.3 4D-STEM

4D-STEM refers to a technique of using an additional pixelated detector to record the CBED pattern at each probe position during the regular scan. The STEM raster scan can be considered as a 2D matrix of probe position $\boldsymbol{r}$ at specimen plane in real space, and the CBED pattern image as a 2D matrix at diffraction plane, rendering a 4D data set (fig. 2.4). This should not be confused with '4D Electron Microscopy (4D EM)' proposed by Zewail et al.,[39] in which the fourth dimension represents time series.

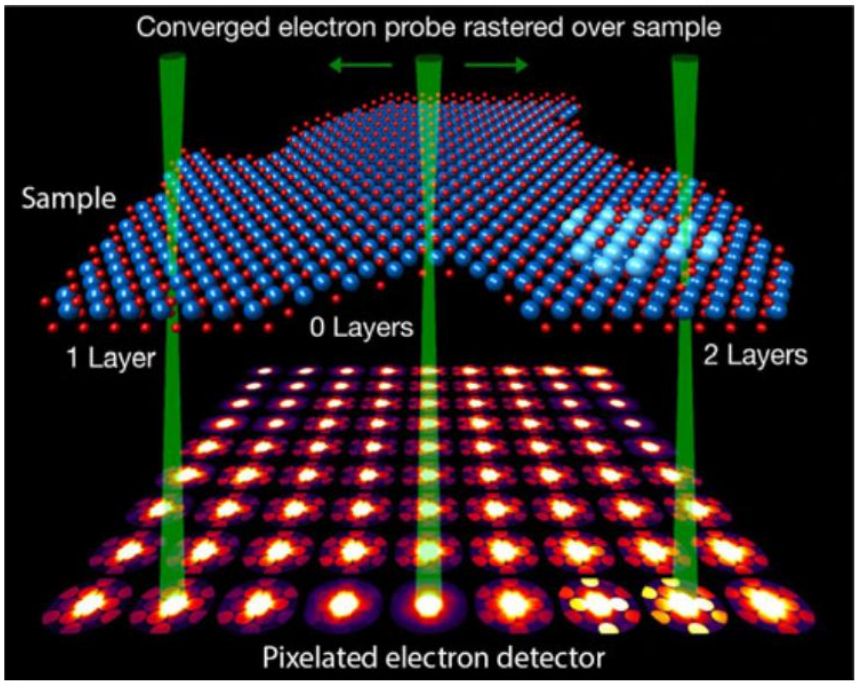


Figure 2.4. Schematic diagram of a STEM probe scans across a sample with 1, 0 (vacuum), and 2 layers of thickness and the variation in the corresponding CBED patterns. The CBED patterns are position averaged for better representation.[40] Figures adapted with permission from © Microscopy Society of America 2019, under the terms of the Creative Commons Attribution licence.

The reason for recording the CBED pattern is that it has a wealth of information that would have been discarded in conventional ADF-STEM imaging. CBED has been used extensively in CTEM for its sensitivity in the determination of crystal symmetry.[41] Position averaged CBED (PACBED) was used to determine the specimen thickness of a known crystal by comparing it with simulated PACBED patterns. However, the charge coupled device (CCD) and scintillator used for (S)TEM imaging is not ideal for recording CBED patterns. For example, a low resolution 256 x 256-pixel ADF-STEM image corresponds to in total of 65536 pixels i.e. probe position, and to record a CBED pattern at each probe position requires a detector with high readout speed and frame rate to achieve a reasonable acquisition time, as well as an extensive dynamic range for the accurate measurement of a single electron scattering and high-intensity BFD at the same time.[42] It is until recently, advances in pixelated direct electron detector enabled the efficient recording of CBED patterns.[43] Two types of pixelated detectors have been developed for 4D-STEM: monolithic active pixel sensors (APS) and hybrid pixel array detector (PAD). APS detector is composed of a complementary metal–oxide–semiconductor (CMOS) chips with a sensitive doped epitaxial layer. It is suitable for recording single electron events for its high sensitivity, but relatively poor dynamic range.[44,45] PAD is composed of an array of photodiodes bump-bonded to an application-specific integrated circuit, it uses a high-gain integration and counting circuitry in each pixel, giving single electron sensitivity, high dynamic range, and fast readout speeds,[46] which was chosen for this project. The retractable pixelated detector usually sits underneath the ADF detector, if all other detectors are retracted, by optimizing the camera length, a CBED pattern with scattered electrons to desired angular ranges can be recorded (e.g. shorter camera length, larger angular range).[47] If the ADF detector is inserted, a simultaneous ADF-STEM image will be obtained, and the Z-contrast image can be used as a reference for later reconstruction.[48,49] In practice, a large camera length magnifies the central BFD, which is more convenient and accurate for

measuring the shift of CoM of the BFD. On the other hand, using a small camera length, the direct beam can collect most of the electrons that interact with the specimen, which enables the post-experimental reconstruction various imaging modes. By using a virtual detector, which sums the number of electrons in a given angular range, one can reconstruct BF-, ABF-, ADF-, and HAADF-STEM images with arbitrary angular cut-off. It also enables more complex reconstructions e.g., phase reconstruction from differential phase contrast (DPC) and ptychography.

In the following sections, applications of 4D-STEM in electric field mapping, ptychographic phase retrieval, and post-acquisition image reconstruction will be discussed.

2.3.4 Centre of Mass and Electromagnetic Field

In 1977, Waddell et al.[50] proposed that the momentum transferred to the electron probe due to interaction with the specimen (e.g. local electromagnetic field and thickness variation, as shown in fig. 2.4 & 2.5) is linearly related to the gradient of phase of the object transmission function and can be measured by an anti-symmetrical first moment detector system yielding the CoM of the BFD intensity distribution. Waddell et al.[51] later evaluated the linearity using the first moment detector as well as a split detector system introduced by Dekkers and de Lang,[52] otherwise known as the differential phase contrast (DPC) imaging. Conventional DPC imaging uses an annular two- or four-segmented detector design where the angular deflection of the beam can be easily calculated by the difference between the diametrically opposed detector segments.[52,53] Previously, low magnification STEM coupled with DPC has been used extensively to map sub-micron-range magnetic domains by Chapman et al.,[54–56] which is a mode of

Lorentz microscopy, and with development in aberration corrected STEM, Shibata et al. achieved mapping of both the mesoscopic polarization fields and the atomic electric field with $BaTiO_3$,[57] and later with single Au atoms.[58]

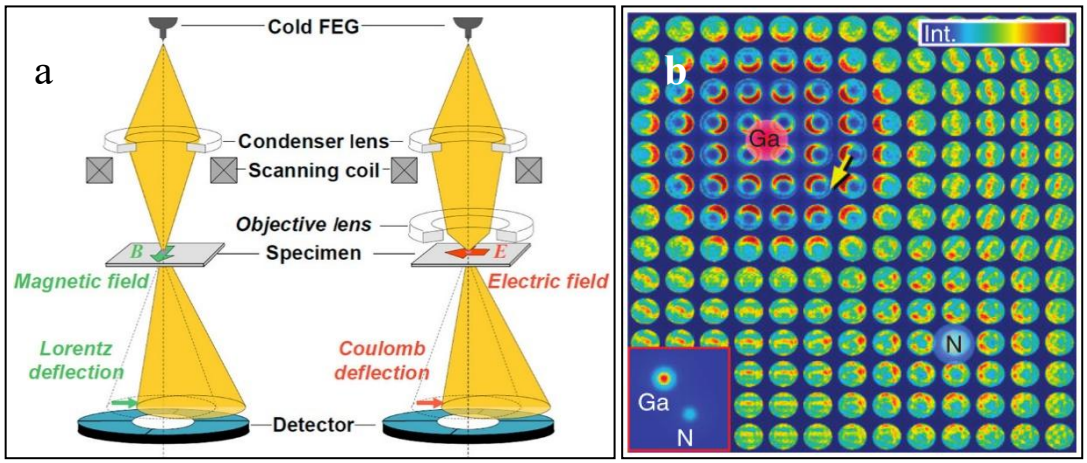


Figure 2.5. (a) Schematic diagram of beam shift under the magnetic and electric field collected by a segmented detector.[59] (b) Beam intensity and distribution variation in GaN, where the CoM shifts most with the vicinity of the atoms, and the variation is more intense for heavier Ga atoms.[60] Figures adapted with permission from (a) ref 59, © 2017 American Chemical Society (b) ref 60, © Creative Commons Attribution 4.0 International License

In 2014, Müller et al. proved the expectation value of lateral momentum transfer is related to the projected electric field by Ehrenfest's theorem,[60] which gives the quantitative calculation of atomic electric field,[61] and the atomic electric field measured in $SrTiO_3$ has shown accordance with their multislice simulation (fig. 2.6) and DFT calculation. The idea is, an electron with an elementary charge e will experience a total electromagnetic Lorentz force $\boldsymbol{F}$, where

$$\boldsymbol{F} = -e(\boldsymbol{E} + v \times \boldsymbol{B}) (eq.\ 2.12)$$

Assuming there is no magnetic field, then the particle will only experience the Coulomb force $-e\boldsymbol{E}$. The derivation of momentum over time gives

$$\frac{d\boldsymbol{p}}{dt} = \boldsymbol{F} = -e\boldsymbol{E} (eq.\ 2.13)$$

According to Ehrenfest's theorem, which relates the time derivative dt of the expectation values of the momentum $d\langle \boldsymbol{p}_\perp \rangle$ to the expectation value of the force, which is proportional to the expectation value of the electric field $\langle \boldsymbol{E}_{\perp \mathbf{pc}} \rangle$, thus eq.2.13 is still valid in the quantum mechanical context.

$$\frac{d\langle \boldsymbol{p}_\perp \rangle}{dt} = -e\langle \boldsymbol{E}_{\perp \mathbf{pc}} \rangle (eq.\ 2.14)$$

where $\boldsymbol{p}_\perp$ is the lateral momentum, $\boldsymbol{E}_{\perp \mathbf{pc}}$ is the probe-convolved projected electric field, the convolution between the true projected electric field $\boldsymbol{E}_\perp$ and the intensity distribution of the imaging probe $\boldsymbol{I}_\mathrm{p}$.

$$\boldsymbol{E}_{\perp \mathbf{pc}} = \boldsymbol{E}_\perp * \boldsymbol{I}_\mathrm{p}\ (eq.\ 2.15)$$

Moving dt to the right side, and assume the electron travels through the specimen in constant speed $dt = dz/v$, where v is electron velocity at given accelerating voltage, and z is specimen thickness, then

$$d\langle \boldsymbol{p}_\perp \rangle = -e\langle \boldsymbol{E}_{\perp \mathbf{pc}} \rangle dt = -e\langle \boldsymbol{E}_{\perp \mathbf{pc}} \rangle dz/v (eq.\ 2.16)$$

The momentum transfer is related to the CoM shift via

$$\Delta \boldsymbol{p} = \langle \boldsymbol{p}_\perp \rangle = \boldsymbol{p} \cdot sin(\boldsymbol{CoM_r})\ (eq.\ 2.17)$$

where $\boldsymbol{CoM_r}$ is the radial CoM shift in radian. $\boldsymbol{p} = h/\lambda$ gives

$$\langle \boldsymbol{p}_\perp \rangle = \frac{h}{\lambda} \cdot sin\,(\boldsymbol{CoM_r})\ (eq.\ 2.18)$$

Combining eq.2.14 and eq.2.18, the simplified relation between $\boldsymbol{E}_{\perp \mathbf{pc}}$ and $\boldsymbol{CoM_r}$ can be expressed as

$$\boldsymbol{E}_{\perp \mathbf{pc}} = -\frac{v}{ez} \cdot \frac{h}{\lambda} \cdot \sin\,(\boldsymbol{CoM_r})\ (eq.\ 2.19)$$

Thus, the probe-convolved projected electric field $\boldsymbol{E}_{\perp \mathbf{pc}}$ is linearly proportional to the modulus of $\boldsymbol{CoM}_{\boldsymbol{r}}$ shift in the opposite direction. Note that an assumption was made that the intensity distribution of the STEM probe does not change as a function of z, i.e. the sample must be thin enough (1-2 nm), which is inherently suitable for 2D materials.[62] Following Gauss's Law, the divergence of $\boldsymbol{E}_{\perp}$ gives the total charge density ρ

$$div\left[\boldsymbol{E}_{\perp \mathbf{pc}}\right] = \frac{\partial \boldsymbol{E}_{\perp x}}{\partial x} + \frac{\partial \boldsymbol{E}_{\perp y}}{\partial y} = \frac{\rho_{PC}}{\varepsilon_0} (eq.\ 2.20)$$

If the positive nucleus charge can be obtained, then the accurate determination of electron density is also possible, which will help us to understand the nature of bonding. The limiting factor in this technique is the inevitable scan noise from the shift of beam position and specimen drift that obscure the accuracy of calculated divergence.[61] However, the momentum transfer, electric field, and charge density mapping are still very useful for locating light elements even in the presence of heavy atoms, as shown in fig. 2.6, wherein $SrTiO_3$, the oxygen column is still visible.

Electric and magnetic fields can be measured by both DPC segmented detector and pixelated detector, and the benefit of choosing a pixelated detector over segmented detector is the easy and versatile post-processing. First, if there is a relative rotation between the scan coils and the detector, it may be necessary to rotate the CBED patterns, which can only be achieved in data recorded with pixelated detector (though rotation of the CoM shift is also viable, in that case, both detectors are suitable). Second, the segmented detector may fail to differentiate electron events locate differently inside a segment, especially when using small number of segmented detectors, making it less sensitive compared to pixelated detector. Third, 4D-STEM data recorded by pixelated detector can be used for ptychographic phase reconstruction, which cannot be achieved with segmented detector. However, the

photomultiplier tube (PMT) system used in DPC segmented detectors still have the benefit of faster read-out speed over pixelated detector.[59]

Though Müller et al. reported a good accordance between the $\boldsymbol{E}_{\perp \mathbf{pc}}$ map calculated from $\boldsymbol{CoM}_{\boldsymbol{r}}$ and theoretical $\boldsymbol{E}_{\perp}$ calculated from the negative gradient of Coulomb potential (fig. 2.6),[60] subsequent studies have reported a discrepancy of a factor of 2 between the DFT calculated $\boldsymbol{E}_{\perp}$ and the experimental $\boldsymbol{E}_{\perp \mathbf{pc}}$ values.[63,64] Multislice calculation with quantum excitation of phonons (QEP) algorithm was used to simulate CoM using a spatially and temporally incoherent probe has obtained CoM comparable with the experimental CoM. To date, electric field study obtained from DPC and CoM has been performed on single Au atom,[58] GaN,[60] perovskite ($SrTiO_3$,[60] $DyScO_3$,[65] $BiFeO_3$,[66] and $BaTiO_3$[57,67]), MoS_2,[64] graphene,[63] and hBN.[68] Even though these materials have different structures and electronic properties, their $\boldsymbol{E}_{\perp \mathbf{pc}}$ map and charge map exhibit some similarities: the projected electric field drops to a minimum at the atom position, which helps to locate and differentiate light elements, especially in perovskite. Also, defect structure leads to disturbance of local electronic state e.g. studies on graphene[63] and MoS_2[64] showed abnormal electric field magnitude increases at the vacancy site and monolayer/bilayer step edge in graphene.

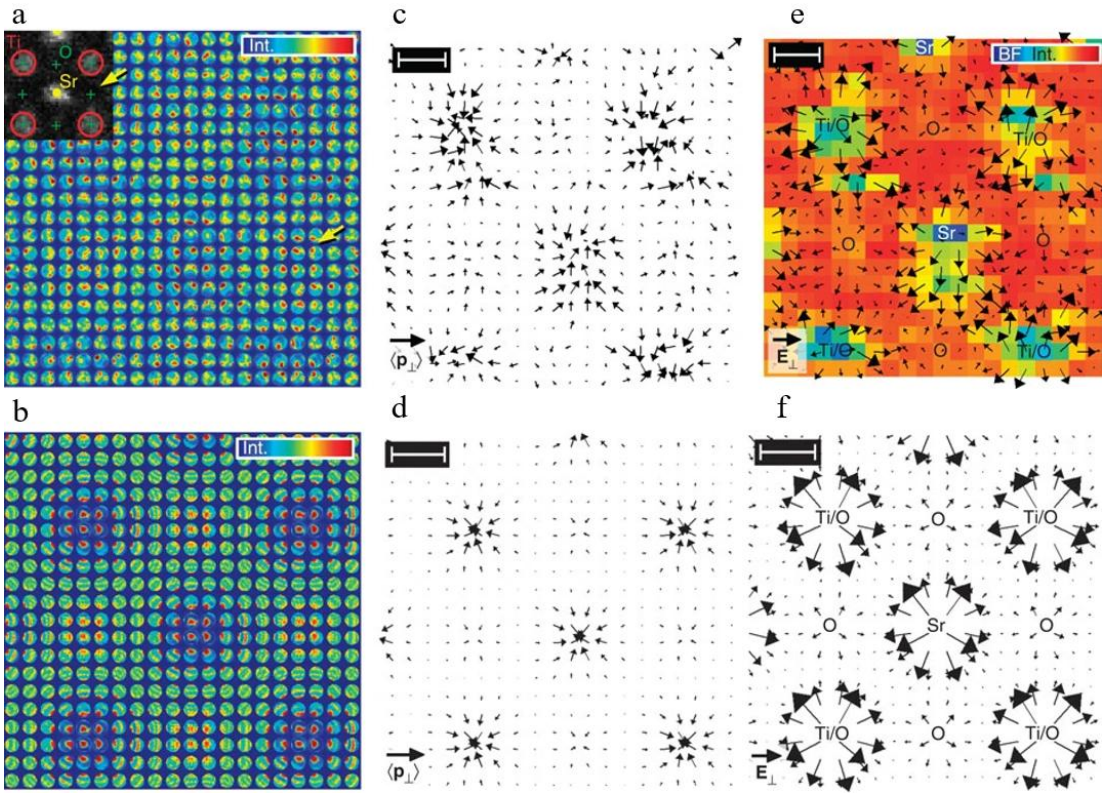


Figure 2.6. Measurement of momentum transfer and electric field of $SrTiO_3$ by 4D-STEM. (a) Experimental and (b) simulated CBED patterns ta each probe position. Inset in (a) shows the atom site in the Z-contrast image. (c) Experimental and (d) simulated momentum transfer calculated from (a) and (b) respectively, the scale bar at the bottom left is 5h/nm. (e) Experimental projected electric field overlaid on the corresponding charge density map. (f) Theoretical projected electric field, the scale bar at the bottom left is 1V/pm.[60] Figures adapted with permission from © Creative Commons Attribution 4.0 International License

2.3.5 Phase retrieval

As discussed in section 2.3.1, the phase of the object transmission function contains information on the local electromagnetic potential and the atomic structure of the specimen, however, the phase information is lost in conventional TEM imaging.

Ptychography is a phase-retrieval method that records the CBED patterns and use computational methods to reconstruct complex electron probe function and sample potential from the overlapping of adjacent CBED patterns,[40,69–71] which can achieve resolution beyond the limit of aperture and lens aberration.[72]

There are two general types of ptychography, non-iterative ptychography, e.g., single side band method (SSB) and Wigner distribution deconvolution (WDD), and iterative ptychography, e.g., extended phase iterative engine (ePIE). Both SSB and WDD used a focused probe, which performs Fourier transform on the recorded CBED patterns to obtain the Fourier overlap function, which is the convolution of the aperture function and the transmission function separated by a spatial frequency. The SSB method recalls the WPOA; thus, the Fourier overlap function can be simplified to be linearly proportional to the interference between direct and two diffracted beams with the positive and negative spatial frequency of the probe position from the direct beam, and the phase can be retrieved by integration from either side of the overlapped direct and diffracted beam.[48,49]

WDD does not require WPOA, it first performs an inverse Fourier transform on the Fourier overlap function with respect to the scattering vector which gives the product of two integrals that are the Wigner distribution function of probe function and object transmission function, respectively. These two terms are separated by Wiener deconvolution, and the Wigner distribution function of object transmission function is inverse Fourier transformed with respect to real-space probe position, and the transmission function at a given spatial frequency of the probe position with respect to the scattering angle origin and spatial frequency origin can be obtained.[73]

In STEM, the iterative method ePIE can be performed using either focused or defocused probe, and the resolution depends on the overlap of the probe positions in real space. It first assumes an ideal probe and object transmission function, iteratively corrects the functions to minimize the difference, and finally obtains an aberration-free transmission function.[74,75] If only the BFD is used, the ptychographic phase obtained by WDD and ePIE is comparable at the same electron dose (fig. 2.7). A deeper resolution can be achieved by ePIE when a larger angular range of diffracted beams is used.[76,77]

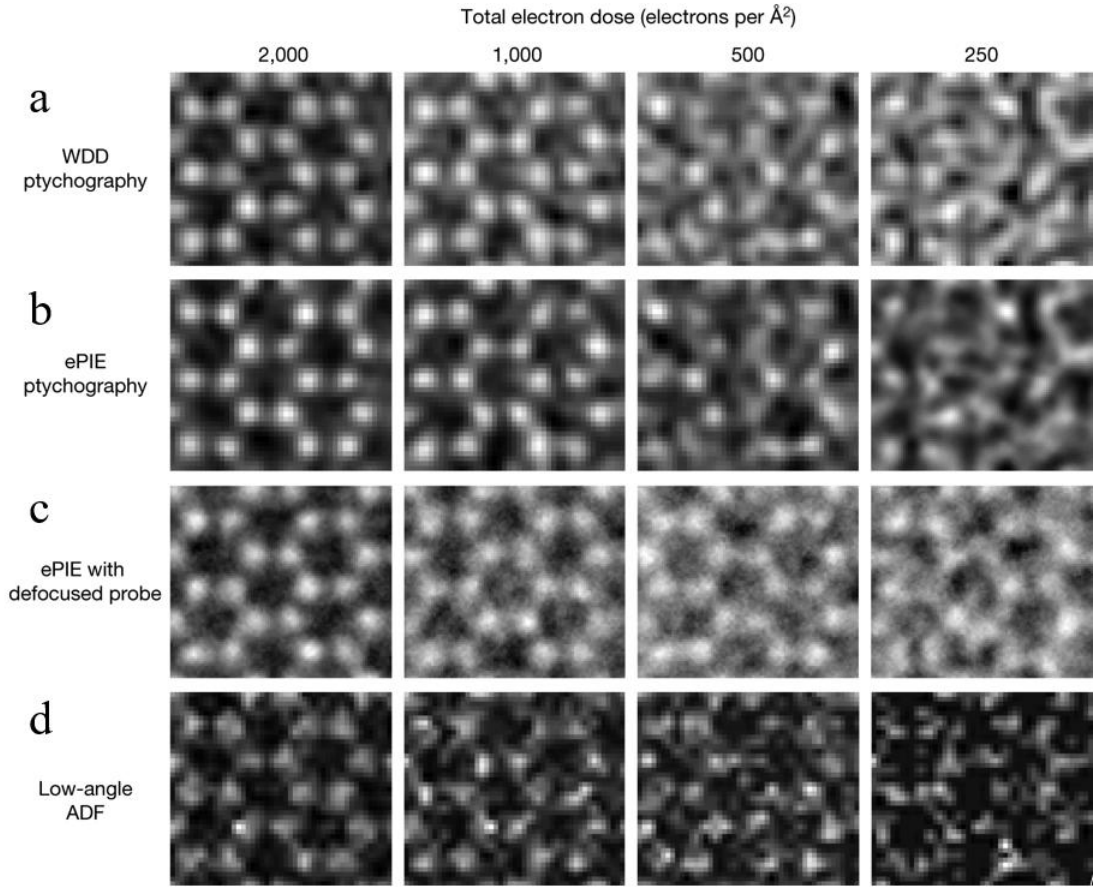


Figure 2.7. Comparison of different ptychography methods and LAADF-STEM as a function of electron dose.[77] Figures adapted with permission from © 2018 Macmillan Publishers Ltd., part of Springer Nature

Another phase retrieval method that can be achieved by 4D-STEM is integrated DPC (iDPC).[78,79] The basic idea of DPC and CoM shift from 4D-STEM data set are similar, but DPC is comparatively less sensitive to thin polycrystalline materials,[80] and pixelated detector provide better detection ability to small deflection and an overall better result.[81] The phase retrieved by integrated CoM (iCoM) is very close to ptychographic phase when both methods use only the BFD, and when the ePIE ptychography uses a larger angular range, e.g. 5α, the resolution is largely improved and differs from iCoM, but still, iCoM is a quick and simple method to retrieve phase.

2.3.6 Virtual Detector

The idea of post-session reconstruction is a mimic of the ADF detector. In conventional ADF-STEM imaging, scattered electrons hit the scintillator and were converted to photons due to the luminescence effect, the photons will then be guided into the photomultiplier tube (PMT) and amplified. The final signal is an integration over the dwell time and should not be taken as the number of electrons detected.[82] Using imaging processing and analysing code, the post-session integration can be carried out with user choice of detector angular range, thus from a full CBED pattern, imaging modes including HAADF-, BF-, LAADF/MAADF-, and ABF-STEM,[65,81] as shown in fig. 2.8. The incoherent Z-contrast HAADF-STEM can be used in conjunction with coherent phase reconstruction from the 4D data set, which showed high sensitivity in the detection of low atomic number elements.[83,84] In chapter 4 and 5, ‘phase’ will be calculated from the iCoM for ease of calculation as well as for the fine difference between iCoM and phase reconstruction when only using the BFD.

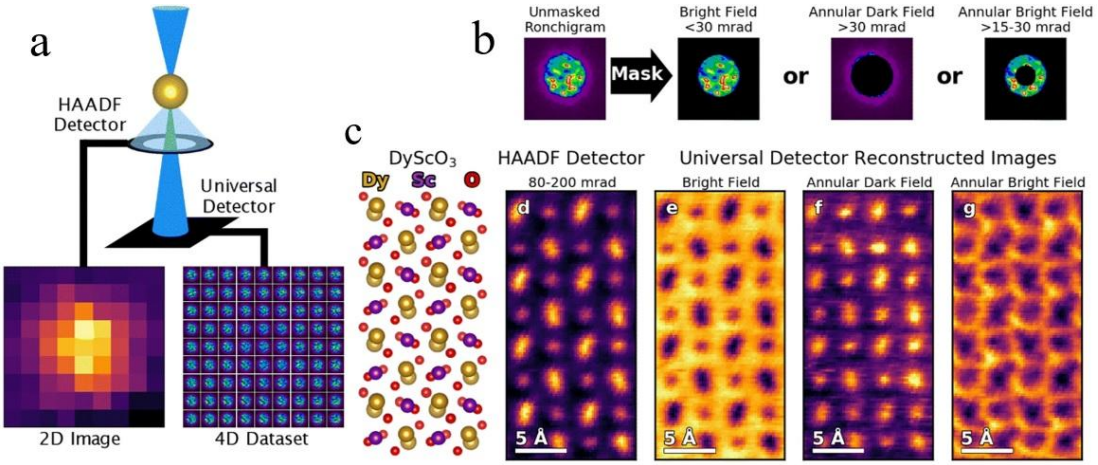


Figure 2.8. Various types of STEM image reconstruction from 4D data set of $DyScO_3$. (a) Schematics showing a 2D ADF-STEM image obtained from the HAADF detector and the simultaneous CBED pattered recorded by a pixelated detector. (b) Imaging mode reconstructed from selective angular range by masking, ranging from unmasked CBED pattern, BF, ADF, and ABF. (c) Crystal model of $DyScO_3$, (d) corresponding HAADF-STEM images, and (e-g) reconstructed BF-, ADF-, and ABF-STEM images, respectively.[65] Figures adapted with permission from © Creative Commons Attribution 4.0 International License

2.4 In-situ Defect Evolution in 2D TMDs

2D materials have superior properties, but in practice, the crystals are rarely perfect, especially at nanoscale. Crystallographic defects formed during synthesis will scatter charge carriers which largely decrease the carrier mobility in the materials, but these nanostructures may also bring unusual modifications. When the specimen is loaded into an electron microscope and irradiated, contamination and beam damage will promote intriguing in-situ defect evolution. Thus, it is essential to understand the formation and evolution of these defects, so one can avoid or utilize these defect structures in device fabrication. For example, the absence of band gap in graphene is

not beneficial for its application in the electronic device, but its electronic properties may be engineered by introducing structural defects into the graphene lattice. In this chapter, the irradiation damage will be listed and explained, followed by common types of defects in graphene and TMDs and their *in situ* evolution. Methods to minimize and utilize these beam-induced defects will be provided.

2.4.1 Electron beam damage and mechanisms

During electron microscopy imaging, high-energy electron irradiation may cause damage to the specimen. There are generally 6 types of electron-beam irradiation damage that may occur in graphene and TMD specimens and leads to final structural destruction: generation of secondary electrons and electrostatic charging, heating, radiolysis, knock-on displacement, surface contamination, and surface etching.

Electrostatic charging and **specimen heating** usually happen in a less thermal and electrical conducting specimens, e.g., in hBN, where secondary electrons severely charge the sample and such electrostatic repulsion finally disassembles the specimen, as referred to as 'coulomb explosion'.[85] Generally, this can be eased with decreasing incident current density and conductive coating.[86]

Radiolysis, or ionization damage, is caused by inelastic scattering between the atomic electron cloud and incident electrons, which breaks the chemical bonds and causes ionization. It is the predominant damaging mechanism in insulators, semiconductors, and organic specimen and will be promoted under high temperatures.[87,88] Radiolysis can be reduced by using a high accelerating voltage to decrease the cross-section for the inelastic electron interactions. Thinner specimens also reduce radiolysis if such thickness is shorter than the mean-free path of the inelastic interaction.[25]

Knock-on displacement happens when the energetic incident electron directly collided with an atom, which causes atom displacements and electron-beam sputtering near surface.[88] It is the dominant damaging mechanism in conducting specimens (e.g., graphene). Intuitively, lower the beam energy will reduce knock-on damage, but compromise the resolution due to increased wavelength of the electrons. 60-80 kV is often pursued for TMDs because 1) to reduce knock-on displacement and 2) to increase signal for HAADF-STEM, as a lower accelerating voltage gives a higher scattering cross section, resulting in more scattering events, as an electron with less energy will be more prone to be scattered by nuclei. For each element, there is an energy threshold, beyond which displacement will occur. For the S atom in pristine MoS_2, the threshold is about 6.5eV, about the same as the maximum knock-on energy under 80kV irradiation. However, it should be noted that at 60kV the energy transferred is ~ 4.3eV,[89] lower than the threshold energy, but sputtering of surface S atoms may still occur.[25] However, radiolysis worsens with lower accelerating voltage,[25,38] thus the choice of accelerating voltage is a compromise between knock-on displacement and radiolysis. Materials that do not suffer from radiolysis e.g. graphene and hBN may be preferentially imaged at low accelerating voltage.[86]

Besides aforementioned methods, there are several other ways to stop electron beam damage:

Electron dose: electron dose D_{image} is often used to evaluate the beam damage by calculating the accumulative electrons interacted with the specimen during the course of imaging, adapted from reference[38]

$$D_{image} = I_{beam} NM\Delta t/A \quad (eq.\ 2.21)$$

where D_{image} is the dose experienced by the specimen during an image acquisition, I_{beam} is the beam current, N and M are the number of pixels along x and y direction in such image, Δt is the dwell time in each pixel, A is the area imaged. Dose is an indication of beam damage as well as signal to noise ratio (SNR), lowering the dose will reduce beam damage but sacrifices the SNR of the obtained image.

Beam blanking: deflect the beam when not imaging the sample to reduce unnecessary beam damage.

Encapsulation. It was found that in bilayer graphene, the bottom layer has fewer irradiation-induced vacancies than the top layer. Studies by Kaiser et al.[90] and Novoselov et al.[91] demonstrated that using an additional layer of graphene under MoS_2, or using a sandwich structure e.g. Gr-MoS_2-Gr, greatly reduced electron beam damage in 80kV TEM and 60kV STEM, in the same fashion as traditionally used gold coating, as they both have great thermal and electrical conductivity. Graphene is also chosen for 2D TMDs for its crystallinity which facilitates post-session Fourier-filtering.[90,91]

In TMDs, the beam damaging mechanism can be a mix of ionization damage and knock-on displacement,[92] while graphene mainly suffer from knock-on displacement. Irradiation-induced vacancies, line defects, and holes act as traps and hinder the electron transport, which is detrimental for electronic applications, as they scatter charge carriers thus reducing the electrical and thermal conductivity, [93] but they also have interesting properties like induced magnetism.[94] One can manipulate defect forming process by using a focused probe down to sub-A size, which acts as atomic tweezers that selectively sputter atom(s)[95,96] to achieve tailoring target atomic structure, which requires a detailed understanding of the defect structure, and hence the purpose of the following sections.

2.4.2 Point and Line Vacancy

In 2D materials, point and line defects may be the simplest type of defects. Vacancies mean loss of native atom(s). They are formed either during imperfect synthesis [97] or under irradiation and chemical etching. In graphene, the loss of one C atom leads to atomic reconstruction into a 5-9 ring, leaving one unsaturated atom. Loss of two C atoms leads to a reconstruction into a 5-8-5 configuration with no dangling bonds. In MoS_2 and WS_2, point vacancies are either missing S atom or metal atom (fig. 2.9a). In TMDs, S atoms are always preferentially sputtered over metal atoms with higher atomic mass,[98] and it is the same case for the heavier Se atoms.[92] Single S vacancy (V_S) does not affect the lattice much, while double S vacancy (V_{S2}) induces bond contraction.[99] Vacancies can be annealed by high temperatures and carbon sources. They may also be filled with mobile atoms or agglomerate to form a line S vacancies (LV),[97,100] the latter case is usually irreversible. This is supported by the fact that around an expanding LV, the number of V_S always has a sharp decrease.[97]

In an irradiated region, usually several LVs are present at the same time, and their direction may be affected by the lattice strain presented,[97] indicating they can be intentionally produced by introducing external strain. These defects also introduce intrinsic strain via lattice deformation. The strain (isotropic contraction) around S vacancies induced high magnetic moment, similar to chemically incorporated metallic 1T-phase into diamagnetic 2H-phase. Along LVs, the contraction is most evident perpendicular to the direction of the line (fig. 2.9d), with increased conductivity along the line direction due to the defect band overlapping the band gap (i.e., metallic). These vacancies tend to be filled with foreign atoms like C, N, and O

from ambient environment. More candidates from non-metal and halogen group showed the potential of acceptor/donor doping.

In terms of the side view of a LV, the S atoms are always arranged in the 'staggered' configuration, this causes minimum bending in the monolayer and is calculated to be energetically favoured,[97] however, it is hard to determine whether the vacancies are formed on the top or bottom atomic layer either in TEM or STEM, as the side view is perpendicular to the beam direction.

Another type of point defect is bond rotation, which does not change the stoichiometry of the lattice and does not create dangling bonds. In graphene, Stone-Wales defect is formed due to a 90° bond rotation of a C-C bonding.[101] In TMDs, the 60° M-X bond rotation is compatible with TMDs' trigonal lattice symmetry, with the simplest form of trefoil, which later evolved to an 8-5-5-8-membered ring domain boundary, as shown in fig. 2.9f-i.[93] Note that bond rotation is observed in a range of TMDs but has not yet been found in MoS_2.

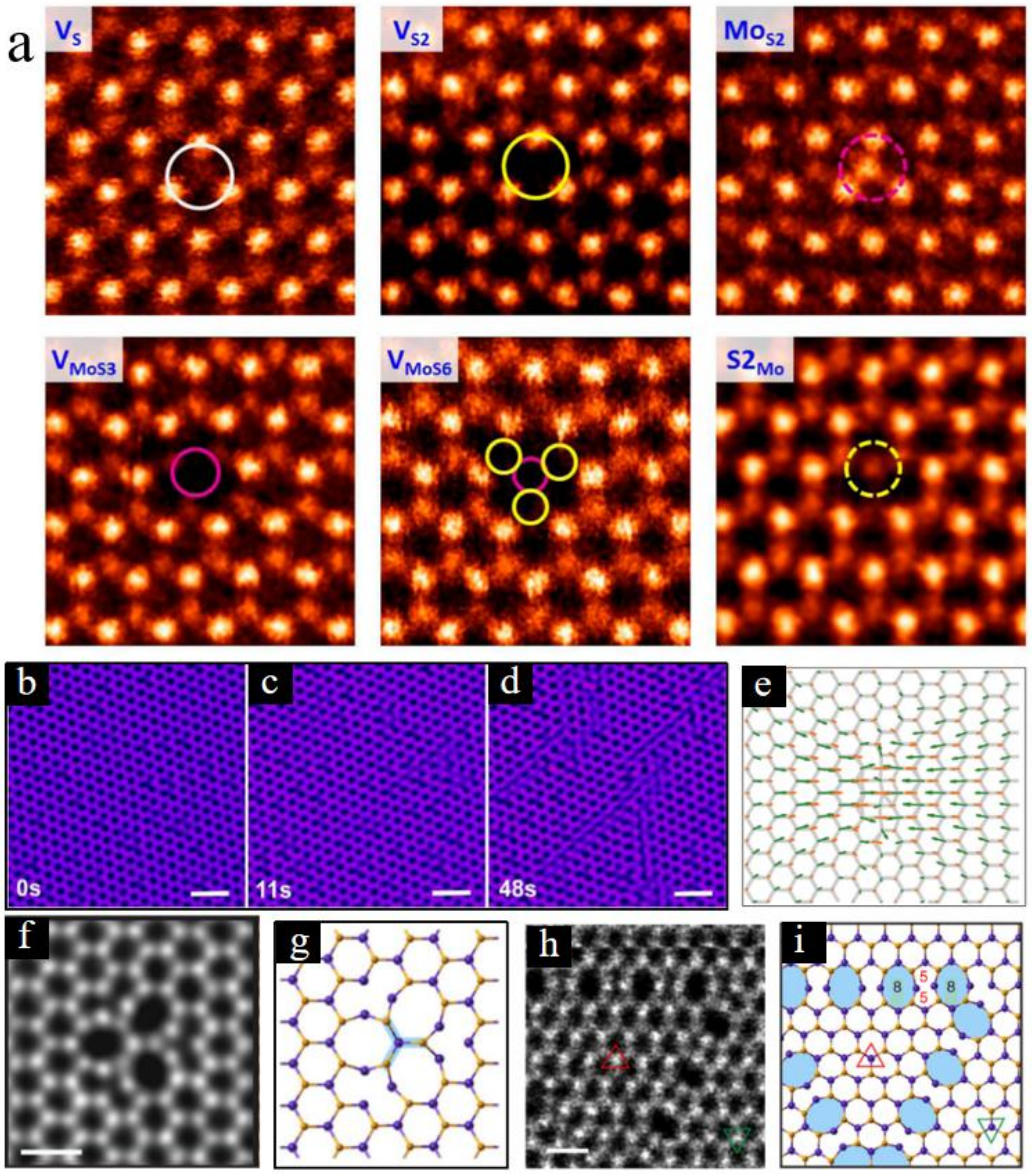


Figure 2.9. Point defects and their evolution. (a) High resolution ADF-STEM images of intrinsic point defects in monolayer MoS_2, V_S indicates single sulphur vacancy, V_{S2} indicates double sulphur vacancy, Mo_{S2} indicates antisite Mo atom substitution at a di-sulphur vacancy, V_{MoS3} indicates Mo vacancy with three nearby mono-sulphur vacancy, V_{MoS6} indicates Mo vacancy with three nearby disulphur vacancy, and $S2_{Mo}$ indicates a 2S column substituting a Mo vacancy.[102] (b-d) Agglomeration of S vacancies under continuous irradiation and formation of several line sulphur vacancy (LV) after 48 s, scale bar indicates 0.5 nm.[100] (e) Strain field around a double LV, arrows represent atom displacement.[97] (f) Trefoil bond rotation in WSe_2, scale bar 0.5 nm, (h) 8-5-5-8-membered ring domain boundary, scale bar

0.5 nm, (f) and (h) corresponding crystal models of panel f and h, respectively.[93] Figures adapted with permission from: (a) ref 102, © 2013 American Chemical Society (b-d) ref 100, © 2016 American Chemical Society (e) ref 97, © 2013 American Physical Society (f-i) ref 93, © Creative Commons Attribution 4.0 International License

2.4.3 Nanopore, Hole, and Hole Edge

The *in situ* formation of holes is always due to continuous irradiation. Most holes will continue to grow (destruction of lattice) under irradiation, as the S vacancies migrate to the hole edge. This damaging process can also be utilized to create a sub-nm pore with proximity if the probe is focused down to sub- Å size.[96] In MoS_2, for instance, the Mo atom is much more stable under irradiation compared to the S atom,[98] thus the formation of such a pore involves sputtering the Mo atoms and all six surrounding S atoms. The Mo atom will then jump between the energetically favourable pore edge and its original position, and finally resides around the pore edge[73]. The formation of such nanopore is pursued due to its wide application as a membrane for water desalination, gas separation, and DNA transportation.[103–107]

Another interesting aspect of a hole is its edge. In graphene, there are two edge terminations, zigzag and armchair. These two terminations show comparable activation energy thus the hole edge is a mixture of both and rarely flat. In TMDs, zigzag and armchair are possible edge terminations and DFT calculation revealed that the zigzag termination is energetically preferred in MoS_2 and WS_2, and it has intriguing magnetic and metallic properties arising from the discontinuity of interface.[108] Annealing MoS_2 at 800°C in vacuum leads to the creation of atomically flat zigzag hole edge at the scale of tens of nanometres.[109] Atomic resolution STEM imaging showed that if it is an S-terminated zigzag edge, the 2S atoms will be

replaced by Mo atoms and form temporal Mo-Mo bonding, forming a slightly elongated hexagonal (fig. 2.10a, b).[109] This can be an alternative way of fabricating nanoribbons.

Nowadays, the fabrication methods for large-scale ribbons (which have two edges) used in devices are mainly top-down methods e.g. electron beam lithography (EBL) patterning from 2D samples, but once the resulting ribbon width is downsized, it becomes increasingly unstable,[110] and from bottom up, through epitaxial growth.[111] Cheng et al. recently reported a controlled growth of $MoSe_2$ ribbon by pre-patterning evaporated Se on Au, yielding ribbons of aspect ratio up to 100, width down to 0.7nm, and zigzag terminated edges.[112] The ribbons remained stable when attached to the Au substrate, however, the author didn't discuss their stability after detaching and for further application.

Nanoribbons can also be fabricated *in situ*. Under beam irradiation, as holes continue to expand, lattice between adjacent holes deconstructs and through a phase transition, forming a highly-crystalline ribbon, in the case of MoS_2, with a stoichiometry of Mo_5S_4, and the formation of such nanoribbons is theoretically feasible for other TMDs.[110] These ribbons have uniform geometry, width down to 0.35nm, with a theoretical band gap of 0.77 eV, showing a pathway to in-situ fabrication of sub-10 nm nano-ribbons.[113] However, it is still tricky to control the initial geometry of the hole to achieve batch fabrication of such ribbons.

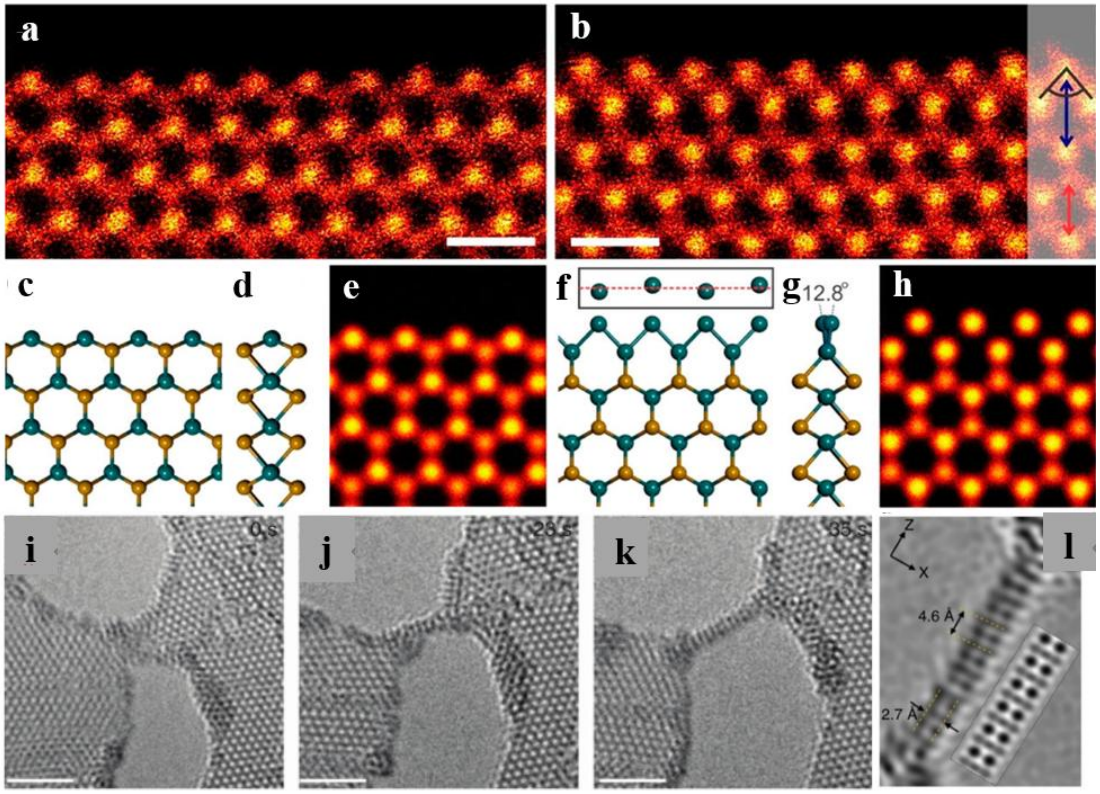


Figure 2.10. (a) Mo-terminated zig-zag edge and (b) Mo replaced S-terminated zig-zag edge, (c) and (f) are corresponding crystal models, (d) and (g) are their side view, (e) and (h) are multislice simulation based on the model in (c) and (f).[109] (i-k) Evolution of region between two adjacent holes, and (l) zoomed-in of the final Mo_5S_4 nano-ribbon.[113] Figures adapted with permission from: (a-h) ref 109, © 2017 American Chemical Society (i-l) ref 113, © Creative Commons Attribution-NonCommercial-ShareAlike 3.0 Unported License

2.4.4 Dopants and Nanocrystal

The band gap of the semiconducting TMDs can be effectively tuned by doping and alloying. Intentional doping is done by incorporating groups of metal species that are close to the transition metals for a small lattice mismatch thus the original crystal structure was rarely abrupted and formed stable substitutional dopants. Mn and Re are group VII elements that facilitate n-type doping by introducing an extra d-orbital

valence electron. Similarly, group V element Nb facilitates p-type doping. Unintentional doping from foreign species from MoO_3 precursors e.g., Cr and V are incorporated into the lattice during the CVD synthesis. They act as substitutional dopants of the metal atoms.[114] These dopants are very stable under irradiation and elevated temperature. One can easily spot such dopants in Z-contrast STEM images, but the determination of such dopants with single atom precision is challenging and often requires either EELS or ADF-STEM image simulation.[115]

2D materials comprise a large surface area, which made them ideal for catalyst loading. As shown in fig. 2.10a, Pt nanocrystals were loaded onto MoS_2 (which also shows HER catalytic behaviour[116,117]) via solution phase epitaxial growing and in-situ annealing for their synergistic catalytic ability for HER.[118] The annealing process with the presence of Pt will etch the lattice, and sometimes the Mo atoms will be incorporated into the Pt nanocrystal.[118] The diffusing Pt atoms may also be trapped by S vacancies, and subsequently lost their catalytic properties (fig. 2.11b).[115]

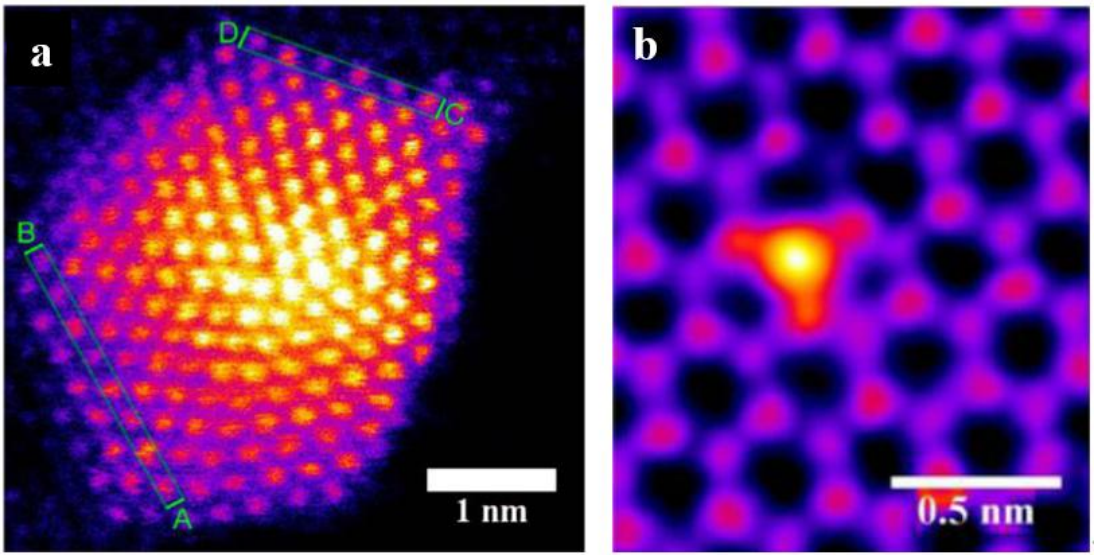


Figure 2.11. (a) Epitaxial growth of Pt nanocrystal[118] and (b) single Pt atom incorporated in MoS_2 lattice.[115] Figures adapted with permission from (a) ref 118, © 2017 American Chemical Society and (b) ref 115, © 2017 American Chemical Society

2.4.5 Contamination

The main source of contamination is the carbon-based contamination introduced during the transfer process (fig. 2.12a) which is present in an ADF-STEM image as contrast variation which can obscure subsequent analysing.[19,119] A pre-session vacuum annealing with optional activated carbon is sufficient to remove most of the hydrocarbon contamination. During imaging, the sample is charged by incident electron, this increases energy and attracts carbon contamination and is shown as a bright region, same as the imaging window, at beam position. Normally, in practice, people use a beam shower, which is to raster the chosen area with a beam (lower intensity). The comparatively easier way is to heat the sample in the chamber with an *in situ* heating chip, with simple steps such as blanking the beam, while elevating the temperature (up to 700°C for MoS_2, depending on the robustness of the specimen).[109] This is basically the same as vacuum annealing but is much more efficient. The action to deflect the beam is to prevent amorphous carbon from turning into graphitic carbon due to the duet of 'beam energy' and 'annealing', and it is much harder to remove graphitic carbon once it is pinned at specimen edges. However, it is found that the foreign dopant atoms tend to sit on these contamination layers, which might open a possibility for catalyst loading.

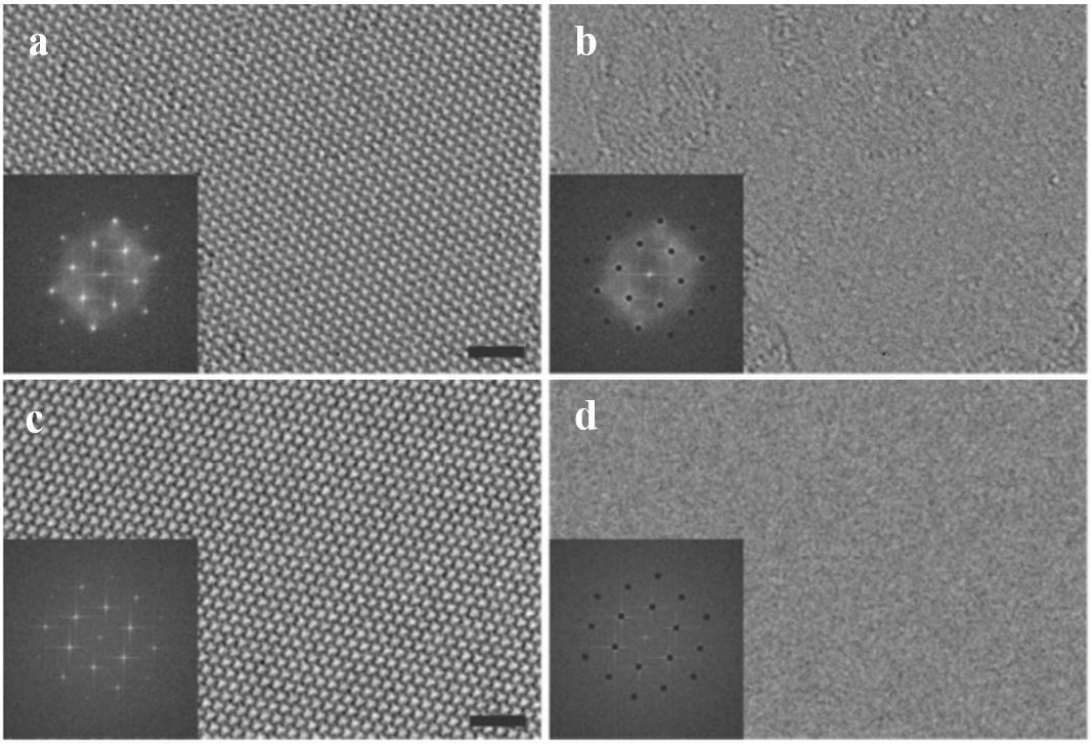


Figure 2.12. AC-TEM image of MoS_2 at (a) room temperature and (c) 800°C, and the corresponding hydrocarbon contamination (b) and (d) obtained by inversed fast Fourier transform (FFT) with the removal of MoS_2 spectrum, showing substantial contamination removal with in-situ annealing, with inset showing corresponding FFT spectrum.[119] Figures adapted with permission from © 2017 American Chemical Society

2.5 Conclusion

The family of 2D materials, or more specifically, van der Waals layered materials include single elements e.g. black phosphor (phosphorene)[120,121] and silicene[122], hexagonal boron nitride,[9] graphitic carbon nitride,[123] transition-metal carbide and nitride (MXene),[124] III−VI layered semiconductors, layered double hydroxide,[125] metal oxide e.g. MoO_3[126] and α-V_2O_5[127], and many others. Among them, the 2D TMD family is the most studied and has a well-developed synthesis and device fabrication process.[128] To date, most applications are still confined to pristine, undamaged TMD materials (except for nanoribbons and nanopore, which has been explored for biomedical detection[129] and 1D electronics application[130,131]), where the various atomic-scale defects have exhibited intriguing behaviour and require more mechanistic studies. In-situ heating and biasing electron microscopy have proposed a convenient method of studying those defects and *in situ* nanofabrication, though the immediate problem would be scaling.

To date, the explorations of the powerful 4D-STEM technique are still focusing on a pristine lattice or micron-scale magnetic domain mapping, and there is no detailed analysis of atomic electro-magnetic mapping of 2D TMDs, the materials that had already shown intriguing behaviour in in-situ defect evolution and DFT calculations. The intuitive thought would be to combine atomic resolution in-situ (S)TEM with 4D-STEM to experimentally verify these theories and give insight into manipulating these defects efficiently. The drawback might be the extended acquisition time compared to common ADF-STEM imaging, which is not suitable for studying transient changes in defect evolution. Nevertheless, this combination still has great potential, not only for 2D TMDs, but also for the whole 2D materials family, and should receive more attention and further study.

References

1. Novoselov, K. S. *et al.* Two-dimensional atomic crystals. *Proc. Natl. Acad. Sci.* **102**, 10451–10453 (2005).
2. GEIM, A. K. & NOVOSELOV, K. S. The rise of graphene PROGRESS. *Nat. Mater.* **6**, 183–191 (2007).
3. Geim, A. K. & Grigorieva, I. V. Van der Waals heterostructures. *Nature* **499**, 419–425 (2013).
4. Zhu, Z. Y., Cheng, Y. C. & Schwingenschlögl, U. Giant spin-orbit-induced spin splitting in two-dimensional transition-metal dichalcogenide semiconductors. *Phys. Rev. B - Condens. Matter Mater. Phys.* **84**, 1–5 (2011).
5. Kuc, A., Zibouche, N. & Heine, T. Influence of quantum confinement on the electronic structure of the transition metal sulfide TS2. *Phys. Rev. B - Condens. Matter Mater. Phys.* **83**, 1–4 (2011).
6. Ding, Y. *et al.* First principles study of structural, vibrational and electronic properties of graphene-like MX2(M=Mo, Nb, W, Ta; X=S, Se, Te) monolayers. *Phys. B Condens. Matter* **406**, 2254–2260 (2011).
7. Ma, Y. *et al.* Evidence of the existence of magnetism in pristine VX 2 monolayers (X = S, Se) and their strain-induced tunable magnetic properties. *ACS Nano* **6**, 1695–1701 (2012).
8. Ataca, C., Şahin, H. & Ciraci, S. Stable, single-layer MX 2 transition-metal oxides and dichalcogenides in a honeycomb-like structure. *J. Phys. Chem. C* **116**, 8983–8999 (2012).
9. Geick, R., Perry, C. & Rupprecht, G. Normal Modes in Hexagonal Boron Nitride. *Phys. Rev.* **146**, 543–547 (1966).
10. Wang, S., Sawada, H., Allen, C. S., Kirkland, A. I. & Warner, J. H. Orientation dependent interlayer stacking structure in bilayer MoS $_2$ domains. *Nanoscale* 13060–13068 (2017). doi:10.1039/C7NR03198J
11. Song, I., Park, C. & Choi, H. C. Synthesis and properties of molybdenum disulphide: from bulk to atomic layers. *RSC Adv.* **5**, 7495–7514 (2015).
12. Radisavljevic, B., Radenovic, A., Brivio, J., Giacometti, V. & Kis, A. Single-layer MoS2 transistors. *Nat. Nanotechnol.* **6**, 147–150 (2011).
13. Splendiani, A. *et al.* Emerging photoluminescence in monolayer MoS2. *Nano Lett.* **10**, 1271–1275 (2010).
14. Wang, Q. H., Kalantar-Zadeh, K., Kis, A., Coleman, J. N. & Strano, M. S. Electronics and optoelectronics of two-dimensional transition metal dichalcogenides. *Nat. Nanotechnol.* **7**, 699–712 (2012).
15. Schaibley, J. R. *et al.* Valleytronics in 2D materials. *Nat. Rev. Mater.* **1**, 1–15 (2016).

16. Li, S. *et al.* Edge-Enriched 2D MoS $_2$ Thin Films Grown by Chemical Vapor Deposition for Enhanced Catalytic Performance. *ACS Catal.* **7**, 877–886 (2017).
17. Manzeli, S., Ovchinnikov, D., Pasquier, D., Yazyev, O. V. & Kis, A. 2D transition metal dichalcogenides. *Nat. Rev. Mater.* **2**, (2017).
18. Li, H., Wu, J., Yin, Z. & Zhang, H. Preparation and applications of mechanically exfoliated single-layer and multilayer MoS2 and WSe2 nanosheets. *Acc. Chem. Res.* **47**, 1067–1075 (2014).
19. Shi, Y., Li, H. & Li, L.-J. Recent advances in controlled synthesis of two-dimensional transition metal dichalcogenides via vapour deposition techniques. *Chem. Soc. Rev.* **44**, 2744–2756 (2015).
20. Wang, X., Feng, H., Wu, Y. & Jiao, L. Controlled Synthesis of Highly Crystalline MoS 2 Flakes by Chemical Vapor Deposition. *J. Am. Chem. Soc.* **135**, 5304–5307 (2013).
21. Liu, K. K. *et al.* Growth of large-area and highly crystalline MoS2 thin layers on insulating substrates. *Nano Lett.* **12**, 1538–1544 (2012).
22. Shi, Y. *et al.* van der Waals Epitaxy of MoS $_2$ Layers Using Graphene As Growth Templates. *Nano Lett.* **12**, 2784–2791 (2012).
23. Mujib, S. Bin, Ren, Z., Mukherjee, S., Soares, D. M. & Singh, G. Design, characterization, and application of elemental 2D materials for electrochemical energy storage, sensing, and catalysis. *Mater. Adv.* **1**, 2562–2591 (2020).
24. Thomas, J. M., Ducati, C., Leary, R. & Midgley, P. A. Some turning points in the chemical electron microscopic study of heterogeneous catalysts. *ChemCatChem* **5**, 2560–2579 (2013).
25. Williams, D. B. & Carter, C. B. *Transmission Electron Microscopy: A Textbook for Materials Science*. *Materials Science* **1**–**4**, (2009).
26. Spence, J. C. H. High-Resolution Electron Microscopy. (2013). doi:10.1093/acprof:oso/9780199668632.001.0001
27. Zernike, F. Phase contrast, a new method for the microscopic observation of transparent objects. *Physica* **9**, 686–698 (1942).
28. Crewe, A. V., Wall, J. & Langmore, J. Visibility of Single Atoms. *Science (80-.).* **168**, 1338–1340 (1970).
29. Findlay, S. D. *et al.* Dynamics of annular bright field imaging in scanning transmission electron microscopy. *Ultramicroscopy* **110**, 903–923 (2010).
30. Okunishi, E., Sawada, H. & Kondo, Y. Experimental study of annular bright field (ABF) imaging using aberration-corrected scanning transmission electron microscopy (STEM). *Micron* **43**, 538–544 (2012).
31. Dinges, C., Kohl, H. & Rose, H. High-resolution imaging of crystalline objects by hollow-cone illumination. *Ultramicroscopy* **55**, 91–100 (1994).
32. Ishikawa, R. *et al.* Direct imaging of hydrogen-atom columns in a crystal by annular bright-field electron microscopy. *Nat. Mater.* **10**, 278–281 (2011).
33. Batson, P. E. Simultaneous STEM imaging and electron energy-loss

spectroscopy with atomic-column sensitivity. *Nature* **366**, 727–728 (1993).
34. Enache, D. I. *et al.* Solvent-free oxidation of primary alcohols to aldehydes using Au-Pd/TiO2 catalyst. *Science (80-.).* **311**, 362–365 (2006).
35. Krause, F. F. & Rosenauer, A. Reciprocity relations in transmission electron microscopy: A rigorous derivation. *Micron* **92**, 1–5 (2017).
36. Lichte, H., Geiger, D. & Linck, M. Off-axis electron holography in an aberration-corrected transmission electron microscope. *Philos. Trans. R. Soc. A Math. Phys. Eng. Sci.* **367**, 3773–3793 (2009).
37. ePSIC. https://confluence.diamond.ac.uk/display/epsicweb/epsic. (2019).
38. Pennycook, S. J. & Nellist, P. D. *Scanning Transmission Electron Microscopy*. *Springer* (2011).
39. Zewail, A. H. 4D Ultrafast Electron Diffraction, Crystallography, and Microscopy. *Annu. Rev. Phys. Chem.* **57**, 65–103 (2006).
40. Ophus, C. Four-Dimensional Scanning Transmission Electron Microscopy (4D-STEM): From Scanning Nanodiffraction to Ptychography and Beyond. *Microsc. Microanal.* **25**, 563–582 (2019).
41. J. M. Rodenburg, B. C. McCallum & P. D. Nellist. Experimental tests on double-resolution coherent imaging via STEM. *Ultramicroscopy* **48**, 304–314 (1993).
42. Simson, M. *et al.* 4D-STEM Imaging With the pnCCD (S)TEM-Camera. *Microsc. Microanal.* **21**, 2211–2212 (2015).
43. Yang, H. *et al.* 4D STEM: High efficiency phase contrast imaging using a fast pixelated detector. *J. Phys. Conf. Ser.* **644**, (2015).
44. Mendis, S. K. *et al.* CMOS active pixel image sensors for highly integrated imaging systems. *IEEE J. Solid-State Circuits* **32**, 187–196 (1997).
45. Milazzo, A. C. *et al.* Active pixel sensor array as a detector for electron microscopy. *Ultramicroscopy* **104**, 152–159 (2005).
46. Caswell, T. A. *et al.* A high-speed area detector for novel imaging techniques in a scanning transmission electron microscope. *Ultramicroscopy* **109**, 304–311 (2009).
47. Ophus, C., Ercius, P., Sarahan, M., Czarnik, C. & Ciston, J. Recording and Using 4D-STEM Datasets in Materials Science. *Microsc. Soc. Am.* **20**, (2014).
48. Yang, H., Pennycook, T. J. & Nellist, P. D. Efficient phase contrast imaging in STEM using a pixelated detector. Part II: Optimisation of imaging conditions. *Ultramicroscopy* **151**, 232–239 (2015).
49. Pennycook, T. J. *et al.* Efficient phase contrast imaging in STEM using a pixelated detector. Part 1: Experimental demonstration at atomic resolution. *Ultramicroscopy* **151**, 160–167 (2015).
50. Waddell, E. M., Chapman, J. N. & Ferrier, R. P. Linear imaging of strong phase objects by differential phase contrast. *Proc. Inst. Phys. Electron Microsc. Anal. Gr.* **36**, 267–270 (1977).
51. Waddell, E. M. & Chapman, J. N. Linear Imaging of Strong Phase Objects Using Asymmetrical Detectors in Stem. *Opt.* **54**, 83–96 (1979).

52. Dekkers, N. H. & Lang, H. d. Differential Phase Contrast in a STEM. *Optik (Stuttg).* **41**, 452–456 (1974).
53. Rose, H. Nonstandard imaging methods in electron microscopy. *Ultramicroscopy* **2**, 251–267 (1976).
54. Chapman, J. N. The investigation of magnetic domain structures in thin foils by electron microscopy. *J. Phys. D. Appl. Phys.* **17**, 623–647 (1984).
55. Chapman, J. N. & Morrison, G. R. Quantitative determination of magnetisation distributions in domains and domain walls by scanning transmission electron microscopy. *J. Magn. Magn. Mater.* **35**, 254–260 (1983).
56. Chapman, J. N., Morrison, G. R., Jakubovics, J. P. & Taylor, R. A. Determination of domain wall structures in thin foils of soft magnetic alloy. *J. Magn. Magn. Mater.* **49**, 277–285 (1985).
57. Shibata, N. *et al.* Differential phase-contrast microscopy at atomic resolution. *Nat. Phys.* **8**, 611–615 (2012).
58. Shibata, N. *et al.* Electric field imaging of single atoms. *Nat. Commun.* **8:15631**, (2017).
59. Shibata, N. *et al.* Direct Visualization of Local Electromagnetic Field Structures by Scanning Transmission Electron Microscopy. *Acc. Chem. Res.* **50**, 1502−1512 (2017).
60. Müller, K. *et al.* Atomic electric fields revealed by a quantum mechanical approach to electron picodiffraction. *Nat. Commun.* **5:5653**, (2014).
61. Müller-Caspary, K. *et al.* Measurement of atomic electric fields and charge densities from average momentum transfers using scanning transmission electron microscopy. *Ultramicroscopy* **178**, 62–80 (2017).
62. Müller, K. *et al.* Supplementary Note 1 Supplementary Note 2. **2**, 1–6 (2014).
63. Ishikawa, R. *et al.* Direct electric field imaging of graphene defects. *Nat. Commun.* **9**, 3878 (2018).
64. Fang, S. *et al.* Atomic electrostatic maps of 1D channels in 2D semiconductors using 4D scanning transmission electron microscopy. *Nat. Commun.* **10**, 1127 (2019).
65. Hachtel, J. A., Idrobo, J. C. & Chi, M. Sub-Ångstrom electric field measurements on a universal detector in a scanning transmission electron microscope. *Adv. Struct. Chem. Imaging* **4:10**, (2018).
66. Gao, W. *et al.* Real-space charge-density imaging with sub-ångström resolution by four-dimensional electron microscopy. *Nature* **575**, 480–484 (2019).
67. Eldred, T. B., Smith, J. G. & Gao, W. Sub-Unit Cell Spatial Resolution of Phase and Polarization Mapping in Scanning Electron Diffraction. 1–6 (2021).
68. Cretu, O., Ishizuka, A., Yanagisawa, K., Ishizuka, K. & Kimoto, K. Atomic-Scale Electrical Field Mapping of Hexagonal Boron Nitride Defects. *ACS Nano* **15**, 5316–5321 (2021).
69. Hoppe, W. Beugung im inhomogenen Primärstrahlwellenfeld. I. Prinzip einer

Phasenmessung von Elektronenbeugungsinterferenzen. *Acta Crystallogr. Sect. A* **25**, 495–501 (1969).
70. Hoppe, W. & Strube, G. Beugung in inhomogenen Primärstrahlenwellenfeld. II. Lichtoptische Analogieversuche zur Phasenmessung von Gitterinterferenzen. *Acta Crystallogr. Sect. A* **25**, 502–507 (1969).
71. Hoppe, W. Beugung im inhomogenen Primärstrahlwellenfeld. III. Amplituden- und Phasenbestimmung bei unperiodischen Objekten. *Acta Crystallogr. Sect. A* **25**, 508–514 (1969).
72. Nellist, P. D., McCallum, B. C. & Rodenburg, J. M. Resolution beyond the 'information limit' in transmission electron microscopy. *Nature* **374**, 630–632 (1995).
73. Yang, H. *et al.* Simultaneous atomic-resolution electron ptychography and Z-contrast imaging of light and heavy elements in complex nanostructures. *Nat. Commun.* **7**, 1–8 (2016).
74. Maiden, A. M. & Rodenburg, J. M. An improved ptychographical phase retrieval algorithm for diffractive imaging. *Ultramicroscopy* **109**, 1256–1262 (2009).
75. Maiden, A., Johnson, D. & Li, P. Further improvements to the ptychographical iterative engine. *Optica* **4**, 736 (2017).
76. Humphry, M. J., Kraus, B., Hurst, A. C., Maiden, A. M. & Rodenburg, J. M. Ptychographic electron microscopy using high-angle dark-field scattering for sub-nanometre resolution imaging. *Nat. Commun.* **3**, 1–7 (2012).
77. Jiang, Y. *et al.* Electron ptychography of 2D materials to deep sub-ångström resolution. *Nature* **559**, 343–349 (2018).
78. Lazić, I., Bosch, E. G. T. & Lazar, S. Phase contrast STEM for thin samples: Integrated differential phase contrast. *Ultramicroscopy* **160**, 265–280 (2016).
79. Yücelen, E., Lazić, I. & Bosch, E. G. T. Phase contrast scanning transmission electron microscopy imaging of light and heavy atoms at the limit of contrast and resolution. *Sci. Rep.* **8**, 2676 (2018).
80. Krajnak, M., McGrouther, D., Maneuski, D., O'Shea, V. & McVitie, S. Pixelated detectors and improved efficiency for magnetic imaging in STEM differential phase contrast. *Ultramicroscopy* **165**, 42–50 (2016).
81. Tate, M. W. *et al.* Pub High Dynamic Range Pixel Array Detector for Scanning Transmission Electron Microscopy. *Microsc. Microanal.* **22**, 237–249 (2016).
82. Jones, L. Quantitative ADF STEM: Acquisition, analysis and interpretation. *IOP Conf. Ser. Mater. Sci. Eng.* **109**, (2016).
83. Yang, H. *et al.* Electron ptychographic phase imaging of light elements in crystalline materials using Wigner distribution deconvolution. *Ultramicroscopy* **180**, 173–179 (2017).
84. Ophus, C. *et al.* Efficient linear phase contrast in scanning transmission electron microscopy with matched illumination and detector interferometry. *Nat. Commun.* **7:10719**, 1–7 (2016).

85. Wei, X., Wang, M. S., Bando, Y. & Golberg, D. Electron-beam-induced substitutional carbon doping of boron nitride nanosheets, nanoribbons, and nanotubes. *ACS Nano* **5**, 2916–2922 (2011).
86. Egerton, R. F. Mechanisms of radiation damage in beam-sensitive specimens, for TEM accelerating voltages between 10 and 300 kV. *Microsc. Res. Tech.* **75**, 1550–1556 (2012).
87. Egerton, R. F. Control of radiation damage in the TEM. *Ultramicroscopy* **127**, 100–108 (2013).
88. Egerton, R. F., Li, P. & Malac, M. Radiation damage in the TEM and SEM. *Micron* **35**, 399–409 (2004).
89. Novoselov, K. S. Imaging of Bernal stacked and misoriented graphene and boron nitride : experiment and simulation. **244**, 152–158 (2011).
90. Algara-Siller, G., Kurasch, S., Sedighi, M., Lehtinen, O. & Kaiser, U. The pristine atomic structure of MoS2 monolayer protected from electron radiation damage by graphene. *Appl. Phys. Lett.* **103**, (2013).
91. Zan, R. *et al.* Control of radiation damage in MoS2 by graphene encapsulation. *ACS Nano* **7**, 10167–10174 (2013).
92. Lehnert, T., Lehtinen, O., Algara-Siller, G. & Kaiser, U. Electron radiation damage mechanisms in 2D MoSe2. *Appl. Phys. Lett.* **110**, (2017).
93. Lin, Y. C. *et al.* Three-fold rotational defects in two-dimensional transition metal dichalcogenides. *Nat. Commun.* **6**, 1–6 (2015).
94. Guguchia, Z. *et al.* Magnetism in Semiconducting Molybdenum Dichalcogenides. *Sci. Adv.* **4:eaat3672**, (2018).
95. Sun, L., Banhart, F. & Warner, J. Two-dimensional materials under electron irradiation. *MRS Bull.* **40**, 29–37 (2015).
96. Wang, S. *et al.* Atomic structure and formation mechanism of sub-nanometer pores in 2D monolayer MoS 2. *Nanoscale* **9**, 6417–6426 (2017).
97. Komsa, H. P., Kurasch, S., Lehtinen, O., Kaiser, U. & Krasheninnikov, A. V. From point to extended defects in two-dimensional MoS2: Evolution of atomic structure under electron irradiation. *Phys. Rev. B - Condens. Matter Mater. Phys.* **88**, 1–8 (2013).
98. Garcia, A. *et al.* Analysis of electron beam damage of exfoliated MoS2 sheets and quantitative HAADF-STEM imaging. *Ultramicroscopy* **146**, 33–38 (2014).
99. Wang, S., Robertson, A. & Warner, J. H. Atomic structure of defects and dopants in 2D layered transition metal dichalcogenides. *Chem. Soc. Rev.* **47**, 6764–6794 (2018).
100. Wang, S., Lee, G. Do, Lee, S., Yoon, E. & Warner, J. H. Detailed Atomic Reconstruction of Extended Line Defects in Monolayer MoS2. *ACS Nano* **10**, 5419–5430 (2016).
101. Kim, Y., Ihm, J., Yoon, E. & Lee, G. Do. Dynamics and stability of divacancy defects in graphene. *Phys. Rev. B - Condens. Matter Mater. Phys.* **84**, 75445 (2011).

102. Zhou, W. *et al.* Intrinsic structural defects in monolayer molybdenum disulfide. *Nano Lett.* **13**, 2615–2622 (2013).
103. Surwade, S. P. *et al.* Water desalination using nanoporous single-layer graphene. *Nat. Nanotechnol.* **10**, 459–464 (2015).
104. Heiranian, M., Farimani, A. B. & Aluru, N. R. Water desalination with a single-layer MoS 2 nanopore. *Nat. Commun.* **6:8616**, (2015).
105. O'Hern, S. C. *et al.* Selective ionic transport through tunable subnanometer pores in single-layer graphene membranes. *Nano Lett.* **14**, 1234–1241 (2014).
106. Schneider, G. F. *et al.* DNA translocation through graphene nanopores. *Nano Lett.* **10**, 3163–3167 (2010).
107. Farimani, A. B., Min, K. & Aluru, N. R. DNA base detection using a single-layer MoS2. *ACS Nano* **8**, 7914–7922 (2014).
108. Xiao, S. L., Yu, W. Z. & Gao, S. P. Simu Edge preference and band gap characters of MoS2and WS2nanoribbons. *Surf. Sci.* **653**, 107–112 (2016).
109. Chen, Q. *et al.* Atomically Flat Zigzag Edges in Monolayer MoS 2 by Thermal Annealing. *Nano Lett.* **17**, 5502−5507 (2017).
110. Lin, J. *et al.* Flexible metallic nanowires with self-adaptive contacts to semiconducting transition-metal dichalcogenide monolayers. *Nat. Nanotechnol.* **9**, 436–442 (2014).
111. Cai, J. *et al.* Atomically precise bottom-up fabrication of graphene nanoribbons. *Nature* **466**, 470–473 (2010).
112. Cheng, F. *et al.* Controlled Growth of 1D $MoSe_2$ Nanoribbons with Spatially Modulated Edge States. *Nano Lett.* **17**, 1116–1120 (2017).
113. Liu, X. *et al.* Top-down fabrication of sub-nanometre semiconducting nanoribbons derived from molybdenum disulfide sheets. *Nat. Commun.* **4:1776**, (2013).
114. Robertson, A. W. *et al.* Atomic Structure and Spectroscopy of Single Metal (Cr, V) Substitutional Dopants in Monolayer MoS2. *ACS Nano* **10**, 10227–10236 (2016).
115. Li, H. *et al.* Atomic Structure and Dynamics of Single Platinum Atom Interactions with Monolayer MoS2. *ACS Nano* **11**, 3392–3403 (2017).
116. Tan, C., Lai, Z. & Zhang, H. Ultrathin Two-Dimensional Multinary Layered Metal Chalcogenide Nanomaterials. *Adv. Mater.* **29**, 1–25 (2017).
117. Sim, D. M. *et al.* Controlled Doping of Vacancy-Containing Few-Layer MoS2via Highly Stable Thiol-Based Molecular Chemisorption. *ACS Nano* **9**, 12115–12123 (2015).
118. Wang, S. *et al.* In Situ Atomic-Scale Studies of the Formation of Epitaxial Pt Nanocrystals on Monolayer Molybdenum Disulfide. *ACS Nano* **11**, 9057–9067 (2017).
119. Chen, Q. *et al*. Supplementary information of Atomically Flat Zigzag Edges in Monolayer MoS 2 by Thermal Annealing. *Nano Lett.* **2**, acs.nanolett.7b02192 (2017).
120. Brown, A. & Rundqvist, S. Refinement of the crystal structure of black

phosphorus. *Acta Crystallogr.* **19**, 684–685 (1965).
121. Cartz, L., Srinivasa, S. R., Riedner, R. J., Jorgensen, J. D. & Worlton, T. G. Effect of pressure on bonding in black phosphorus. *J. Chem. Phys.* **71**, 1718–1721 (1979).
122. Zhao, J. *et al.* Rise of silicene: A competitive 2D material. *Prog. Mater. Sci.* **83**, 24–151 (2016).
123. Zheng, Y., Liu, J., Liang, J., Jaroniec, M. & Qiao, S. Z. Graphitic carbon nitride materials: Controllable synthesis and applications in fuel cells and photocatalysis. *Energy Environ. Sci.* **5**, 6717–6731 (2012).
124. Naguib, M., Mochalin, V. N., Barsoum, M. W. & Gogotsi, Y. 25th anniversary article: MXenes: A new family of two-dimensional materials. *Adv. Mater.* **26**, 992–1005 (2014).
125. Gouskov, A., Camassel, J. & Gouskov, L. Growth and characterization of III–VI layered crystals like GaSe, GaTe, InSe, GaSe1-xTex and GaxIn1-xSe. *Prog. Cryst. Growth Cheract.* **5**, 323–413 (1982).
126. Wells, A. F. *Structural Inorganic Chemistry*. (OUP Oxford, 2012).
127. Wainwright, J. E. & Starkey, J. A refinement of the structure of anorthite. *Zeitschrift fur Krist. - New Cryst. Struct.* **133**, 75–84 (1971).
128. Choi, W. *et al.* Recent development of two-dimensional transition metal dichalcogenides and their applications. *Mater. Today* **20**, 116–130 (2017).
129. Storm, A. J., Chen, J. H., Ling, X. S., Zandbergen, H. W. & Dekker, C. Fabrication of solid-state nanopores with single-nanometre precision. *Nat. Mater.* **2**, 537–540 (2003).
130. Xu, Q. *et al.* Controllable atomic scale patterning of freestanding monolayer graphene at elevated temperature. *ACS Nano* **7**, 1566–1572 (2013).
131. Qi, Z. J. *et al.* Correlating atomic structure and transport in suspended graphene nanoribbons. *Nano Lett.* **14**, 4238–4244 (2014).

Chapter 3 Methodology

3.1 Introduction

This chapter will summarize the experimental techniques used in this project, starting with the synthesis of 2D materials using CVD, transferring, annealing, initial characterization, and characterization with aberration-corrected STEM and its variant 4D-STEM. Details on data processing and simulations will also be outlined in the final section and will be further discussed in the following chapters.

3.2 Chemical Vapour Deposition Synthesis

3.2.1 MoS_2

MoS_2 specimens used in this project were grown by two methods. The specimen used in chapter 4 is grown on a Si wafer, and the one in chapter 6 is grown on soda lime glass.

MoS_2 samples used in chapter 4 were grown by atmospheric pressure CVD using a double tube method previously reported.[1] A schematic diagram is shown in fig. 3.1. The substrate was a 2 cm × 2 cm SiO_2 (300 nm)/Si wafer (University Wafer), which was sonicated in acetone and then in isopropyl alcohol (IPA) for 15 minutes each. A 22 cm-diameter large quartz tube was used as the reaction chamber. Sulphur powder (300 mg, 99.5%, Sigma-Aldrich) was placed in the large outer tube and positioned in the centre of the first furnace. A smaller 12 cm-diameter quartz tube containing the MoO_3 powder (20 mg, 99.5%, Sigma-Aldrich) was placed inside the outer tube and positioned at the centre of the second furnace. The Si substrate was situated on an alumina crucible and positioned downstream of the precursors. The large outer tube

was sealed and mounted at the centre of two furnaces and flushed with 500 sccm Ar gas flow (BOC) for half an hour. The gas flow was measured by a mass flow controller (MFC). In the first furnace, the sulphur powder was heated to 180°C in the large outer tube, forming gaseous sulphur and filling the whole tube with 150 sccm Ar flow. Meanwhile, the second furnace was heated to 200°C to prevent S deposition on the substrate. Next, MoO3 power in the small inner tube was heated by the second furnace to 800°C and reacted with the S atmosphere. The MoS_2 was grown on the Si wafer downstream from the chemicals with 10 sccm Ar flow for 20 minutes, after which the tube was removed from the furnace for fast cooling. The samples were spin-coated with PMMA (8% weight in anisole, 495A molecular weight) and preserved in a sample box wrapped with foil to prevent degradation and contamination.

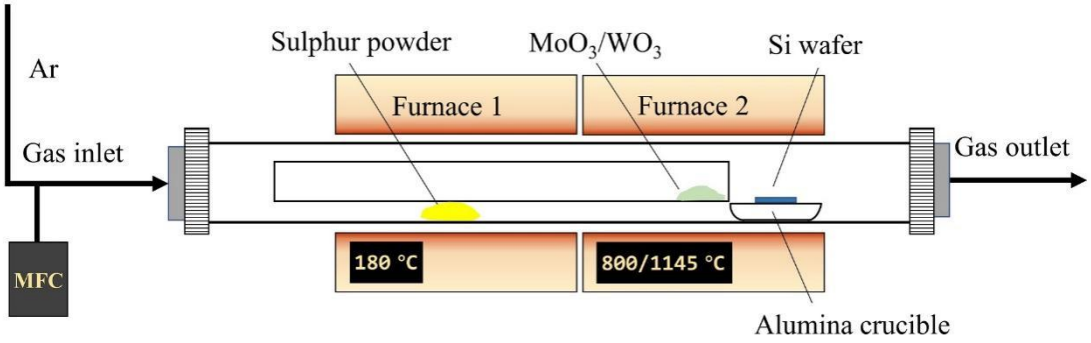


Figure 3.1. Schematic diagram of APCVD setup for MoS_2 and WS_2 synthesis using Si substrate. The temperature shown on the furnaces corresponds to the growth period.

MoS_2 sample used in chapter 6 was kindly provided by my colleague Mr. Yang Lu from Nanostructured Materials Group, Department of Materials, University of Oxford. It was synthesized via direct sulphurization of MoO_3 on glass using a double tube method.[2] The soda lime glass substrate was first cleaned in deionised water, acetone, and isopropanol. MoO_3 powder precursor (20 mg, 99.5%, Sigma-Aldrich) dissolved in 28.0% NH_4OH solution was spin-coated onto the glass substrate. The

substrate was then heated at 300 °C in the air to evaporate the residual water. For sulphurization, the sulphur powder (300 mg, 99.5%, Sigma-Aldrich) and the substrate were sealed in a quartz tube and flushed with 500 sccm Ar (BOC) for 30 minutes to purge and then 150 sccm for growth. The MoO_3/glass downstream was first heated to 800 °C, and the sulphur upstream was heated to 180 °C in a separate furnace followed by subsequent growth for 5 minutes. Finally, the tube was removed from the furnace for fast cooling, and the tube was flushed with 500 sccm Ar during the cooling. After cooling, the samples were spin-coated with PMMA to prevent degradation and contamination.

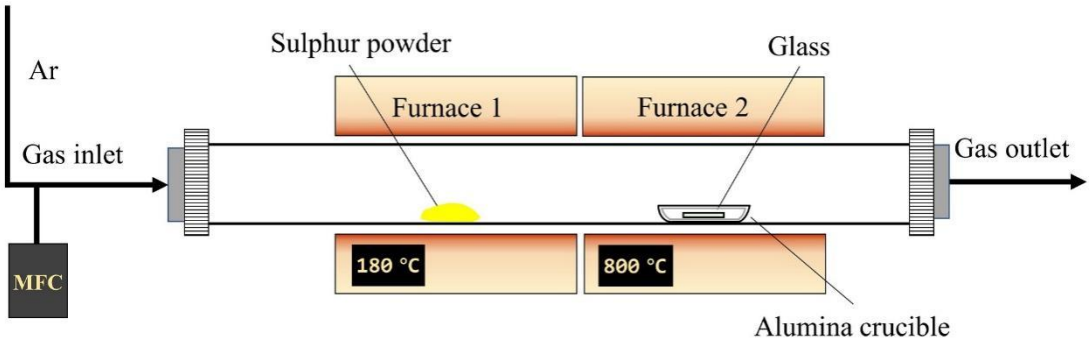


Figure 3.2. Schematic diagram of APCVD setup for MoS_2 synthesis using a glass substrate. The temperature shown on the furnaces corresponds to the growth period.

3.2.2 WS_2

WS_2 was grown by APCVD using a similar method as MoS_2, but with variations in temperature and gas flow.[3] 200 mg sulphur powder was placed in the large outer tube and positioned in the centre of the first furnace, and 100 mg WO_3 powder (99.5%, Sigma-Aldrich) was placed inside the smaller tube. The cleaned 2 cm × 2 cm substrate was situated on an alumina crucible and positioned downstream of the precursors. The large outer tube was sealed and mounted at the centre of two furnaces and flushed with 500 sccm Ar gas flow (BOC) for 30 minutes. In the first

furnace, the sulphur powder was heated to 180°C in the large outer tube, forming gaseous sulphur and filling the whole tube with 150 sccm Ar flow. The WO_3 power in the small inner tube was heated by the second furnace to 1145 °C and reacted with the S atmosphere, and once the temperature of the first furnace reached 100 °C, the Ar flow was reduced to 250 sccm. After 3 minutes of growth, the second furnace was set to room temperature and Ar flow was further reduced to 10 sccm. When the temperature of the second furnace dropped to 950 °C, the first furnace was set to 400 °C and the Ar flow to 500 sccm to remove the excess sulphur. When the second furnace reached 850 °C, the furnace was removed from the tube for fast cooling, and the tube was flushed with 500 sccm Ar during the cooling. After cooling, the samples were spin-coated with PMMA to preserve.

3.2.3 Graphene

Graphene was kindly provided by my colleague Ms. Linlin Hou from Nanostructured Materials Group, Department of Materials, University of Oxford. Graphene was grown by APCVD in a homemade furnace following the previously reported method.[4] A 10 cm × 10 cm Cu foil substrate (25 μm thick, 99.8%, Alfa Aesar) was polished, sonicated in diluted hydrochloric acid (HCl, 1 M) solution, deionised water, acetone, and IPA, and then placed on an alumina crucible situated at the centre of a tube furnace. The tube was sealed and flushed with a mixture of Ar (2000 sccm, BOC), H_2 (500 sccm, 25% H_2 in Ar, BOC), and methane (100 sccm, 1% CH_4 in Ar, BOC). The furnace temperature was then ramped up to 1060 °C and then annealed the Cu foil for 1 hour for Cu grain growth and surface cleaning with a flow of 500 sccm Ar and 100 sccm H_2. After annealing, the growth started with a flow of 600 sccm Ar, 100 sccm H_2, and 20 sccm CH_4, and continued for 1 hour. After growth, the sample was fast cooled by removing the furnace and the tube was flushed by 600 sccm Ar and 100 sccm H_2 during the cooling. After cooling, the samples were

spin-coated with PMMA.

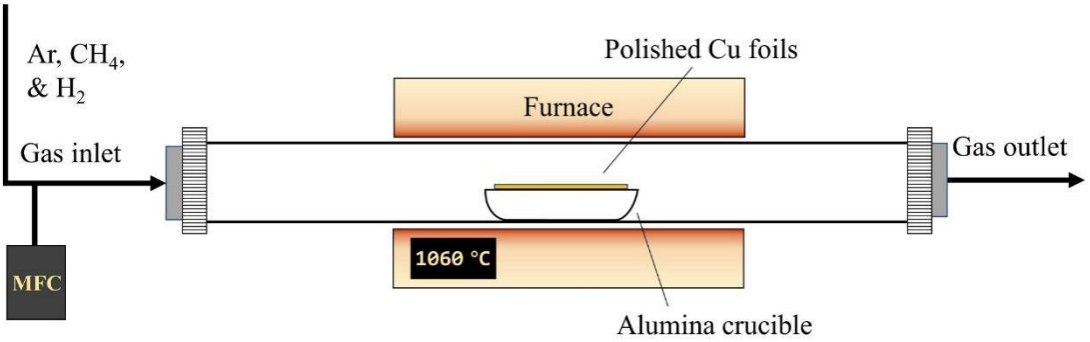


Figure 3.3. Schematic diagram of APCVD setup for graphene synthesis using Cu substrate. The temperature shown on the furnaces corresponds to the growth period.

3.3 Transfer and Cleanliness of 2D materials

After CVD synthesis, the materials were processed to detach from the substrate and transferred onto either lacey carbon grids or *in situ* heating chips (DENS Solutions) for subsequent AC-STEM analysis. The old version DENS-C-30 (fig. 3.4c) was used for data presented in chapter 4, and the new version Nano-Chips (fig. 3.4d) were used for data presented in chapter 5 and 6. I used a focused ion beam (JEOL JIB4700F) to drill viewing windows of 1 μm × 4 μm size on the Si_3N_4 membrane covering each slit.

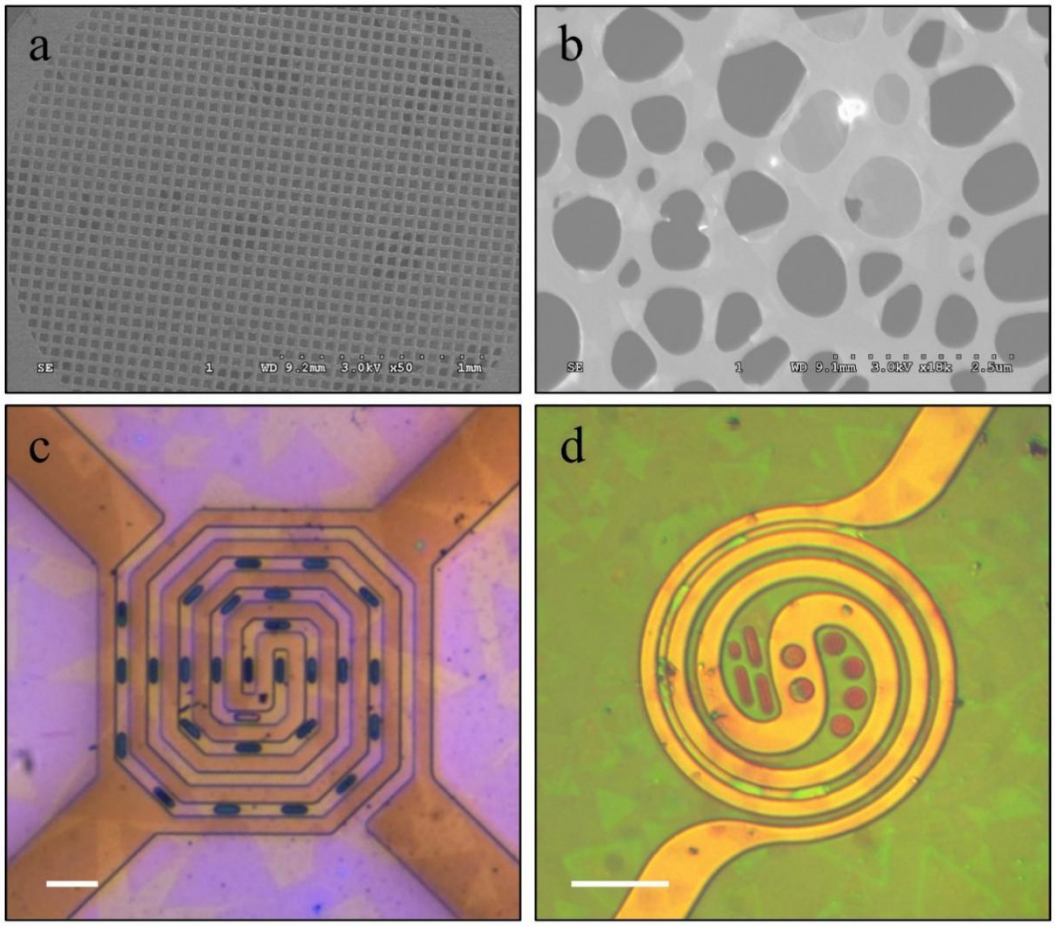


Figure 3.4. Various TEM grids were used in this project. (a-b) Scanning electron microscopy (SEM) secondary electron images of Lacey carbon grids under low and high magnification, respectively. (a) showed the Cu grids backbone and (b) shows the lacey carbon nets that suspend transferred 2D materials (bright contrast at top right). Comparison between two versions of heating chips: (c) DENS-C-30. (d) DENS Nano-Chips. The latter has fewer viewing windows but can heat with more precision and at higher temperatures (up to 1300 °C). Scale bars in (c) and (d) indicate 50 μm.

To transfer the MoS_2 and WS_2 grown on Si wafer to TEM grids, the materials and substrate were first spin-coated with PMMA (if not already present) and baked on a hotplate at 180 °C for 90 seconds. The PMMA around the substrate edges was removed by a file to expose the SiO_2 layer between the material and the Si substrate. The substrate was then floated in KOH solution to detach the materials from the

substrate by etching the SiO_2. The PMMA/MoS_2 (WS_2) film was then scooped out using a glass slide and placed onto the surface of deionised water for 30 minutes to remove any residual KOH. This step was repeated three times. Next, the film was scooped up by the TEM grids supported by a small piece of Si wafer (University Wafer) which were both gripped by reverse action tweezers. The film, TEM grids, and the Si wafer were dried in an ambient environment overnight. On the next day, the samples were first vacuum annealed at 180°C for one hour to enhance adhesion between the chip and the materials. The samples were then gripped by a reverse-action tweezer fastened to a retort stand and carefully immersed in a beaker of acetone for 24 hours and isopropanol for 10 minutes to dissolve all the PMMA. The acetone was replaced regularly to ensure efficient removal of PMMA.

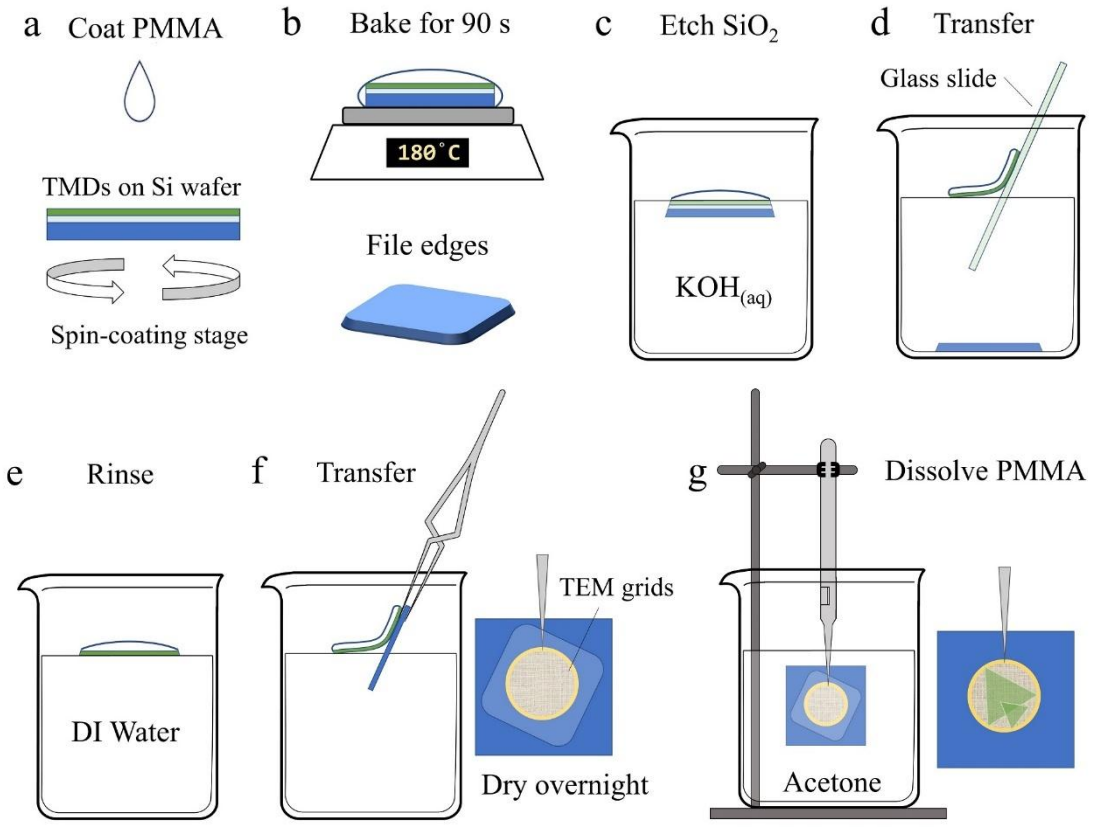


Figure 3.5. Schematic diagram of transferring MoS_2 and WS_2 grown on Si wafer to lacey

carbon grids.

To transfer the MoS_2 grown on the glass substrate to TEM grids, the MoS_2/glass was first spin-coated with PMMA (if not already present), baked on a hotplate at 150 °C for 5 minutes, and then slowly immersed in deionised water to detach the PMMA/MoS_2 thin film from the glass. The film was then scooped up by the TEM grids and the subsequent procedures were the same as MoS_2 grown on a Si wafer.

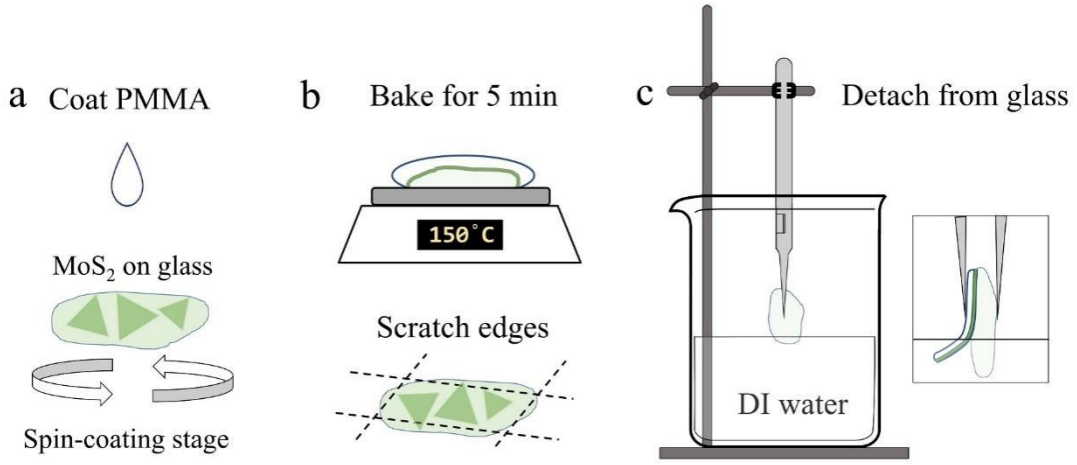


Figure 3.6. Schematic diagram of transferring MoS_2 grown on soda lime glass.

To transfer the graphene grown on Cu foil to TEM grids, the graphene/Cu was first spin-coated with PMMA (if not already present) and baked on a hotplate at 180 °C for 90 s. The PMMA/material/Cu was then floated on the surface of a beaker of ammonium persulfate solution (APS, 0.2 M, Sigma-Aldrich) to etch away the Cu substrate. The PMMA/graphene film was then scooped out using a glass slide and placed onto the surface of deionised water three times to remove any residual APS. The PMMA/graphene film was then scooped out by the TEM grids and the subsequent procedures were the same as MoS_2 grown on a Si wafer.

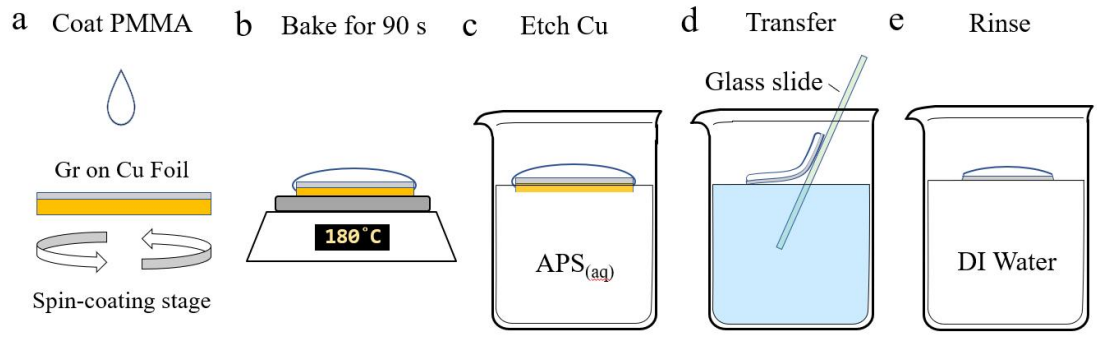


Figure 3.7. Schematic diagram of transferring graphene (Gr) grown on Cu foil.

To remove hydrocarbon contamination brought in during the transfer process, the samples were vacuum annealed in a homemade vacuum pump at 150 °C for 3 hours. Next, the samples were annealed using *in situ* heating holder (SH30-4M-FS, DENS Solutions) at 700 ~ 800 °C in the microscope with the beam blanked. During acquisition, the temperature stays at 700 °C to stop the accumulation of beam-induced carbon contamination.

3.4 Optical Microscopy and Scanning Electron Microscopy

Optical microscopy (OM) and scanning electron microscopy (SEM) were used to examine the size and distribution of the crystal domains in the CVD-synthesized 2D materials, and the result of the transfer process. The homemade optical microscope consists of a LED light source, objective lenses (×10 and ×50 magnification, Mitutoyo), and a CMOS colour sensor (Thorlabs). OM can visualize MoS_2 and WS_2 grown on Si wafer (fig. 3.8a, b), but not ideal for MoS_2 grown on glass, as well as graphene and hBN on Cu, which requires SEM for better contrast. SEM images were obtained on A Hitachi S-4300 field emission scanning electron microscope. The operation voltage used for imaging 2D materials was 3.0 kV, and the image was acquired with secondary electron (SE) mode, in which the image intensities were associated with the specimen topography (fig. 3.8c). Low magnification STEM was

frequently used to identify sample coverage and cleanliness of graphene (fig. 3.8d, e).

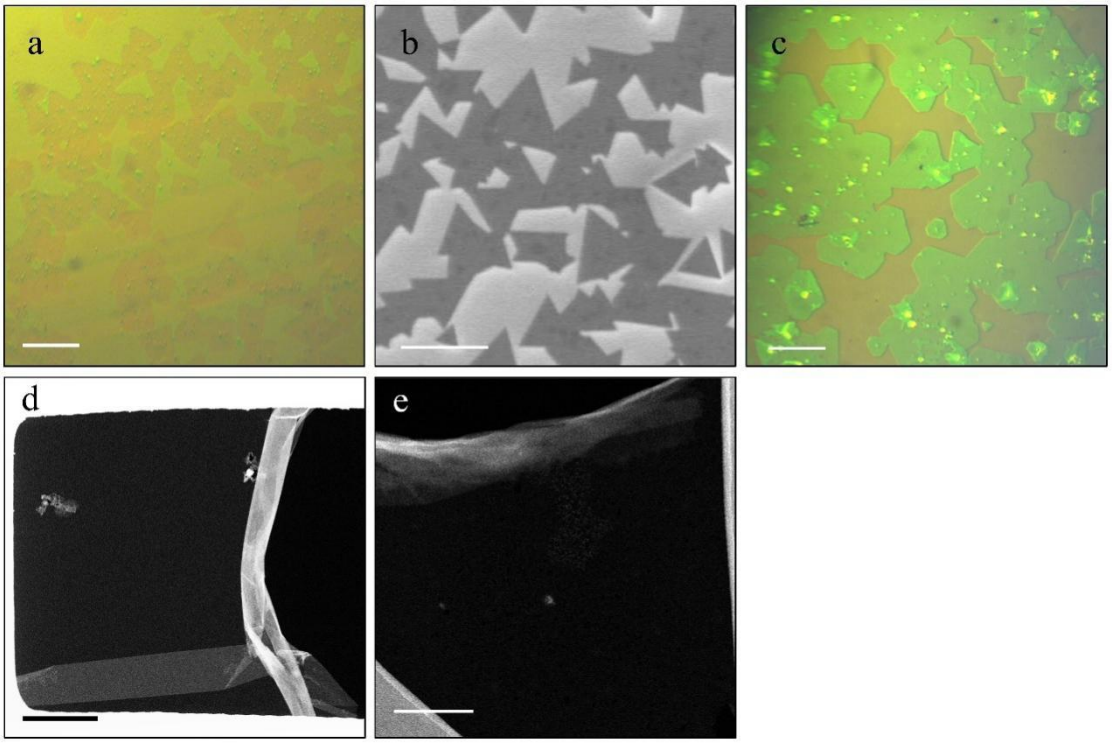


Figure 3.8. Initial characterization of synthesized 2D materials using optical microscopy (OM) and SEM. (a) OM image of MoS_2 grown on Si wafer. (b) SEM secondary electron (SE) image of MoS_2 grown on glass. (c) OM image of WS_2 grown on Si wafer. (d-e) low magnification STEM image of graphene on Cu foil. Scale bars in (a) and (c) indicate 50 μm, scale bar in (b) indicates 5 μm.

3.5 Scanning Transmission Electron Microscopy

3.5.1 Aberration-Corrected STEM

ADF-STEM images of MoS_2, WS_2, and graphene presented in chapter 4, 5, and 6 were captured with JEOL JEM-ARM300F at 60 kV at the electron Physical Sciences Imaging Centre (ePSIC) at Diamond Light Source, UK. ADF-STEM images in fig.

6.2 and fig. B7 were captured with JEOL JEM-ARM200F at 80 kV at David Cockayne Centre for Electron Microscopy, University of Oxford, UK. Both microscopes were equipped with a cold field emission gun and spherical aberration correction software and hardware. All 4D-STEM data were acquired on ARM300F with Merlin (MediPix) fast pixelated direct electron detector.

Before imaging, the microscopes were calibrated to correct objective and condenser lenses' aberrations. For ARM300F, the Ronchigram was calibrated on a thin amorphous region on the specimen or TEM grids. Under Ronchigram mode, the defocus was set to zero, and the sample height was set to infinite magnification. Coma, 2-fold, and 3-fold astigmatism were first adjusted manually on the camera. Then, a large condenser lens aperture (50 μm) was inserted to include the central flat region of the Ronchigram. Next, JEOL COSMO aberration correction was used to correct astigmatism (fig. 3.9). The correction started with a large defocus range of ±250 nm. The low order astigmatism including coma, 2-fold, and defocus were adjusted first, and once they reached a satisfying value, the high order aberrations including spherical, four-fold, and star aberration were adjusted (see table 3.1 for target values). After that, the defocus range was decreased to ±150 nm and the Ronchigram was corrected again. Continuing to decrease the defocus gradually to ±25 nm and the correction was finalized.

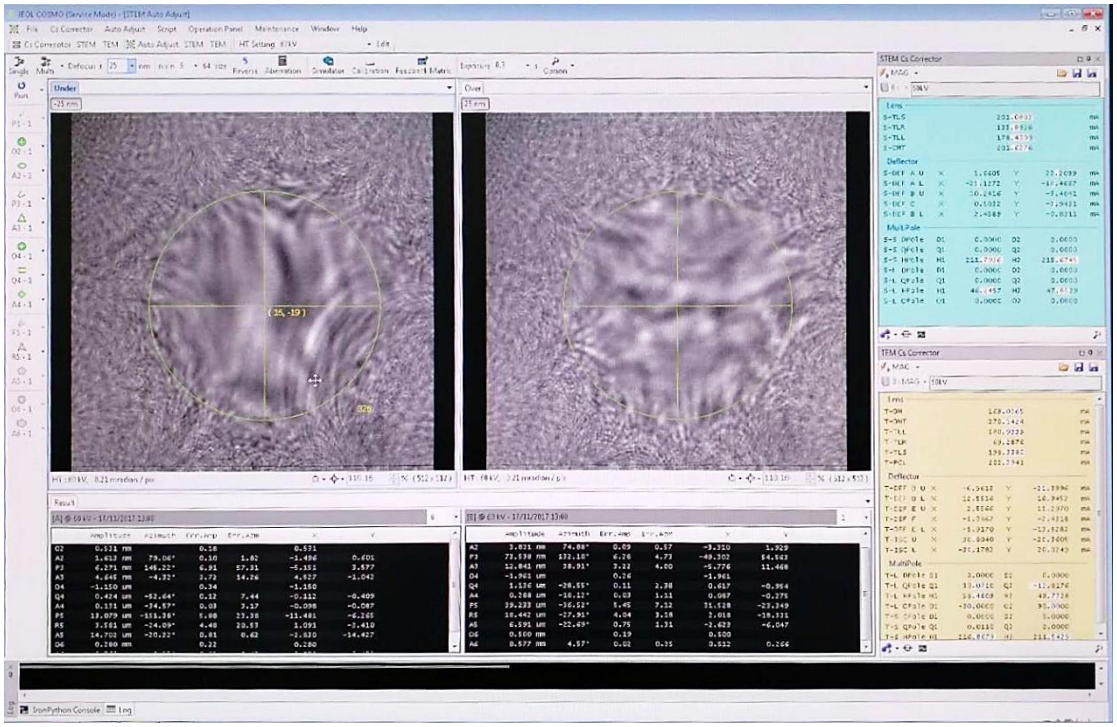


Figure 3.9. JEOL COSMO aberration correction software. The panel on the left (right) shows the under (over) focus Ronchigram. The yellow circle denotes the region that will be corrected by the software.

Table 3.1. Target values for aberration correction on ARM300F by manual adjustment and COSMO correction software.

Defocus (O2)	2-fold (A2)	Axial coma (P3)	3-fold (A3)
N/A	< 5 nm	< 50 nm	< 50 nm
Spherical (O4)	Star aberration (Q4)	4-fold (A4)	
< 2μm	< 2 μm	< 1 μm	

For ARM200F, the Ronchigram was calibrated on a standard gold nanoparticle sample. The Ronchigram was first adjusted manually on a phosphor screen. A large aperture was inserted, and magnification was set to 20M. Next, CEOS corrector was used to adjust the high order aberrations. Magnification was set to 600K, camera length to 8 cm, and a small aperture of 30 μm was inserted to select the central flat

region. The corrector user interface was given in fig. 3.10. In the right panel, a diffractogram of the gold specimen was captured and displayed at the centre, followed by a series of diffractograms from different beam tilt angles displayed around the centre, and those situated farther from the centre corresponded to larger tilt angle, and vice versa. The asymmetry of these diffractograms indicated the aberration presented, which could be corrected once selected. The low order astigmatisms should be corrected first to a satisfying value, and then proceed to the high order aberrations (see table 3.2 for target values). This procedure was repeated several times to achieve a larger aberration-free flat region in the calculated phase map shown in the left panel (quantified as size in mrad).

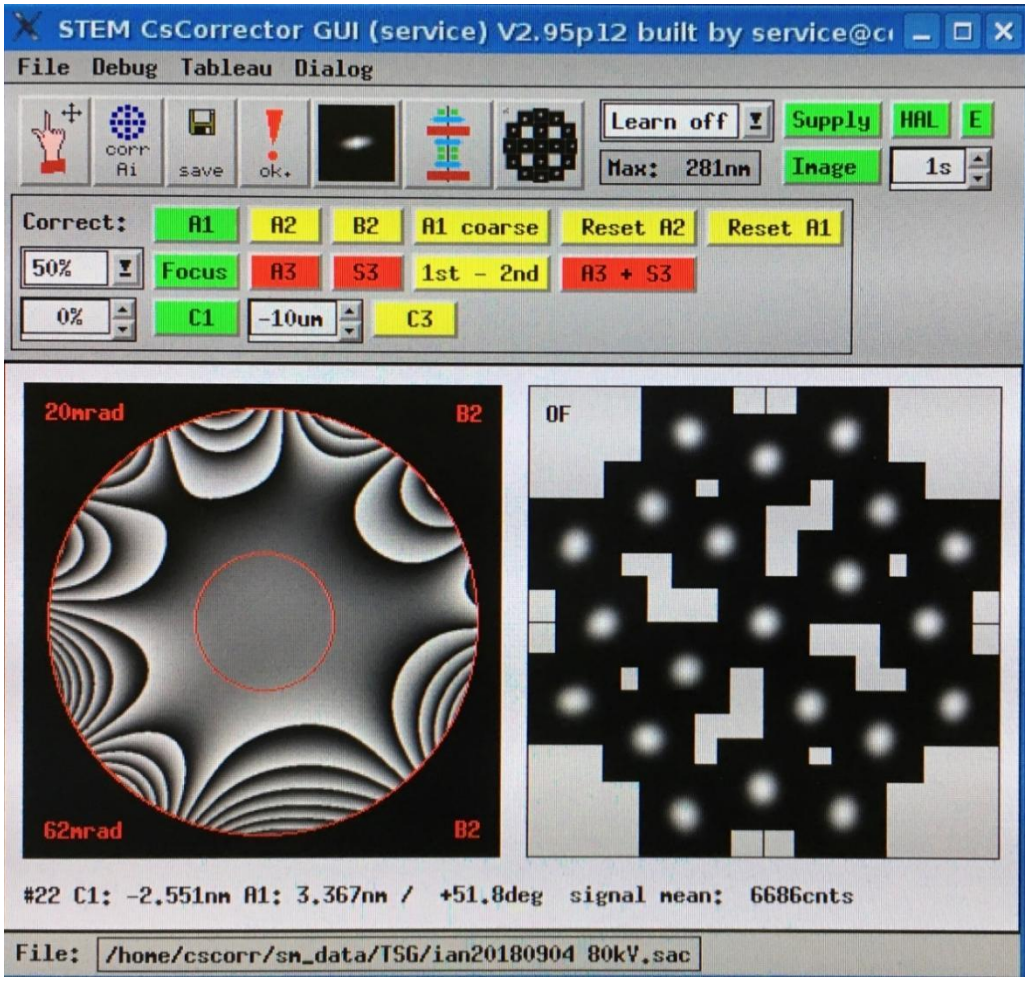


Figure 3.10. CEOS corrector software. The right panel is the Zemlin tableau of

diffractograms at different beam tilts. Note the diffractograms at large tilt angles were distorted due to aberration. The left panel is the phase map calculated from the measured aberration values, the top left value indicates the estimated size of the corrected region in mrad, and the top right indicates the major limiting aberration.

Table 3.2. Target values for aberration correction on ARM2200F by manual adjustment and CEOS correction software.

Defocus (C1)	2-fold (A1)	3-fold (A2)	Axial coma (B2)
< 1 nm	< 1 nm	< 100 nm	< 100 nm
4-fold (A3)	Star aberration (S3)	Spherical (C3)	
< 1 μm	< 1 μm	< 1μm	

The microscope parameters for imaging were adjusted based on the specimen and the condition of the microscope. For high resolution ADF-STEM images presented in chapter 5 and 6, the microscope parameters are summarized in the following tables. Electron dose was calculated based on eq. 2.21.

Table 3.3. High resolution ADF-STEM parameters for graphene in chapter 5 fig. 5.4

Accelerating voltage	Condenser lens aperture	Convergence semi-angle	
60 kV	30 μm	30.6 mrad	
Beam current	Camera length	ADF detector collection angle	
28.3 pA	15 cm	56.4 – 207.1 mrad	
Pixel count	Dwell time	Pixel size	Electron dose
1024 × 1024	100 μs	Fig. 5.4d ~ 0.44 Å	8.9×10^{4} $e^{-}/Å^{2}$
Pixel count	Dwell time	Pixel size	Electron dose
1024 × 1024	100 μs	Fig. 5.4e ~ 0.09 Å	2.1×10^{6} $e^{-}/Å^{2}$

Table 3.4. High resolution ADF-STEM parameters for MoS_2 in chapter 6 fig. 6.2

Accelerating voltage	Condenser lens aperture	Convergence semi-angle
80 kV	30 μm	24.8 mrad
Beam current	Camera length	ADF detector collection angle
28.3 pA	12 cm	68.3 to 206.4 mrad

Pixel count	Dwell time	Pixel size	Electron dose
2048 × 2048	5 μs	0.04 Å	4.3×10^5 $e^-/Å^2$

3.5.2 4D-STEM, Quantitative Conversion and Reconstruction

The 4D-STEM data were recorded using a JEM ARM300CF on a Merlin Medipix fast pixelated direct electron detector. Each data set contains 256 × 256 images of BFD and scattered electrons recorded by the pixelated detector at each probe position. The counting mode of the detector was 6-bit ($0 \leq$ intensity range $\leq 2^6$), and the dwell time was adjusted accordingly to avoid saturating the intensities but also allowed a large signal range in the BFD. ADF detector was inserted to capture a simultaneous ADF-STEM image with the same scan pixels and dwell time. Electron dose was calculated based on eq. 2.21.

Table 3.5. 4D-STEM parameters for MoS_2 in fig. 4.1

Accelerating voltage	Condenser lens aperture	Convergence semi-angle
60 kV	30 μm	30.6 mrad
Beam current	Camera length	ADF detector collection angle
28.3 pA	6 cm	111.3 to 222.7 mrad
ADF Pixel count	Dwell time	CBED pixel count
256 × 256	700 μs	515 × 515

Pixel size	Electron dose
0.26 Å	1.9×10^6 $e/Å^2$

Table 3.6. 4D-STEM parameters for WS_2 in fig. 4.2

Accelerating voltage	Condenser lens aperture	Convergence semi-angle
60 kV	30 µm	30.6 mrad
Beam current	Camera length	ADF detector collection angle
28.3 pA	8 cm	71.3 to 200.0 mrad
ADF Pixel count	Dwell time	CBED pixel count
256 × 256	500 µs	256 × 256
Pixel size	Electron dose	
0.20 Å	2.3×10^6 e/Å^2	

Table 3.7. 4D-STEM parameters for MoS_2 in fig. 4.5 and 4.6

Accelerating voltage	Condenser lens aperture	Convergence semi-angle	
60 kV	30 µm	30.6 mrad	
Beam current	Camera length	ADF detector collection angle	
28.3 pA	6 cm	111.3 to 222.7 mrad	
ADF Pixel count	Dwell time	CBED pixel count	
256 × 256	700 µs	515 × 515	
Pixel size	Electron dose	Pixel size	Electron dose
Fig. 4.5 ~ 0.30 Å	1.6×10^6 e/Å^2	Fig. 4.6 ~ 0.13Å	9.3×10^6 e/Å^2

Table 3.8. 4D-STEM parameters for MoS_2 in fig. 4.8 and 4.11

Accelerating voltage	Condenser lens aperture	Convergence semi-angle	
60 kV	30 µm	30.6 mrad	
Beam current	Camera length	ADF detector collection angle	
28.3 pA	6 cm	111.3 to 222.7 mrad	
ADF Pixel count	Dwell time	CBED pixel count	
256 × 256	1 ms	256 × 256	
Pixel size	Electron dose	Pixel size	Electron dose

Fig. 4.8 ~ 0.39 Å	1.2×10^6 e/Å^2	Fig. 4.11 ~ 0.31Å	1.8×10^6 e/Å^2

Table 3.9. 4D-STEM parameters for Graphene in chapter 5

Accelerating voltage	Condenser lens aperture	Convergence semi-angle
60 kV	30 µm	30.6 mrad
Beam current	Camera length	ADF detector collection angle
28.3 pA	15 cm	56.4 – 207.1 mrad
ADF Pixel count	Dwell time	CBED pixel count
256 × 256	700 µs	515 × 515

Pixel size	Electron dose	Pixel size	Electron dose
Fig. 5.2 ~ 0.26 Å	2.7×10^6 e/Å^2	Fig. 5.5 ~ 0.39 Å	1.1×10^6 e/Å^2

The quantitative conversion starts with the calculation of CoM shift of the BFD. The calculation was based on code written by Dr. Christopher Allen from ePSIC at Diamond Light Source, UK, and Dr. Colin Ophus from Molecular Foundry user facility at Lawrence Berkeley National Laboratory, US.

A frame of 4D-STEM data is a 2D image of the BFD and scattered electrons, which can be considered as a matrix M_{mn} of size $m \times n$ (m rows and n columns), with intensity I_{ij} at a coordinate (i, j).

$$M_{mn} = \begin{pmatrix} I_{11} & \cdots & I_{1n} \\ \vdots & I_{ij} & \vdots \\ I_{m1} & \cdots & I_{mn} \end{pmatrix}$$

And its CoM has two components, the horizontal CoM, CoM_x and the vertical CoM, CoM_y. They were calculated from

$$CoM_x = \frac{\sum (S_i \cdot d_i)}{\sum S_i} \ , \ CoM_y = \frac{\sum (S_j \cdot d_j)}{\sum S_j} (eq.\ 3.1)$$

Where $S_i = \sum I_i$, the sum of the intensity of the ith column, d_i is the horizontal

distance between this column and the central column; $S_j = \sum I_j$, the sum of the intensity of the jth row, d_j is the vertical distance between this row and the first row. Note that $\sum S_i = \sum S_j = \sum I_{ij}$, the sum of all the pixel intensity in M_{mn}.

A 4D-STEM data consists of a number of these 2D images which can be considered as another matrix of p rows and q columns, and the indices of each element correspond to the probe position during the scan. A sufficient number of CBED patterns of probe scanning in vacuum, usually 4000-5000 slices, were summed and calculated to find the CoM of the sum, which was set as the reference CoM. Next, a circular mask with a radius of the bright disk and origin at the reference CoM was applied to all the slices. Additional pixels were added to the radius of the mask to accommodate the small movement of BFD due to long range electric fields, poor parallelisation of the STEM scan, and poor diffraction focus. The CoM of the region inside the mask will be calculated for each slice in the 4D-STEM data. Then, the CoM shift of a random frame F at probe position (k, l) is given by

$$\boldsymbol{CoM_x}\,(\boldsymbol{F_{kl}}) = CoM_x(F_{kl}) - \overline{CoM_x(vac)}$$

$$\boldsymbol{CoM_y}\,(\boldsymbol{F_{kl}}) = CoM_y(F_{kl}) - \overline{CoM_y(vac)} \quad (eq.\ 3.2)$$

Note that $\boldsymbol{CoM_x}$ and $\boldsymbol{CoM_y}$ are vectors, which are expressed as a negative or positive value. They can be plotted as a 2D image, but only the magnitude will be shown. $\boldsymbol{CoM_x}$ and $\boldsymbol{CoM_y}$ can also be condensed into the radial CoM, $\boldsymbol{CoM_r}$, which is also a vector (sum of $\boldsymbol{CoM_x}$ and $\boldsymbol{CoM_y}$), and its magnitude is

$$CoM_r = \sqrt{(CoM_x)^2 + \left(CoM_y\right)^2} \quad (eq.\ 3.3)$$

A side note on the selection of BFD radius: selection of the central region of BFD produces a 'flat' CoM and phase map, where some phase modulations are suppressed, while the selection of the whole BFD preserves the high-frequency signals from the

defect structure, e.g., step edge, but also the high-frequency noise that also obscures the atomic resolution study. In this thesis, all CoMs were calculated using a large mask (as shown in fig. 3.11 top right), which includes the whole BFD. An extra 15 pixels was added to the mask radius to accommodate small movement of BFDs.

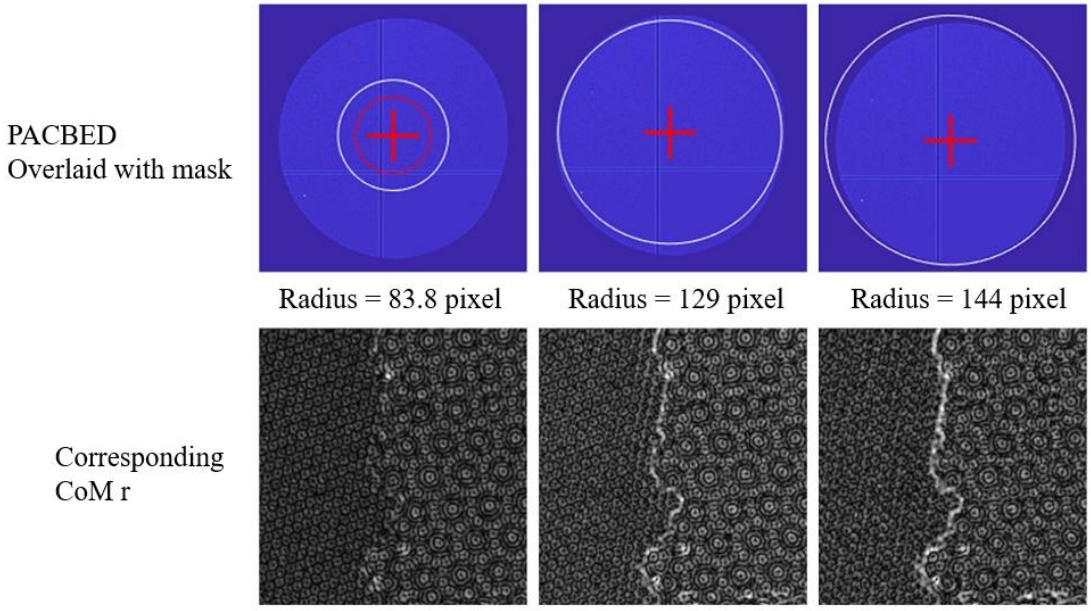


Figure 3.11. Comparison of the CoM maps of a graphene bilayer step edge calculated from a different section of the BFD. The circular mask is indicated by white ovals, the centre of the mask is indicated by the red cross, which is the CoM calculated from PACBED patterns. Top row: CBED patterns overlaid with a small, exact size, and slightly larger mask, respectively, indicating the area used for calculation of CoM. Bottom row: The corresponding CoMr maps show different features with different areas of selection.

Next, the CoM was converted to the lateral momentum component of the expectation value of momentum of the incident electrons by[5]

$$\langle \boldsymbol{p}_{\perp} \rangle = \frac{h}{\lambda} \cdot \sin\left(\boldsymbol{CoM_r}\right) \ (eq.\ 3.4)$$

Where h is Planck's constant, and λ is the electron wavelength. Ehrenfest's theorem extends classical physics derivative of momentum ($\frac{d\boldsymbol{p}}{dt} = -\boldsymbol{eE}$) into quantum mechanical context, thus gives

$$\boldsymbol{E}_{\perp \mathbf{pc}} = -\frac{v}{ez} \cdot \frac{h}{\lambda} \cdot \sin\left(\boldsymbol{CoM}_{\boldsymbol{r}}\right) \ (eq.\ 3.5)$$

Where $E_{\perp}$ is the probe-convolved projected electric field calculated from the lateral momentum, perpendicular to the incident probe direction, parallel to the specimen plane. $\boldsymbol{E}_{\perp \mathbf{pc}}$ is the convolution between the real projected electric field and the intensity of the incident probe I ($\boldsymbol{E}_{\perp \mathbf{pc}} = \boldsymbol{E}_{\perp} * \boldsymbol{I}_{\mathbf{p}}$). v is the velocity of an electron at a given electron microscope accelerating voltage, e is the elementary charge, z is the specimen thickness. The electric field referred to in this paper is the projected electric field integrated across the specimen thickness z ($\int E_{\perp} dz$), thus the values were presented in unit of V. Finally, based on Maxwell's equation, the total charge density ρ can be obtained by the divergence of $\boldsymbol{E}_{\perp \mathbf{pc}}$

$$div\left[\boldsymbol{E}_{\perp \mathbf{pc}}\right] = \frac{\partial \boldsymbol{E}_{\perp \boldsymbol{x}}}{\partial x} + \frac{\partial \boldsymbol{E}_{\perp \boldsymbol{y}}}{\partial y} = \frac{\rho_{PC}}{\varepsilon_0} \ (eq.\ 3.6)$$

where ε_0 is the vacuum permittivity. The step size of the divergence is between 1 to 3 pixels, depending on the magnification of the corresponding data set. Note that when referring to experimental charge density maps, it is always total charge density.

Summing mode reconstruction from 4D-STEM data replicates the function of a single-channel detector. The intensity of the reconstructed image would be the integrated intensities of the pixels inside a user-defined mask (virtual detector). For BF images, a circular mask with a radius of the BFD and origin at the reference CoM can be applied to the slices in the data set. ADF detector and ABF detector can also be simulated by using ring-shaped masks and changing the radius accordingly, which corresponds to the inner and outer angular range of the detector. For ADF-STEM images, the virtual detector range was selected to exclude the BFD region. For LAADF-STEM images, the detector range was close to the BFD, and for ABF images, the detector was just inside the periphery of the BFD. For DPC, the BFD was first divided into 4 quadrants, and the intensity difference between the left-side (1 and 3) and the right-side (2 and 4) quadrants was assigned to DPC_x, and the

difference between the upper (1 and 2) and lower sections (3 and 4) to DPC_y. The divergence of DPC is given by

$$div(\boldsymbol{DPC}) = \frac{\partial(\boldsymbol{DPC_x})}{\partial x} + \frac{\partial(\boldsymbol{DPC_y})}{\partial y} \quad (eq.\ 3.7)$$

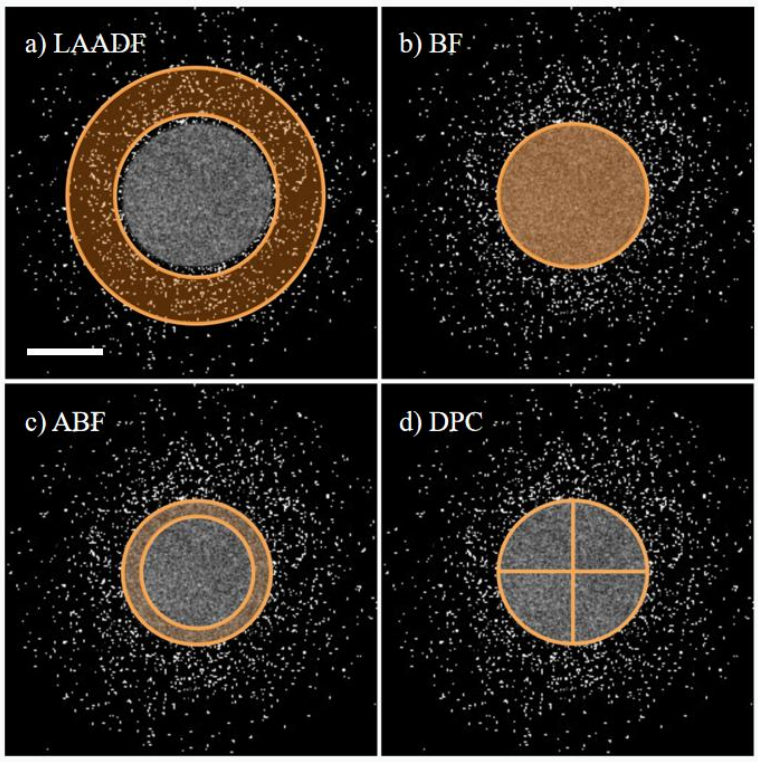


Figure 3.12. Reconstruction from 4D-STEM by using a virtual detector. (a) LAADF-STEM. (b) BF-STEM. (c) ABF-STEM (d) DPC. For (a-c), orange-shaded areas indicate the region selected. Scale bar in (a) indicates 40 mrad.

3.5.3 Image Analysis and Simulations

Most of the analyses in chapter 4-6 are on the atomic level, thus filtering and blurring were applied to raw data for better visualization of individual atoms. However, the measurement in fig. 4.6, A1, and A2 were obtained from unfiltered data. Both ImageJ and Matlab were used for image processing.

First, the ADF-STEM images were fast Fourier transformed and the reflections from {10-10} plane were used to calibrate the magnification of the images. For MoS_2 {10-10} plane, the lattice spacing is 0.273 nm, for WS_2 is 0.274 nm, for graphene is 0.213 nm. Next, the images were Gaussian-blurred with a standard deviation of 1-4 pixels, depending on the magnification. For better visualization, the images were resized (usually enlarged) using bicubic algorithm in ImageJ if necessary. The brightness and contrast were adjusted to show low-atomic-number atoms. An optional false colour was applied.

For 4D-STEM analysis, the CoM_x and CoM_y were filtered for better visualization as described below. Data presented in section 4.3 had stripe signals coming from the 50 Hz electrical hum (from nearby appliances powered by alternating current) and they were removed by masking the fast Fourier transform (FFT) of CoM_x and CoM_y (the bright horizontal line in fig. 3.13b, d were masked, while the signals from the lattice that positioned over this line were not masked). CoM_x and CoM_y were Gaussian blurred for better visualization using imgaussfilt function in Matlab. As shown in fig. 3.13i-l, applying a moderate Gaussian blur on CoM_x and CoM_y slightly decreased the magnitude of $\boldsymbol{CoM_r}$ and charge density, but did not significantly affect their shape. The standard deviation of Gaussian blur used for data presented in chapter 4 and 5 was 0.8 pixels, and for chapter 6 was 0.5 pixels. Quantitative measurements were performed on raw data without Gaussian blur. Sample drift was corrected by compression/expansion and shearing of the $\boldsymbol{CoM_r}$ matrix, if the drift is not caused by underlying lattice distortion.

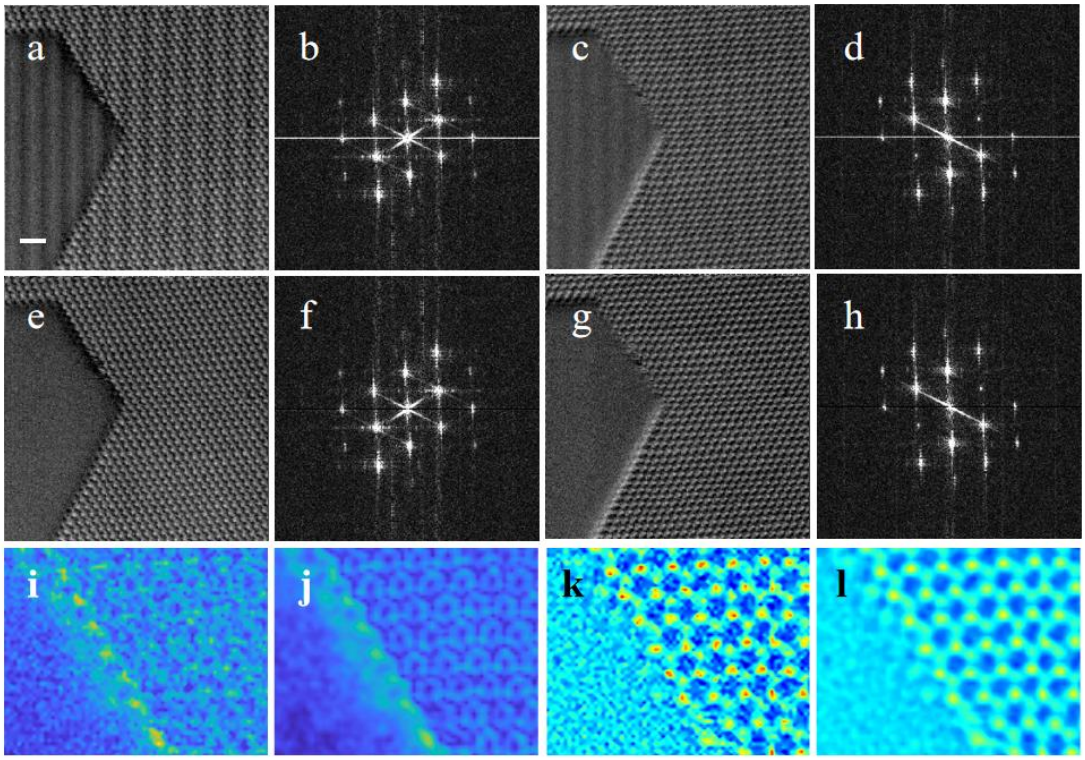


Figure 3.13. Using FFT to remove electrical noise. (a) CoM_x map of a monolayer MoS_2 lattice and its (b) FFT spectrum. (c) CoM_y map of the same data set and its (d) FFT spectrum. (e) CoM_x map after masking and its (f) FFT spectrum. (g) CoM_y map after masking and its (h) FFT spectrum. (i) raw CoM_r of a MoS_2 lattice edge. (j) same image as in (i) but with a gaussian blur on CoM_x and CoM_y. (k) charge density map corresponds to data in (i). (l) charge density map corresponds to data in (j). Scale bar in (a) indicates 1 nm.

The relative rotation between the STEM scan coils and the pixelated detector also needs to be corrected if present. The rotation angle θ was found by a self-consistency measurement written by my collaborator Dr. Colin Ophus (see appendix A). The rotation angle is consistent for datasets acquired in the same session. The rotated matrices $\boldsymbol{CoM_x(rot)}$ and $\boldsymbol{CoM_y(rot)}$ were multiplied by a rotating matrix, which gives the corrected $\boldsymbol{CoM_x}$ and $\boldsymbol{CoM_y}$

$$\begin{bmatrix} \boldsymbol{CoM_x} \\ \boldsymbol{CoM_y} \end{bmatrix} = \begin{bmatrix} cos\theta & -sin\theta \\ sin\theta & cos\theta \end{bmatrix} \begin{bmatrix} \boldsymbol{CoM_x(rot)} \\ \boldsymbol{CoM_y(rot)} \end{bmatrix} \quad (eq.\ 3.8)$$

For ADF-STEM images of multilayer graphene presented in chapter 5, inclusion and exclusion masks were applied to the corresponding FFT spectra to select or remove signals from certain layers, respectively.

3.5.4 ADF-STEM Image and CoM Simulation

Crystal models were constructed in CrystalMaker and adjusted in Discovery Studio for defects, dopants, and lattice reconstructions. Multislice simulations of phase and ADF-STEM images were performed using JEMS. Multislice simulations based on IAM used to simulate CBED patterns were performed using QSTEM code.[6,7] Angular dependent ADF-STEM simulations presented in chapter 6 were performed using Prismatic.[8] The microscope parameters used in simulation were based on the experimental conditions summarized in section 3.5.1.

3.5.5 Phase Reconstruction

Phase reconstructions were calculated by Dr. Colin Ophus via ePIE algorithm. The STEM probe intensities were used to update the object wave function in random order.[9] Because the electron probe had very low residual axial wave aberration coefficients, an idealized probe wave function was used for the reconstruction. The reconstruction space was padded to reduce boundary artefacts, and a fixed number of iterations were used. All relevant microscope parameters were taken from the experimental data. Phases presented in chapter 4 and 5 are obtained from Fourier integrated DPC/CoM.[10] The difference between the integrated phase and ePIE phase is marginal when only using the BFD.

3.5.6 Density Functional Theory Calculations

The DFT calculations for MoS_2 and WS_2 lattice and defect structures were carried out by my collaborator Dr. Shiang Fang originally at Harvard University, US.

The general method was to simulate the charge density distribution and the microscopic electric field by performing pseudo-potential DFT implemented in Vienna Ab initio Simulation Package (VASP)[11,12] for the electronic and mechanical properties. The computation employs projector augmented-wave (PAW) pseudo-potential formalism[13] with exchange-correlation functional parametrized by PBE,[14] which is a type of generalized gradient approximation (GGA) functionals. To simulate for the atomic defect structure, a supercell was used. The convergence was reached with a k grid sampling and a 450 eV energy cutoff for the plane-wave basis. The convergence DFT calculation yields the ground state charge distribution. With the electron and nuclear charge distribution, the microscopic electric field distribution was derived by solving the Poisson's equation for the electrostatics in the layered materials. The finite width of the probing electron beam was simulated by including appropriate Gaussian damping factor in the Fourier components. With these considerations, the solution for the electrostatic Poisson equation in the momentum space with the smearing factor can be written as

$$\widetilde{E}^{\sigma}(\vec{r}) = \sum_{\vec{G}_i \neq 0} \frac{-i\rho_{\vec{G}_i}\vec{G}_i}{\epsilon_0 |\vec{G}_i|^2} e^{i\vec{G}_i \cdot \vec{r} - |\vec{G}_i|^2/\sigma^2} \qquad \text{(eq. 3.9)}$$

over non-zero $\vec{G}_i$ momentum lattice vectors. For data presented in section 4.2, the full width half maximum (FWHM) of gaussian smearing was 1.2 Å. For data presented in section 4.3, the FWHM of gaussian smearing was 1.90 Å.

References

1. Wang, S., Wang, X., & Warner, J. H. All Chemical Vapor Deposition Growth of MoS_2 :h-BN Vertical van der Waals Heterostructures. *ACS Nano* **9**, 5246–5254 (2015).
2. Lu, Y. *et al.* Self-Limiting Growth of High-Quality 2D Monolayer MoS_2 by Direct Sulfurization Using Precursor-Soluble Substrates for Advanced Field-Effect Transistors and Photodetectors. *ACS Appl. Nano Mater.* **2**, 369–378 (2019).
3. Rong, Y. *et al.* Controlling sulphur precursor addition for large single crystal domains of WS $_2$. *Nanoscale* (2014). doi:10.1039/C4NR04091K
4. Sheng, Y., Rong, Y., He, Z., Fan, Y., & Warner, J. H. Uniformity of large-area bilayer graphene grown by chemical vapor deposition. *Nanotechnology* **26**, (2015).
5. Müller, K. *et al.* Atomic electric fields revealed by a quantum mechanical approach to electron picodiffraction. *Nat. Commun.* **5:5653**, (2014).
6. Koch, C. T. Determination of core structure periodicity and point defect density along dislocations. *ProQuest Diss. Theses* 214-214 (2002).
7. Goodman, P. & Moodie, A. F. Numerical evaluations of N-beam wave functions in electron scattering by the multi-slice method. *Acta Crystallogr. Sect. A* **30**, 280–290 (1974).
8. Ophus, C. A fast image simulation algorithm for scanning transmission electron microscopy. *Advanced Structural and Chemical Imaging* **13** (2017)
9. Humphry, M. J., Kraus, B., Hurst, A. C., Maiden, A. M., & Rodenburg, J. M. Ptychographic electron microscopy using high-angle dark-field scattering for sub-nanometre resolution imaging. *Nat. Commun.* **3**, 1–7 (2012).
10. Lazić, I., Bosch, E. G. T., & Lazar, S. Phase contrast STEM for thin samples: Integrated differential phase contrast. *Ultramicroscopy* **160**, 265–280 (2016).
11. Kresse, G. & Furthmüller, J. Efficient iterative schemes for ab initio total-energy calculations using a plane-wave basis set, *Phys. Rev. B*, **54**, 11169−11186 (1996).
12. Kresse, G. & Furthmüller, J. Efficiency of ab-initio total energy calculations for metals and semiconductors using a plane-wave basis set, *Comput. Mater. Sci.*, **6**, 15−50 (1996).
13. Blöchl, P. E. Projector augmented-wave method, *Phys. Rev. B*, **50**, 17953−17979 (1994)
14. Perdew, J.P., Burke, K., & Ernzerhof, M. Generalized Gradient Approximation Made Simple, *Phys. Rev. Lett.*, **77**, 3865−3868 (1996)

Chapter 4 MoS_2 and WS_2

4.1 Introduction

2D materials have been promising candidates for future ultrathin electronics since the isolation of graphene. However, their application requires a full understanding of their optical and electronic properties for both perfect crystals and defects. 4D-STEM can be used to imaging the atomic electric fields, charge density, and electrostatic potential, which is a unique perspective on how atomic defect structure and *in situ* manipulation (annealing, biasing, etc) can affect the real-time electronic environment in the materials. As demonstrated in section 2.3.4, 2D materials are inherently suitable for electric field imaging using 4D-STEM because of their thickness. Monolayer graphene and TMDs consist of a few elements, and from the <0001> direction the atoms are neatly arranged in a honeycomb lattice, making the analysis of atomic electric field self-explanatory and can be used as a guide when studying more complex structures and composites. In this chapter, I will present the electric field study of the perfect lattice and common defect structures of graphene, MoS_2, and WS_2 using the 4D-STEM technique.

4.2 MoS_2 and WS_2 Lattice and Simple Defects

Prior to analysis, it should be noted that the $|\boldsymbol{E}_{\perp \boldsymbol{PC}}|$ map discussed throughout this thesis is not equivalent to the actual projected atomic electric field, and 'charge density', which is the divergence of $|\boldsymbol{E}_{\perp \boldsymbol{PC}}|$, is also not the actual charge density. The influence from the convolution with probe must always be considered and evaluated by comparison with IAM simulation and DFT calculations.

Figure 4.1 shows a detailed analysis of monolayer MoS_2 based on the electric field

$|\boldsymbol{E}_{\perp \boldsymbol{PC}}|$, charged density, and phase from integrated $\boldsymbol{CoM}_{\boldsymbol{r}}$ (iCoM, as demonstrated in ref 1) reconstructed from a single 4D-STEM data set. Fig. 4.1a is the simultaneous Z-dependent ADF-STEM image which acts as an elemental map to pinpoint the Mo and 2S columns. This is helpful as the Mo and 2S columns become indistinguishable in $|\boldsymbol{E}_{\perp \boldsymbol{PC}}|$ and charge density map. After knowing the position of the atoms, interpretations of $|\boldsymbol{E}_{\perp \boldsymbol{PC}}|$ and $\boldsymbol{E}_{\perp \mathbf{pc}}$ components become more straightforward: fig. 4.1b and c show the electric field x and y component, respectively. The bright contrast $\boldsymbol{E}_{\perp \boldsymbol{PCx}}$ indicates the vector pointing at the x-axis propagating direction (to the right), while the bright contrast in $\boldsymbol{E}_{\perp \boldsymbol{PCy}}$ indicates vector pointing upwards following the y-axis direction. This shows that the electric field is emitting in a from the positively charged nuclei, and the screening effect from the electron cloud is not obvious due to the limited resolution. Note that at the exact position of the atom, the $|\boldsymbol{E}_{\perp \boldsymbol{PC}}|$ is minimal, as the projection of the electric field pointing outwards, perpendicular to the specimen plane, is zero. Fig. 4.1e shows the charge density map of the same region which is as predicted: the nuclei are positively charged, while the halfway in the Mo-S bonding, the charge density does not drop to negative due to the convolution of the positive charge. Only the centre of the hexagon shows the negative charge from the electron cloud. The $\boldsymbol{E}_{\perp \boldsymbol{PC}}$ vector map is a good indication of the electric field emitting from the atom position and can indicate whether there is relative rotation between the scan coil and the pixelated detector.

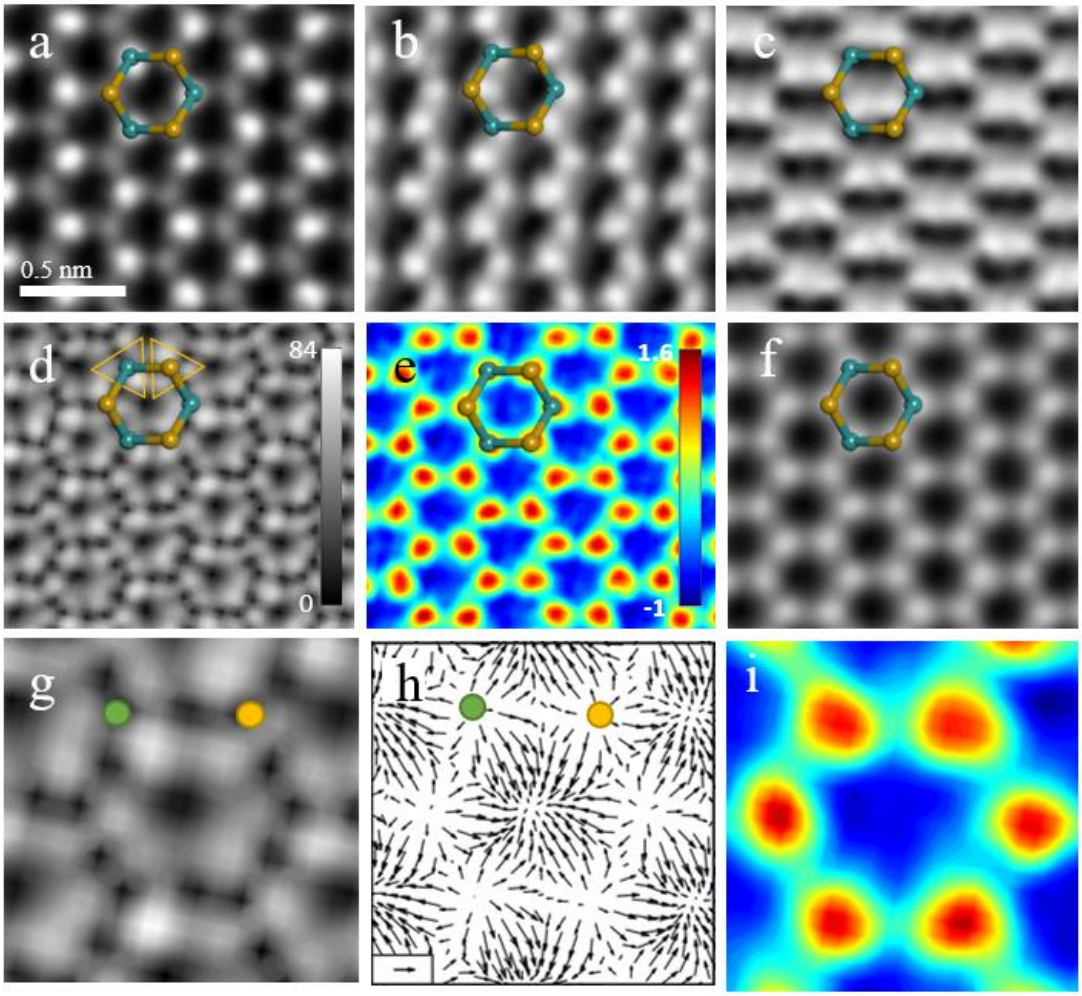


Figure 4.1. 4D-STEM analysis of MoS_2 lattice. (a) Simultaneous HAADF-STEM image. (b, c) Electric field x and y components, respectively. (d) electric field ($|\boldsymbol{E}_{\perp \boldsymbol{PC}}|$), calibration bar unit is V (e) charge density, calibration bar unit is $q \cdot A^{-2}$, and (f) phase (iCoM) of the same region, calculated from integration of radial CoM shift.[1] (g) magnified $|\boldsymbol{E}_{\perp \boldsymbol{PC}}|$, (h) $\boldsymbol{E}_{\perp \boldsymbol{PC}}$ vector map of the same region (scale bar corresponds to 50 V), and (i) charge density map. Scale bar in (a) applies to (b-f). Green ovals in the overlaid crystal model indicate Mo column and yellow ovals indicate 2S column.

It should be noted that the comparison between different quantitative measurements of electric field is hindered by several factors. Fig. 4.2 shows the $|\boldsymbol{E}_{\perp \boldsymbol{PC}}|$ map of MoS_2 lattice under different magnifications (i.e., electron dose), sample cleanliness,

aperture size, and aberration. High magnification, less surface contamination, and better resolution (larger convergence semi-angle and less aberration) will generate a higher $|\boldsymbol{E}_{\perp \boldsymbol{PC}}|$, as $\boldsymbol{E}_{\perp \boldsymbol{PC}}$ is the convolution between the true projected electric field and the intensity distribution of the probe, as described in section 2.3.4 and equation 2.15. This poses a question on how to effectively compare data acquired from different sessions, and even during the same session if the microscope is unstable. This may be one of the reasons why there is always a discrepancy between the simulation and experimental results, and even if the difference can be minimized by using the exact coherence and aberration conditions to simulate CBED patterns, the results may not be applicable to other experimental results. In this thesis, when discussing fluctuation of $|\boldsymbol{E}_{\perp \boldsymbol{PC}}|$ due to defective structures, the comparisons were always made between defects and perfect lattice in one set of data to accommodate the effect of possible changing imaging parameters. IAM simulations of CBED patterns were carried out using the same imaging parameters, and DFT calculations were convoluted with a Gaussian function to simulate the partial coherence from the electron probe.

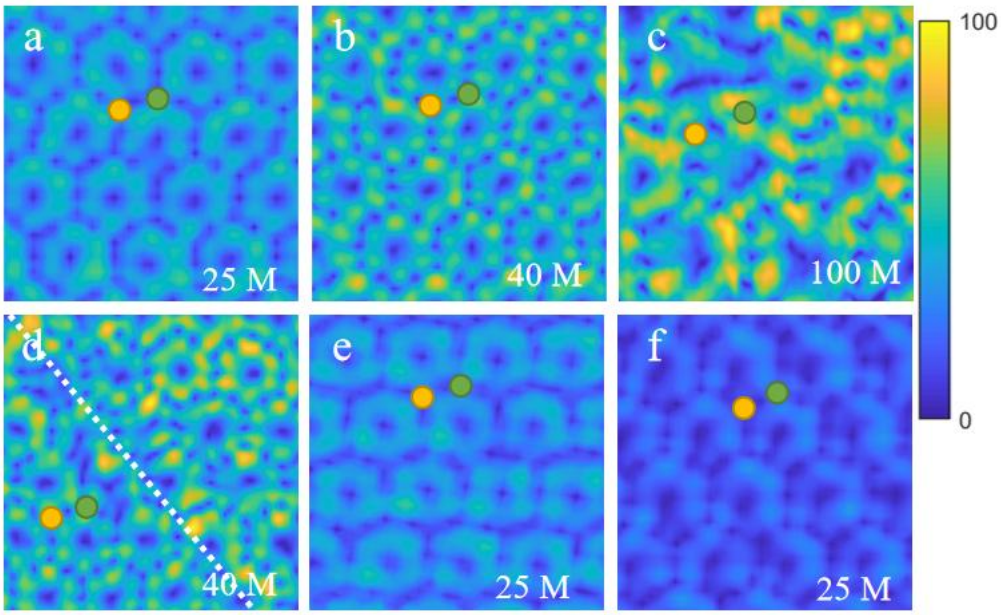


Figure 4.2. Quantitative measurement affected by the magnification, sample cleanliness, convergence semi-angle, and resolution. (a-f) $|\boldsymbol{E}_{\perp \boldsymbol{PC}}|$ map of monolayer MoS_2 from

4D-STEM data taken at magnification marked at bottom right. (a-d) used condenser lens aperture of 40 μm and (e-f) used condenser lens aperture of 30 μm. (d) Dotted line indicates clean region (bottom left) and carbon-contaminated region (top right). Green ovals indicate Mo column and yellow ovals indicate 2S column.

Fig. 4.3 shows the detailed analysis of WS_2, which shows similarity with MoS_2. The only difference is that W has a higher atomic number, thus exhibiting higher $|\boldsymbol{E}_{\perp \boldsymbol{PC}}|$ and charge density. In fig. 4.4, DFT calculation of MoS_2 and WS_2 $|\boldsymbol{E}_{\perp \boldsymbol{PC}}|$ shows a good approximation of the shape and asymmetry of the experimental atomic electric field, but there is a factor of ~2 between the $|\boldsymbol{E}_{\perp \boldsymbol{PC}}|$ values of DFT calculation and experimental results (detailed comparison shown in fig. B1), as reported by previous studies[2] and discussed in section 2.3.4. In section 4.3, the experimental results were multiplied by a scaling factor of 2 for comparison with DFT calculation. Exact simulation has been achieved by Oxley using a multislice simulation with quantum excitation of phonons considering the effect of spatial and temporal incoherence,[3] however, is beyond the scope of this thesis. Otherwise stated, all other data presented are raw data without scaling.

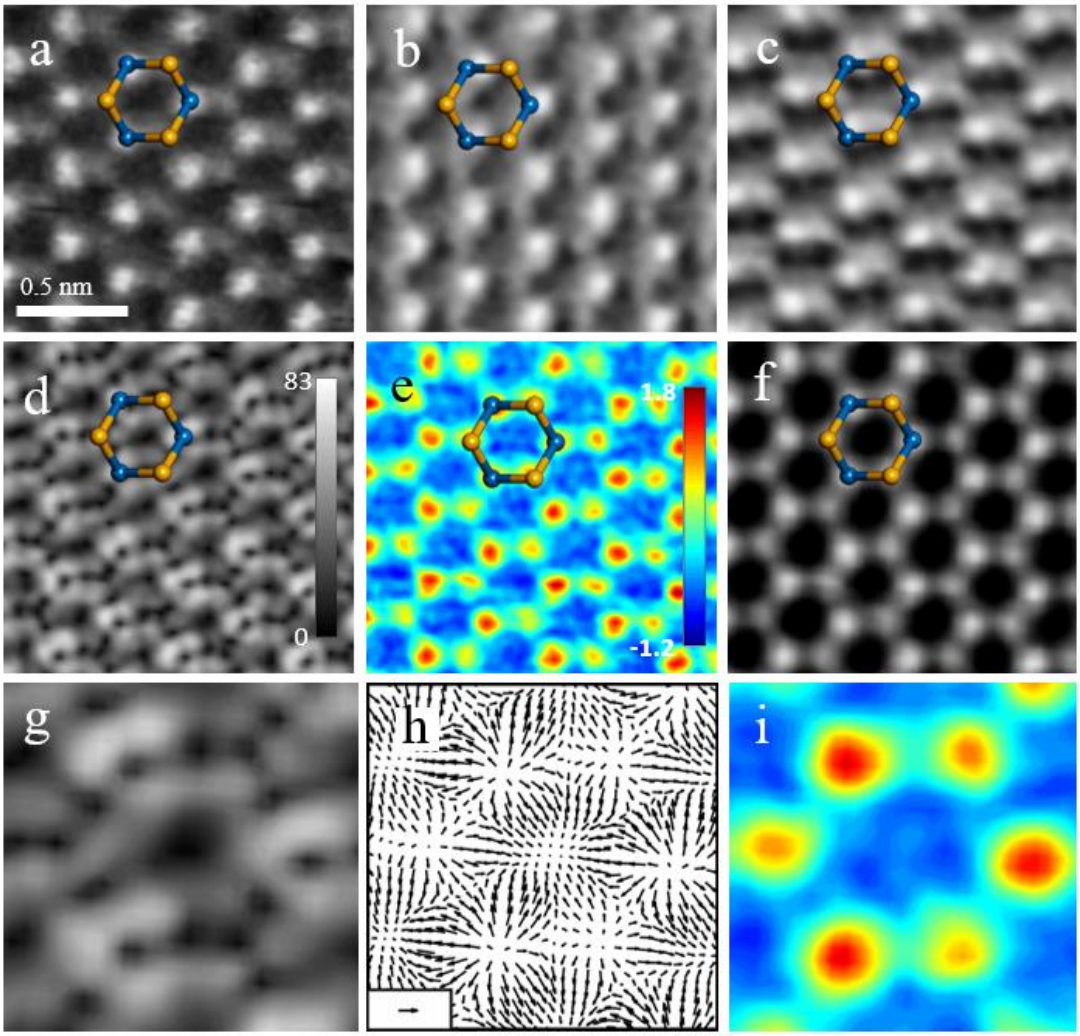


Figure 4.3. 4D-STEM analysis of WS_2 lattice. (a) Simultaneous HAADF-STEM image. (b, c) Electric field x and y components, respectively. (d) $|\boldsymbol{E}_{\perp \boldsymbol{PC}}|$, calibration bar unit is V (e) Charge density, calibration bar unit is $q \cdot A^{-2}$. (f) Phase calculated from iCoM. (g) Magnified $|\boldsymbol{E}_{\perp \boldsymbol{PC}}|$, (h) $\boldsymbol{E}_{\perp \boldsymbol{PC}}$ vector map (scale bar corresponds to 50 V), and (i) charge density map of the same region. Scale bar in (a) applies to (b-f). Blue ovals in the overlaid crystal model indicate W column and yellow ovals indicate 2S column.

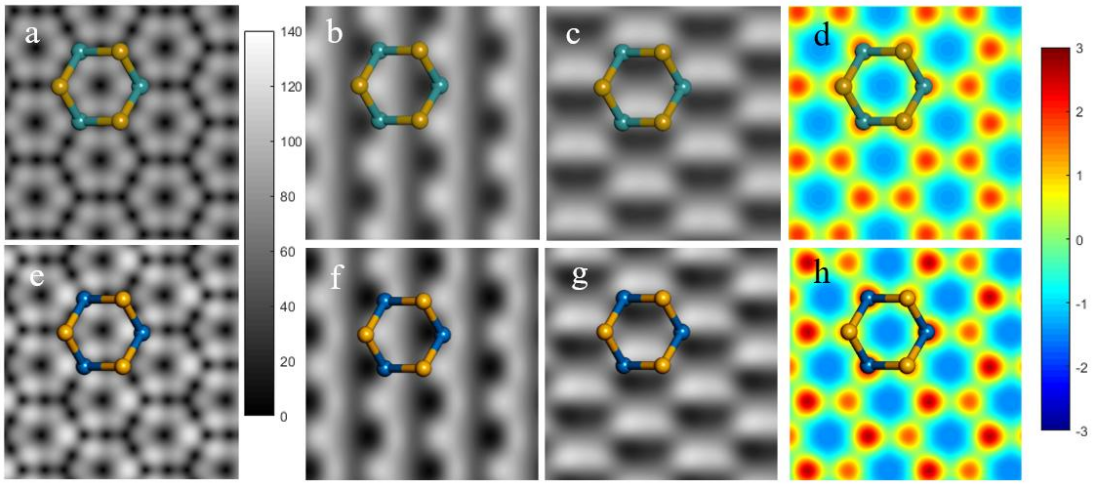


Figure 4.4. DFT calculation of (a, e) $|E_{\perp}|$, calibration bar unit is V, (b, f) CoM_x, (c, g) CoM_y, and (d, h) charge density, calibration bar unit is $q \cdot A^{-2}$. The top row shows results for MoS_2 and the bottom row for WS_2.

Based on the understanding of perfect lattices, 4D-STEM can be a powerful tool in analysing defective structures with atomic resolution. It should be noted that features arising from defective structures can either be a result of changes in electronic environment, or imaging artefact from partial coherence of electron probe. Thus, it is always necessary to include DFT calculation and IAM simulation to confirm the cause of abnormal features at defective structure. Fig. 4.5 shows the study of the simplest form of defects in MoS_2, point S vacancies. Fig. 4.5a shows the reconstructed LAADF-STEM image of V_S and V_{S2} in monolayer MoS_2. The V_{S2} can be effectively identified, but the V_S is better visualized in phase (fig. 4.5b) and $|\boldsymbol{E}_{\perp \boldsymbol{PC}}|$ map (fig. 4.5c). However, the charge density inside a V_{S2} showed a faint intensity similar to an atom (fig. 4.5d). The IAM simulation and DFT calculation of $|\boldsymbol{E}_{\perp \boldsymbol{PC}}|$ and charge density based on V_S models is in accordance with the experimental results, but neither simulation showed the same level of increased charge density inside the V_{S2}, as shown by the intensity line profiles in appendix (fig. B2a-l). It is mostly likely that a substitutional dopant, e.g., carbon, was situated at the V_{S2}, which contributes to the increased charge density. IAM simulation of $|\boldsymbol{E}_{\perp \boldsymbol{PC}}|$ and charge density based on such crystal model (fig. 4.5n) showed similar features as observed

in experimental results: the cavity of V_{S2} with C substitution in $|\boldsymbol{E}_{\perp \boldsymbol{PC}}|$ map was slightly larger than that of the simulated $|\boldsymbol{E}_{\perp \boldsymbol{PC}}|$ of V_{S2}, and the charge density map showed similar signal inside V_{S2}, and the increase in charge density is comparable to experimental results (fig. B2o). C substitution at V_{S2} was observed repetitively in my experiments (fig. B3). Previous studies on intrinsic C substitutional doping in MoS_2 has shown that C doping at S site is energetically favourable compared to Mo site,[4] however, it is unable to identify whether it is an intrinsic doping due to precursor impurity or an *in situ* defect evolution due to electron beam damage.

Since the V_{S2} and carbon-filled V_{S2} are identical in conventional ADF-STEM images, some observations of V_{S2} and calculations based on V_{S2} structures need to be re-evaluated. $|\boldsymbol{E}_{\perp \boldsymbol{PC}}|$ and charge density map are able to locate vacancies and differentiate V_{S2} and substitutional atoms, showing the efficiency of 4D-STEM in imaging low-atomic-number substitutional atoms, alongside the study of surface adsorption atoms in chapter 6. However, no evidence of charge redistribution was observed in V_S and carbon-filled V_{S2}, as the experimental results match well with the IAM simulation. For the unfilled V_{S2}, which I did not encounter during this project, it causes a much stronger lattice contraction compared to V_S,[5] and the exposed and undercoordinated Mo atoms can be used for surface adsorption in catalytic application.[6] The change in MoS_2's electronic properties due to V_{S2} is intriguing and whether 4D-STEM analysis is capable of imaging these changes requires further studies.

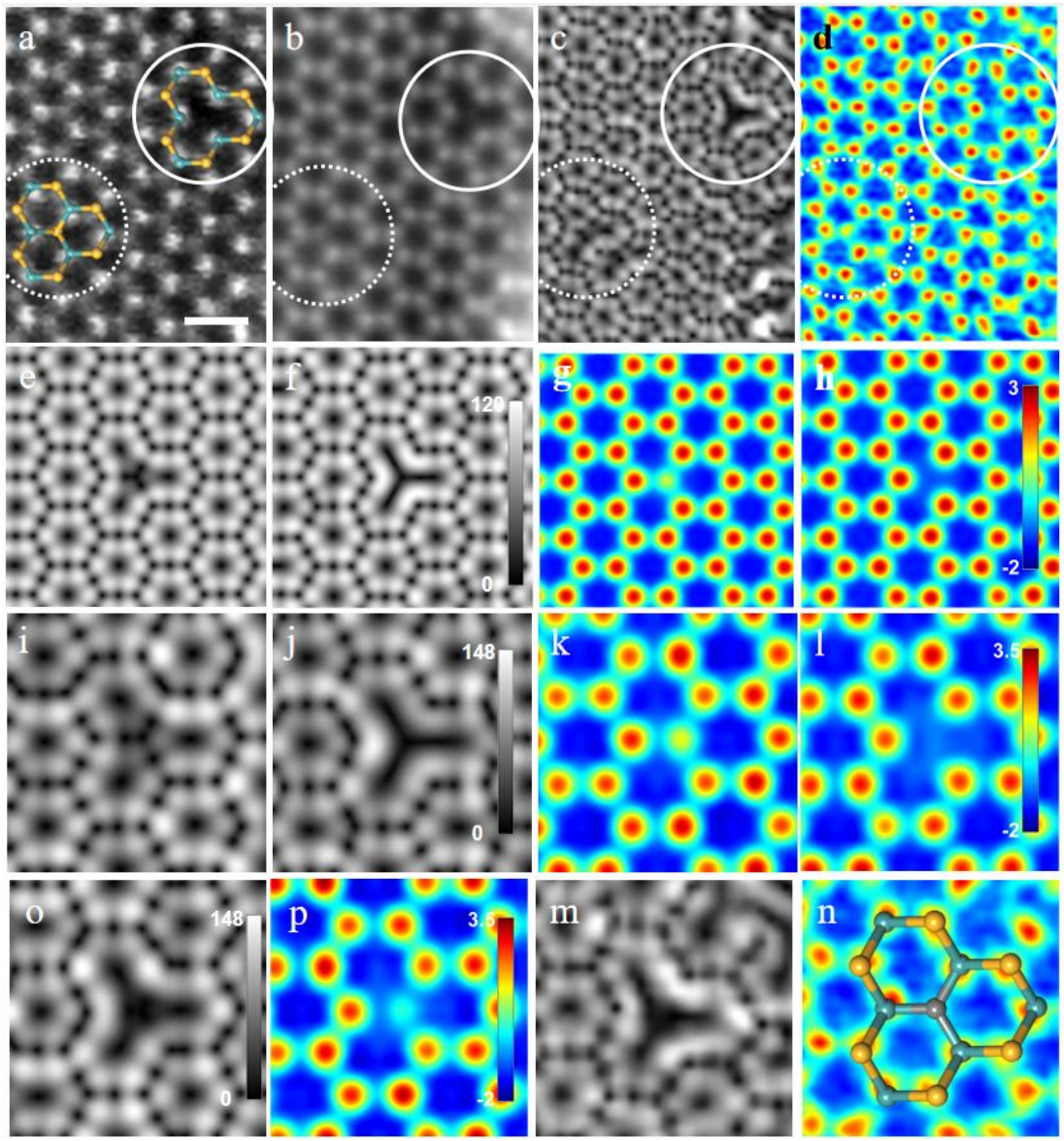


Figure 4.5. Analysis of V_S and V_{S2} in monolayer MoS_2. (a) LAADF-STEM image reconstructed from 60-200 mrad, (b) phase calculated from iCoM, (c) $|\boldsymbol{E}_{\perp \boldsymbol{PC}}|$, (d) charge density, V_S is indicated by dashed-line circle, V_{S2} is indicated by solid-line circle. Scale bar in panel a indicates 0.5 nm and applies to panel a-d. (e-f) DFT calculated $|\boldsymbol{E}_{\perp \boldsymbol{PC}}|$ and (g-h) charge density of V_S and V_{S2}, respectively. (i-j, o) Multislice simulation based on IAM showing $|\boldsymbol{E}_{\perp \boldsymbol{PC}}|$ and (k-l, p) charge density maps of V_S, V_{S2}, and V_{S2} with C substitution, respectively. (m, n) Enlarged $|\boldsymbol{E}_{\perp \boldsymbol{PC}}|$ and charge density map of V_{S2} region shown in panel c and d, panel n is superimposed by a crystal model of V_{S2} with C substitution. For $|\boldsymbol{E}_{\perp \boldsymbol{PC}}|$, calibration bar unit is V, for charge density maps, calibration bar

unit is $q \cdot A^{-2}$.

Upon continuous loss of S atoms, S vacancies migrate and line up to form line S vacancy (LV).[7] Identification of its atomic structure is challenging due to changed stoichiometry and shrunk lattice. It has been suggested by DFT calculations that at 3S-wide line vacancies, the band gap and the effective mass of electrons and holes were significantly reduced, forming a 1D conduction channel along the LV.[8] Thus in this section, the analysis of this structure was supplemented by DFT calculations and IAM simulations, which will be discussed in detail later.

In fig. 4.6, the ADF-STEM image shows an Mo-rich region along the LV, and the phase map provides a less Z-dependent image clearly showing the single S atoms, enabling the construction of an accurate crystal model. The total charge density map (fig. 4.6d) and the line profiles (fig. 4.6i & B4) show that the region between the LV has a lower charge density compared to the centre of the MoS_2 hexagon. This is explained by the DFT calculation, where the calculated total charge density also shows a decrease (fig. 4.6g), and the calculated electron density shows an increase along the LV compared to the centre of hexagon (fig. B4d, e), leading to a decrease in total charge density. Multislice simulation based on IAM was performed, and by comparing the line profiles across the line profile region in experimental results, DFT calculation, and IAM simulation (fig. 4.6i-k), it become obvious that the decrease in charge density was only observed in experimental results and DFT calculation, meaning that this phenomenon of electron-rich region may not be structural, and may be attributed to the formation of new bondings formed between Mo atoms.[8]

However, it should be noted that, the decrease in charge density observed in experimental results is in the noise level of the raw data, and a discrepancy between the experimental results and DFT calculations was found in the Mo and 2S peaks,

thus the results must be interpretated with caution, and it requires further experiments with better resolution and stability to confirm this assumption.

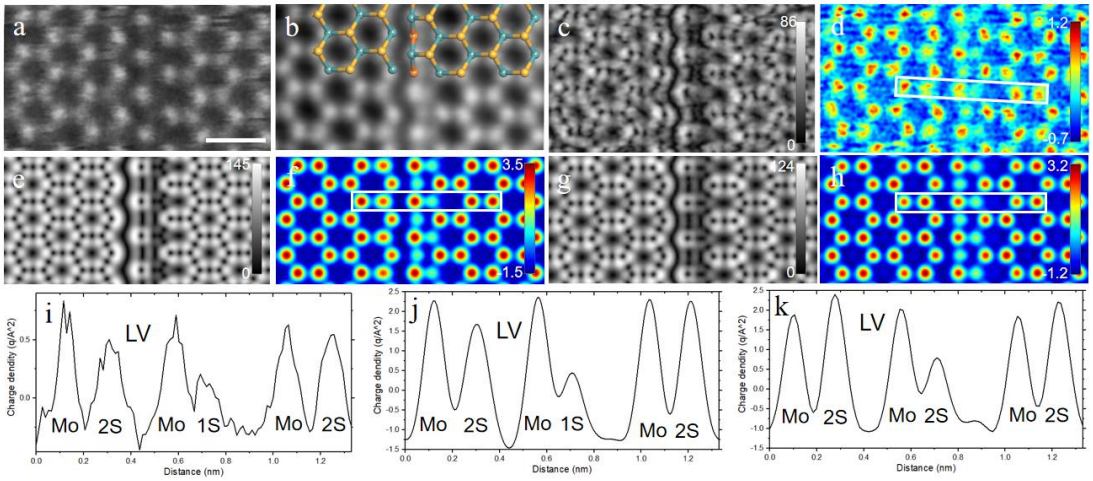


Figure 4.6. Analysis of line sulphur vacancy (LV). (a) LAADF-STEM image reconstructed from 40-60 mrad, (b) Phase of the same region, calculated from iCoM, superimposed by a crystal model constructed in Discovery Studio based on the atom positions in phase, where green ovals indicate Mo atoms, yellow ovals indicate 2S columns, and orange ovals indicate 1S columns. (c) $|\boldsymbol{E}_{\perp \boldsymbol{PC}}|$, (d) charge density of a LV in monolayer MoS_2, without Gaussian blurring. (e-f) DFT-calculated $|\boldsymbol{E}_{\perp \boldsymbol{PC}}|$ and total charge density based on model in panel b, respectively. (g-h) Multislice simulation of $|\boldsymbol{E}_{\perp \boldsymbol{PC}}|$ and total charge density based on IAM, respectively (i-k) Intensity line profiles indicated by boxed region in panel d, f and h, measured from the left to right. For $|\boldsymbol{E}_{\perp \boldsymbol{PC}}|$, calibration bar unit is V, for charge density maps, calibration bar unit is $q \cdot A^{-2}$. Scale bar in panel a indicates 0.5 nm and applies to panel b-h.

4.3 Nanopore and Edges

A 2D crystal can be considered as two classes of atoms, the lattice atoms that make up the bulk of the material, and the edge atoms that terminate a 2D crystal. MoS_2 is a semiconductor with a direct band gap in monolayer form which becomes indirect

when number of layers increases. However, MoS_2 edge terminations have been found to exhibit a localised metallic state,[9] potentially used for catalytic HER and hydro-desulphurization catalysis.[10-12] There are many reasons why edges may exhibit different properties from the bulk: a changed stoichiometry leading to unsaturated coordination and dangling bonds; a localised electronic state due to symmetry breaking with respect to the bulk[13] and accumulated excitons[14] due to charge transfer between MoS_2 and absorbed O_2.[15]

There are various methods to probe the electronic states of edge structures in 2D crystals. Multiphoton microscopy probes the nonlinear optical interaction,[13,16] but does not provide atomic resolution, while an edge at micrometre scale is rarely atomically flat, and it is hard to determine the absorbed species at the edge. Phase contrast imaging in the TEM provides some information on the electronic potential but it is often qualitative. Scanning tunnelling microscopy (STM)[11,17] and in-situ electrical measurement[18] can be used to measure the density of states and conductance respectively at atomic resolution. Recent works using electron energy loss spectroscopy in STEM has revealed new edge states in graphene with atomic resolution, showing how changes to atomic bonding leads to different unoccupied levels.[19-21]

There are also studies on 2D materials including graphene[2] and MoS_2[22,23], with some interesting electric field states and magnitude increases observed at the monolayer/bilayer step edge in graphene. However, more work is needed to image periodic uniform edge terminations in 2D crystals to fully understand the electric field states measured by 4D-STEM. In this section, I analysed the long uniform zig-zag edge states created in monolayer MoS_2 using an established in-situ annealing method.[24] 4D-STEM was then used to map the uniform electric fields along the edges, with simultaneous HAADF-STEM image acquisition for comparative

Z-contrast maps. I reconstructed electric field maps, LAADF-STEM images, and phase images with simultaneous ADF-STEM images, showing the structural rearrangement and enhanced electric fields of MoS_2 edges. Comparison between experimental results, DFT calculation, and multislice simulation based on IAM were carried out, but the near 2-fold enhancement was not observed in DFT calculation and IAM simulation. Current results did not show evidence of charge redistribution in the Mo zigzag edge, and further investigations should include the factor of probe incoherence.

Fig. 4.7a shows a schematic illustration of the 4D-STEM geometry, with the 2D high speed pixelated electron detector at the bottom. Fig. 4.7b shows a schematic that illustrates the relative electric fields in bulk and edge regions, where in the bulk the total field cancels to zero at the location d_B, which is nearly halfway between the Mo and 2S locations. At the edge, this distance d_E is larger because of the absence of a nearest neighbour which gives rise to new electric field distributions. Fig. 4.7c and d show the low magnification ADF-STEM image and the corresponding $|\boldsymbol{E}_{\perp \boldsymbol{PC}}|$, respectively, of an etched region in a monolayer MoS_2 at 700 °C. There are several different edge terminations around the hole, including the pristine zigzag edge (fig. 4.7c i), Mo-rich MoS nanowires attached to the zigzag edge (fig. 4.7c ii, detailed analysis in fig. 4.11) and Mo nanoclusters (fig. 4.7c iii and iv), and a small piece of residual amorphous carbon (fig. 4.7c iv).

Figure 4.7e and f show a high magnification ADF-STEM and $|\boldsymbol{E}_{\perp \boldsymbol{PC}}|$ map of MoS nanowire terminated edge, where the 1D confined edge state is observed at the outer region of the MoS wire. The Z-contrast ADF-STEM image of this region shows no increase along the outer edge, indicating that the electric field contrast increase is not simply from increased thickness in this region. Fig. 4.7g-i show a zig-zag edge, which appears as Mo-terminated in the ADF-STEM image in fig. 4.7g, but the iDPC

phase image in fig. 4.7h shows that there is weak contrast visible from S atoms that terminate the edge. The $|\boldsymbol{E}_{\perp \boldsymbol{PC}}|$ map, fig. 4.7i, also supports the presence of S atoms with contrast observed in this region.

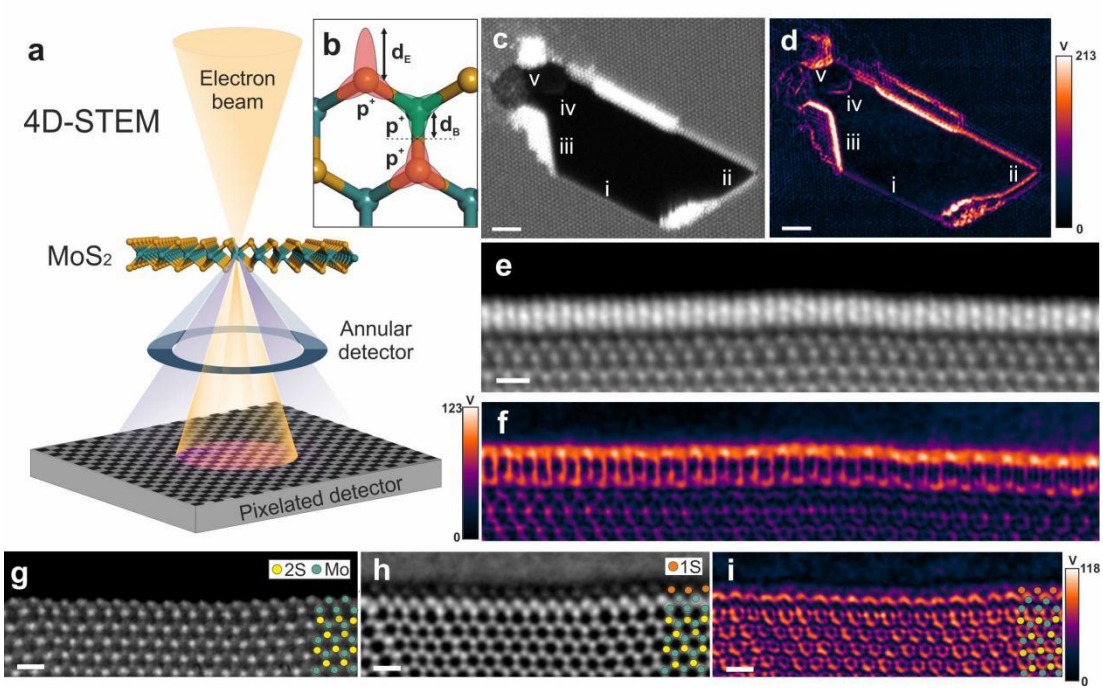


Figure 4.7. (a) Schematic illustration of the 4D-STEM geometry, showing an electron probe (yellow cones) passing through MoS_2 lattice. The grey ring indicates the ADF detector, the black mosaic square at the bottom indicates the fast pixelated detector. (b) Schematic diagram of a zigzag S-terminated edge. The shaded area signifies the interatomic interactions, d_B denotes the halfway distance between two adjacent bulk atoms, where the two atomic fields cancel out and the local electric field becomes minimal. d_E denotes the distance where the edge atomic fields drop to zero. (c) Simultaneous ADF-STEM image and (d) corresponding $|\boldsymbol{E}_{\perp \boldsymbol{PC}}|$ map calculated from the same 4D-STEM data set. i is a zigzag edge, ii is nanowire edge, iii is nanocrystal, iv is residual amorphous carbon and v is the nanocrystal edge with amorphous carbon. (e, f) LAADF-STEM and $|\boldsymbol{E}_{\perp \boldsymbol{PC}}|$ map of a nanowire edge, reconstructed from the same 4D-STEM data. (g-i) Atomic scale 4D-STEM reconstructed images of the same MoS_2 edge showing (g) ADF-STEM (h) phase reconstructed from iDPC. (i) reconstructed $|\boldsymbol{E}_{\perp \boldsymbol{PC}}|$ map. Scale bars in panel c and d indicate 2.0 nm. Scale bars in panel e and f indicate 0.5 nm. Scale bars in k, l, and m indicates 0.5

nm.

Edges were further analysed at higher magnification. Fig. 4.8a shows an ADF-STEM image of Mo-terminated zigzag edge, where the Mo and S atoms are arranged in a hexagonal lattice with a bare zigzag edge. However, I observed some additional atoms attached to the edges in the reconstructed phase (fig. 4.8b) which are not visible using ADF mode. These atoms are most likely to be the S atoms.[25] Each S atom is bonded to two Mo atoms, making the edge Mo saturated, which is a thermodynamically stable geometry.[26] Using the ADF-STEM image as a guide to locate atoms in the corresponding $|\boldsymbol{E}_{\perp \boldsymbol{PC}}|$ map (fig. 4.8c), I found that the edge Mo and additional S atoms exhibit higher electric field, compared to that of bulk atoms (fig. 4.8d, f). I have observed this consistently in both MoS_2 and WS_2 (fig. B6). In fig. 4.8e, the electric field vectors across the Mo zigzag edge showed stronger positive field (larger outwards vectors from the atom) than bulk atoms. A magnified vector map of a larger area can be found in Appendix B (fig. B7).

CBED pattern multislice simulations base on IAM were performed and used to reconstruct the $|\boldsymbol{E}_{\perp \boldsymbol{PC}}|$ maps in fig. 4.8g, based on the atomic model in fig. 4.8h. This shows a similar profile to the experimental data but does not match the enhanced electric field strength observed in the experimental data. Ishikawa et al.[2] reported enhanced electric fields along irregular edges and facet edges in graphene, which was attributed to unsaturated bonding of atoms. Some small enhancement of the electric field is seen in the simulated data in fig. 4.8g, but not in a sufficient amount to explain the experimental data in fig. 4.8c. Oxley and Dyck incorporate the influence from both spatial and temporal incoherence when simulating the CBED patterns and have achieved exact match between the experimental and simulated CoM,[3] which might explain part of the discrepancy.

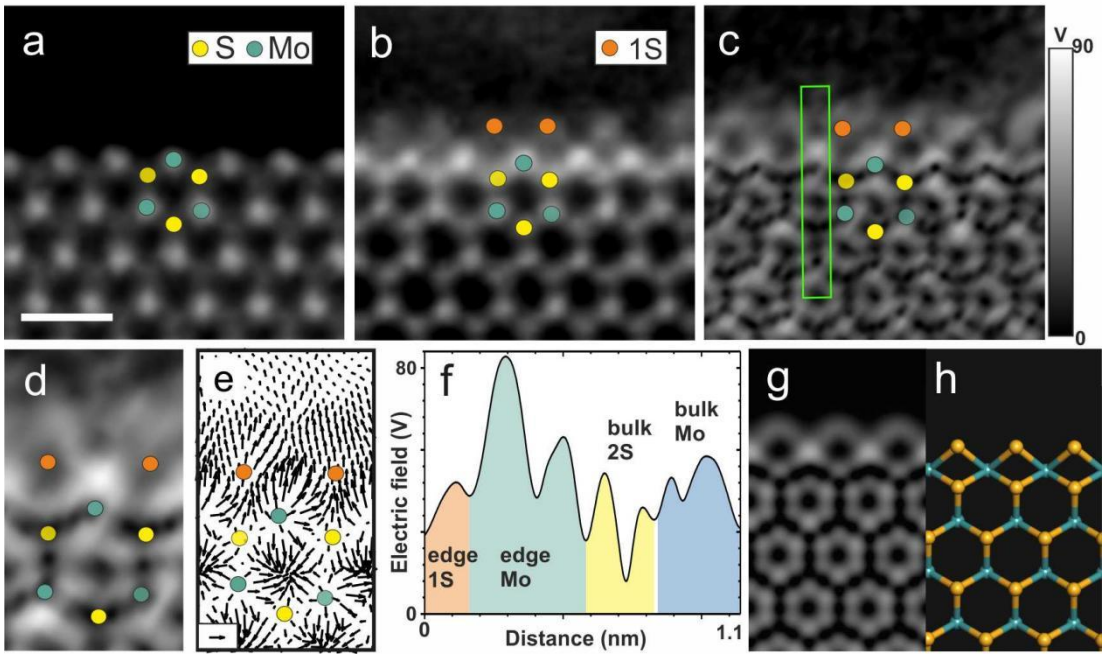


Figure 4.8. Detailed analysis of MoS_2 zigzag edge terminations. (a) HAADF-STEM image showing the Mo zigzag edge structure. (b) Reconstructed phase from iDPC showing additional atoms along the edge. (c) $|\boldsymbol{E}_{\perp \boldsymbol{PC}}|$ map calculated from 4D-STEM dataset, of the same region in panel b. Edge one S, bulk two S, and Mo atoms are indicated by orange, yellow and green ovals, respectively. (d) Enlarged image of panel c. (e) Vector plot of the $|\boldsymbol{E}_{\perp \boldsymbol{PC}}|$ map in panel d, showing an enhanced atomic field at an edge Mo atom. Scale bar indicates 40 V. (f) Intensity line profiles of box-indicated lengths (from top to bottom) in panel c, colour coded for different atoms, the twin peaks indicate the electric field splitting on opposite sides of the atom. (g) Multislice-simulated $|\boldsymbol{E}_{\perp \boldsymbol{PC}}|$ map based on IAM in (h). Scale bar in panel a indicates 0.5 nm and applies to panel b and c.

DFT calculations were used to compute $|E_{\perp}|$ maps using methods previously reported.[22] Fig. 4.9a shows the DFT calculated $|E_{\perp}|$ map of a MoS_2 ribbon that has a Mo zigzag edge with additional S (left side) and a bare S zigzag edge (right side). The electric field magnitude is seen to vary at the edges in fig. 4.9a, along with different spatial distribution compared to the central bulk area of the monolayer. Line profiles are plotted in fig.s 4.9b-d, taken from the coloured boxed areas shown in fig. 4.9a. The non-reconstructed, unsaturated S zigzag edge on the right side shows

significant electric field increase at the edge in fig. 4.9d, confirming that field enhancement is expected from theory in S zigzag edge without absorbed atoms.

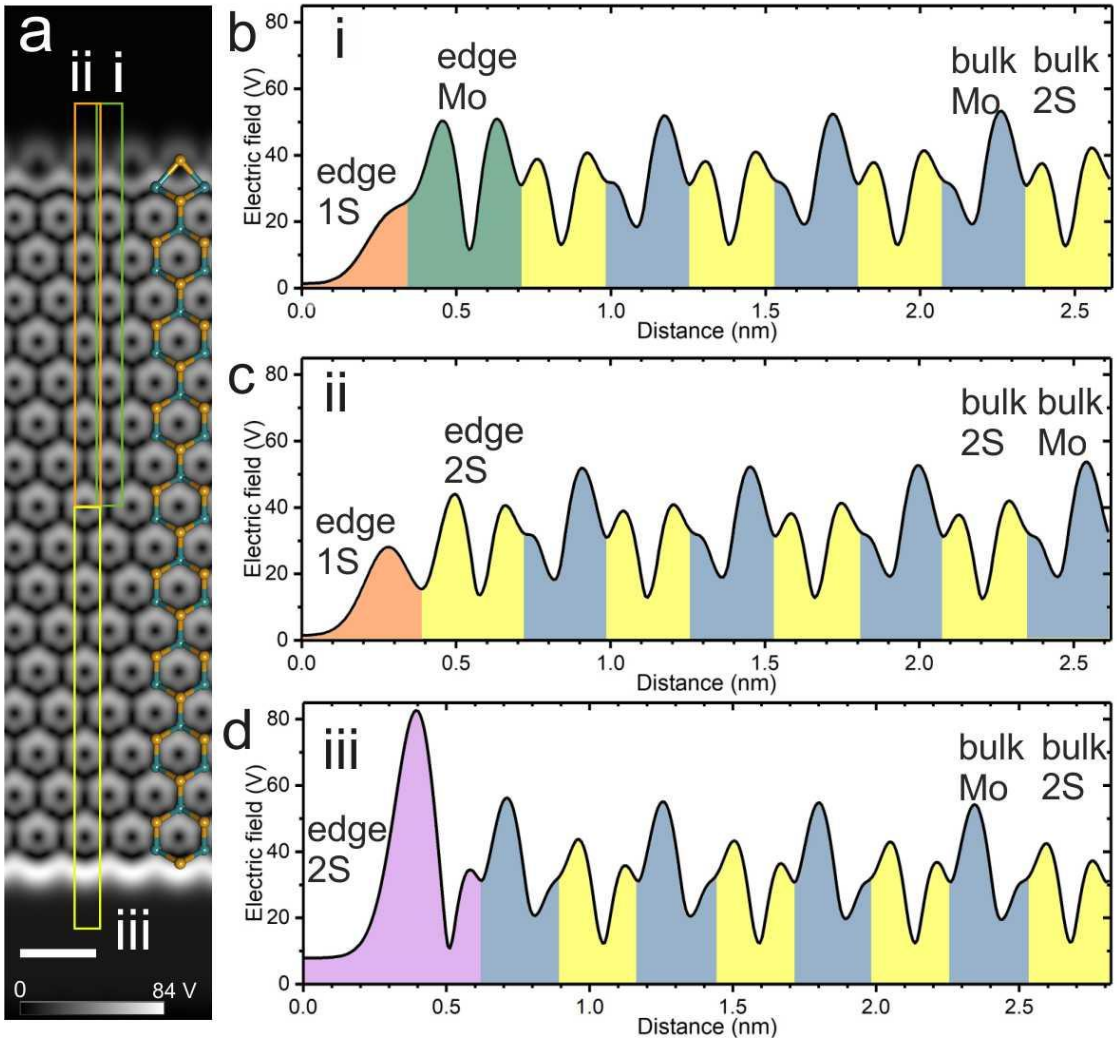


Figure 4.9. DFT calculations of the electric field magnitude at the edges of MoS_2. (a) Calculated $|E_\perp|$ map of MoS_2 ribbon with an overlaid crystal model, the top side is Mo zigzag edge with additional S atoms, the bottom side is S zigzag edge. (b-d) Line profiles taken from the coloured boxes labeled in (a) (i, ii, and iii) that include both edge and central regions of the sample. Scale bar in panel a indicates 0.5 nm.

Figure 4.10 shows the intensity line profiles across the Mo zigzag edge in experimental results (fig. 4.10a), DFT calculation (fig. 4.10b), and Multislice

simulation based on IAM (fig. 4.10c). The line profiles were normalized to the first 2S peak to compare the extent of enhancement in different $|\boldsymbol{E}_{\perp \boldsymbol{PC}}|$ map. It is apparent that the experimental results have shown the highest, close to 2-fold enhancement, while no enhancement was observed in DFT calculation as the Mo atoms at the edge were saturated, and multislice simulation showed a small enhancement. This comparison indicates that, part of the enhancement may be due to imaging artefact arising from partial coherence of the probe but is not the sole contribution to the profound enhancement in experimental results, detailed analysis is needed to confirm the underlying electronic turbulence caused by the edge structure, and such further investigation is beyond the scope of this thesis.

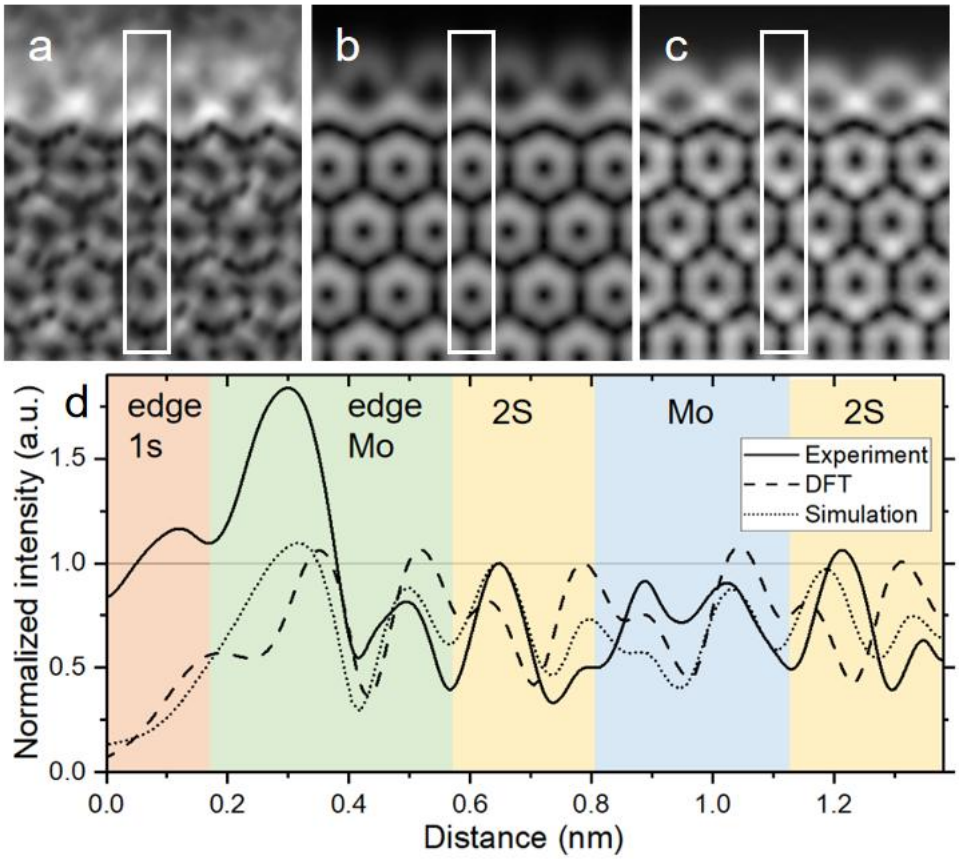


Figure 4.10. Comparison of $|\boldsymbol{E}_{\perp \boldsymbol{PC}}|$ across Mo zigzag edge from (a) Experimental result, (b) DFT calculation, and (c) multislice simulation based on IAM. (d) Normalized intensity line profiles of boxed region indicated in panel a-c. All line profiles were measured from the top of the rectangle to the bottom. Experimental result (solid line), multislice simulation (dotted

line), and DFT calculation (dashed line) were normalized to the first 2S peak on the right side of the edge Mo atom.

Next, I explored the reconstructed MoS nanowire edge termination in more detail. Unlike bottom-up fabrication,[27-29] the nanowires in our experiment were directly formed by reconstruction at the MoS_2 monolayer edge during heating and S loss (fig. B8). The nanowire can rotate and flex under electron beam irradiation,[18] giving rise to complex projections at different angles.[30] Fig. 4.11a-c shows the ADF-STEM image, reconstructed phase, and $|\boldsymbol{E}_{\perp \boldsymbol{PC}}|$ map of a MoS nanowire attached to a Mo zigzag edge, as observed in fig. 4.7. The $|\boldsymbol{E}_{\perp \boldsymbol{PC}}|$ perpendicular to the edge is plotted in fig. 4.11e and shows an increase at the outermost region of the edge. I performed 4D-STEM image simulations based on IAM and reconstructed the $|\boldsymbol{E}_{\perp \boldsymbol{PC}}|$ maps as shown in fig. 4.11f, using the atomic model in fig. 4.11g, which also exhibited enhanced $|\boldsymbol{E}_{\perp \boldsymbol{PC}}|$ at edge which indicates that the edge effect on MoS nanowire is not pronounced and may be attributed to imaging artefact.

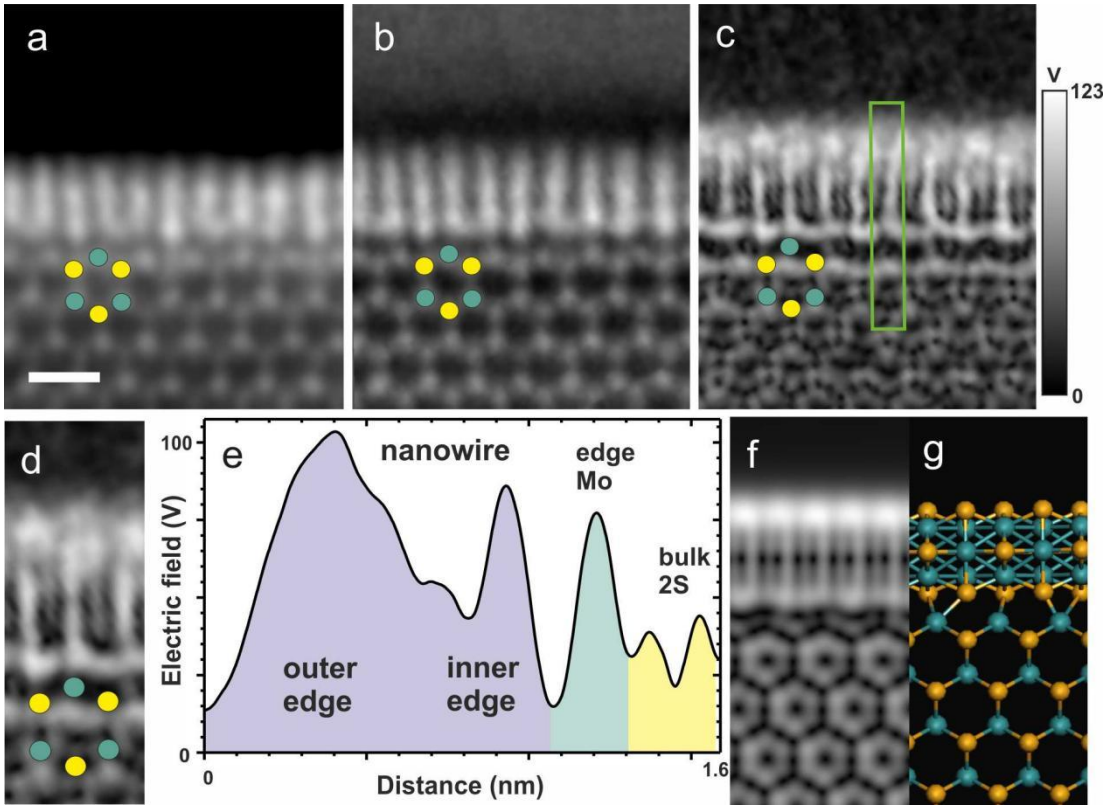


Figure 4.11. (a) ADF-STEM image of a nanowire attached to Mo zigzag edge. (b) Reconstructed phase from iDPC and (c) corresponding $|\boldsymbol{E}_{\perp \boldsymbol{PC}}|$ map. (d) Enlarged image of panel c. (e) Intensity line profile box-indicated lengths (starting from 1 to 2) in panel c, colour coded for different atoms. (f) Reconstructed $|\boldsymbol{E}_{\perp \boldsymbol{PC}}|$ map from multislice simulated 4D-STEM data using the IAM in (g). Scale bar in panel a indicates 0.5 nm and applies to panel b and c.

4.4. Conclusions

4D-STEM was used to reconstruct probe-convolved projected electric field maps of perfect lattice, point and line vacancies and edge regions of 2D materials MoS_2 and WS_2. Analysis of single sulphur vacancy matched well with DFT calculation and IAM simulation, while double sulphur vacancies were rarely observed in my experiments. The charge density map helped to identify substitutional atoms at the double sulphur vacancy sites, which were assumed to be carbon atoms, supported by IAM simulation, while the LAADF-STEM images could not differentiate the unfilled and filled double sulphur vacancies. Study of line sulphur vacancy has shown an electron-rich region possibly due to Mo-Mo bondings which was observed as a decrease in total charge density in this region. DFT calculation of total charge and electron density supported this result, while IAM simulation failed to predict this phenomenon, indicating that the decrease in total charge is not due to imaging artefact. However, in the experimental results, the fluctuations of charge density are in the range of scan noise, which called for further measurements with more stability. The detailed analysis of reconstructed zigzag edge structure in MoS_2 showed an abnormal edge enhancement of probe-convolved projected electric field. Discrepancy between DFT and multislice simulation based on IAM with experimental results indicated that the enhancement may come from the previously reported partial coherence of probe as the enhancement was not predicted by the

DFT calculation.[3] Thus, quantitative simulation must be carried out to differentiate the enhancement from different sources. To sum up, this chapter showcased how 4D-STEM can visualize contrast features that are not detected using conventional ADF-STEM imaging, but some changes in electronic properties due to defective structures were not efficiently imaged using 4D-STEM, which was due to the inevitable convolution with the imaging probe obscuring the results and the insufficient sensitivity of the technique to detect small fluctuations. Still, 4D-STEM analysis of the prototype 2D TMDs opens the way for future work on detailed analysis of defective structures in a wide range of ultrathin materials.

References

1. Lazić, I., Bosch, E. G. T., & Lazar, S. Phase contrast STEM for thin samples: Integrated differential phase contrast. *Ultramicroscopy* **160**, 265–280 (2016).
2. Ishikawa, R., *et al.* Direct Electric Field Imaging of Graphene Defects. *Nat. Commun.* **9**, 3878 (2018).
3. Oxley, M. P. & Dyck, O. E. The importance of temporal and spatial incoherence in quantitative interpretation of 4D-STEM. *Ultramicroscopy* **215**, 113015 (2020).
4. Tao, L. *et al.* Intrinsically Substitutional Carbon Doping in CVD-Grown Monolayer MoS_2 and the Band Structure Modulation *ACS Applied Electronic Materials*. **2** (2020)
5. Wang, S., Lee, G-D, Lee, S., Yoon, E., & Warner, J. H. Detailed Atomic Reconstruction of Extended Line Defects in Monolayer MoS_2. *ACS Nano* **10**, 5419–5430 (2016).
6. Le, D., Rawal, T. B., & Rahman, T. S. Single-layer MoS_2 with sulfur vacancies: Structure and catalytic application. *J. Phys. Chem. C* **118**, 5346–5351 (2014).
7. Komsa, H. P., Kurasch, S., Lehtinen, O., Kaiser, U., & Krasheninnikov, A. V. From point to extended defects in two-dimensional MoS_2: Evolution of atomic structure under electron irradiation. *Phys. Rev. B - Condens. Matter Mater. Phys.* **88**, 1–8 (2013).
8. Chen, Q. *et al.* Atomically Flat Zigzag Edges in Monolayer MoS_2 by Thermal Annealing. *Nano Lett.* **17**, 5502−5507 (2017).
9. Bollinger, M. V. *et al.* One-Dimensional Metallic Edge States in MoS_2. *Phys. Rev. Lett.* **87**, 196803 (2001).
10. Li, Y. *et al.* MoS_2 Nanoparticles Grown on Graphene: An Advanced Catalyst for the Hydrogen Evolution Reaction. *J. Am. Chem. Soc.* **133**, 7296–7299 (2011).
11. Jaramillo, T. F. *et al.* Identification of Active Edge Sites for Electrochemical H_2 Evolution from MoS_2 Nanocatalysts. *Science* **317**, 100–102 (2007).
12. Lukowski, M. A. *et al.* Enhanced Hydrogen Evolution Catalysis from Chemically Exfoliated Metallic MoS_2 Nanosheets. *J. Am. Chem. Soc.* **135**, 10274–10277 (2013).
13. Yin, X. *et al.* Edge Nonlinear Optics on a MoS_2 Atomic Monolayer. *Science* **344**, 488–490 (2014).
14. Gutiérrez, H. R. *et al.* Extraordinary Room-Temperature Photoluminescence in Triangular WS_2 Monolayers. *Nano Lett.* **13**, 3447–3454 (2013).
15. Nan, H. *et al.* Strong Photoluminescence Enhancement of MoS_2 Through Defect Engineering and Oxygen Bonding. *ACS Nano* **8**, 5738–5745 (2014).
16. Lin, K. I. *et al.* Atom-Dependent Edge-Enhanced Second-Harmonic Generation on MoS_2 Monolayers. *Nano Lett.* **18**, 793–797 (2018).
17. Bruix, A. *et al.* In Situ Detection of Active Edge Sites in Single-Layer MoS_2 Catalysts. *ACS Nano* **9**, 9322–9330 (2015).
18. Lin, J. *et al.* Flexible Metallic Nanowires with Self-Adaptive Contacts to

Semiconducting Transition-Metal Dichalcogenide Monolayers. *Nat. Nanotechnol.* **9**, 436–442 (2014).
19. Warner, J. H., Lin, Y. C., He, K., Koshino, M., & Suenaga, K. Atomic Level Spatial Variations of Energy States along Graphene Edges. *Nano Lett.* **14**, 6155–6159 (2014).
20. Warner, J. H., Liu, Z., He, K., Robertson, A. W., & Suenaga, K. Sensitivity of Graphene Edge States to Surface Adatom Interactions. *Nano Lett.* **13**, 4820–4826 (2013).
21. Suenaga, K. & Koshino, M. Atom-by-atom Spectroscopy at Graphene Edge. *Nature* **468**, 1088–1090 (2010).
22. Fang, S. *et al.* Atomic Electrostatic Maps of 1D Channels in 2D Semiconductors using 4D Scanning Transmission Electron Microscopy. *Nat. Commun.* **10**, 1127 (2019).
23. Müller-Caspary, K. *et al.* Atomic-Scale Quantification of Charge Densities in Two-Dimensional Materials. *Phys. Rev. B* **98**, 121408 (2018).
24. Chen, Q. *et al.* Atomically Flat Zigzag Edges in Monolayer MoS_2 by Thermal Annealing. *Nano Lett.* **17**, 5502−5507 (2017).
25. Hansen, L. P. *et al.* Atomic-scale edge structures on industrial-style MoS_2 nanocatalysts. *Angew. Chemie. Int. Ed.* **50**, 10153–10156 (2011).
26. Schweiger, H., Raybaud, P., Kresse, G., & Toulhoat, H. Shape and Edge Sites Modifications of MoS_2 Catalytic Nanoparticles Induced by Working Conditions: A Theoretical Study. *J. Catal.* **207**, 76–87 (2002).
27. Xu, H. *et al.* Oscillating Edge States in One-Dimensional MoS_2 Nanowires. *Nat. Commun.* **7**, 12904 (2016).
28. Xu, H. *et al.* Controllable Synthesis of 2D and 1D MoS_2 Nanostructures on Au Surface. *Adv. Funct. Mater*. **27**, 1603887 (2017).
29. Li, S. *et al.* Vapour–Liquid–Solid Growth of Monolayer MoS_2 Nanoribbons. *Nat. Mater*. **17**, 535-542 (2018).
30. Koh, A. L., Wang, S., Ataca, C., Grossman, J. C., & Sinclair, R., Torsional Deformations in Subnanometer MoS Interconnecting Wires. *Nano Lett.* **16**, 1210–1217 (2016).

Chapter 5 Graphene Moiré Superlattices

5.1 Introduction

Moiré superlattices form when two lattices superimpose and rotate with each other. The interlayer rotation creates complex periodic features whose size are a function of the lattice constant and the twist angle. Such superlattice has unique interlayer coupling and ordering that result in electrical and optical properties different from that of the constituent materials,[1-4] opening new opportunities in the field of 'twistronics'. Among them, twisted bilayer graphene (TBG) may be the simplest turbostratic structure due to its inherent simplicity. Because of the six-fold symmetry of graphene lattice, the discussion of twist angle is confined in $0 < \theta < 30°$. The precise control of the twist angle between layers of 2D materials has been achieved by wet transfer method,[5,6] CVD synthesis,[7,8] and folding.[9,10] For small twist angle, TBG shows a large moiré superlattices, strong interlayer coupling,[11] and moiré superlattice gaps.[12138] And at specific 'magic angle', for example a small twist angle of ~1.1°, moiré superlattices in the TBG can induce half-filling insulator states and gate-tunable superconductivity.[2,13] At large twist angles, this interlayer hybridization ceased[14] and for 30° quasicrystalline TBG, the graphene become decoupled and can be regarded as two individual monolayer graphene.[7,15139,140] There has been extended studies of more complex systems like twisted trilayer graphene (TTG),[16-18] twisted bilayer-bilayer graphene (TBBG),[19-21] and other 2D materials and heterostructures, which all require a better microscopic understanding.

Raman spectroscopy is a common characterization methods for twisted graphene layers as the interlayer coupling in TBG leads to measurable changes in the intensity, position, and shape of the G and 2D Raman peaks.[22-24] Scanning tunnelling microscopy/spectroscopy (STM/STS) has also been used to study the topographic

structures and electronic properties of twisted graphene layers at atomic resolution[25-27] but the effect of the substrate must be considered. 4D-STEM provides a pathway into *in situ* observation of electronic environment of moiré superlattices with simultaneous atomic resolution imaging.[28,29] By using a fast pixelated detector, I recorded the BFD for post-acquisition reconstruction of electric field (fig. 5.1a), while the simultaneous Z-contrast ADF-STEM image act as a reference. In this section, I examined two types of twisted multilayer graphene and their moiré patterns, one from an epitaxial TBG with near-30° twist angle and one from backfolded TTG with a small twist angle of 3° between the first and the third layer, but large (> 23°) twist angles between the first and the second, the second and the third layer, respectively. In both the TBG and TTG, I found a close match between the experimental results and IAM simulation, which indicate that either these two systems with large twist angles both show decoupling behaviour, or the fluctuations in the electric field and charge density are below the sensitivity of the current technique.

5.2 Results and discussion

Graphene samples were synthesized via CVD on Cu foil and transferred onto DENS heating chips for *in situ* annealing and STEM imaging. Fig. 5.1b shows a monolayer graphene bottom layer (I) and an epitaxial top layer (II) with no visible wrinkle or grain boundary. Inset shows the corresponding FFT of fig. 5.1b. There are two sets of hexagonally distributed reflections at 0.21 nm/c which corresponds to 1-100 plane of graphene, and there are a 28.4±0.1°-rotation between them, indicating a 28.4°-rotation between the bottom and top layer in real space,[30,31] and the brighter set of reflections corresponds to the larger bottom layer. The magnified ADF-STEM images shows that a periodic pattern in the bilayer region. Fig. 5.1e-g shows that a

smaller twist angle (θ) produces large moiré pattern and vice versa. The numerical relation between θ and moiré wavelength (λ) can be expressed as[32141]

$$\lambda = a/[2\sin\left(\frac{\theta}{2}\right)] \ (eq.5.1)$$

where a is lattice constant (a = 0.246 nm for graphene). For the measured θ = 28.4°, the corresponding λ = 0.51 nm.

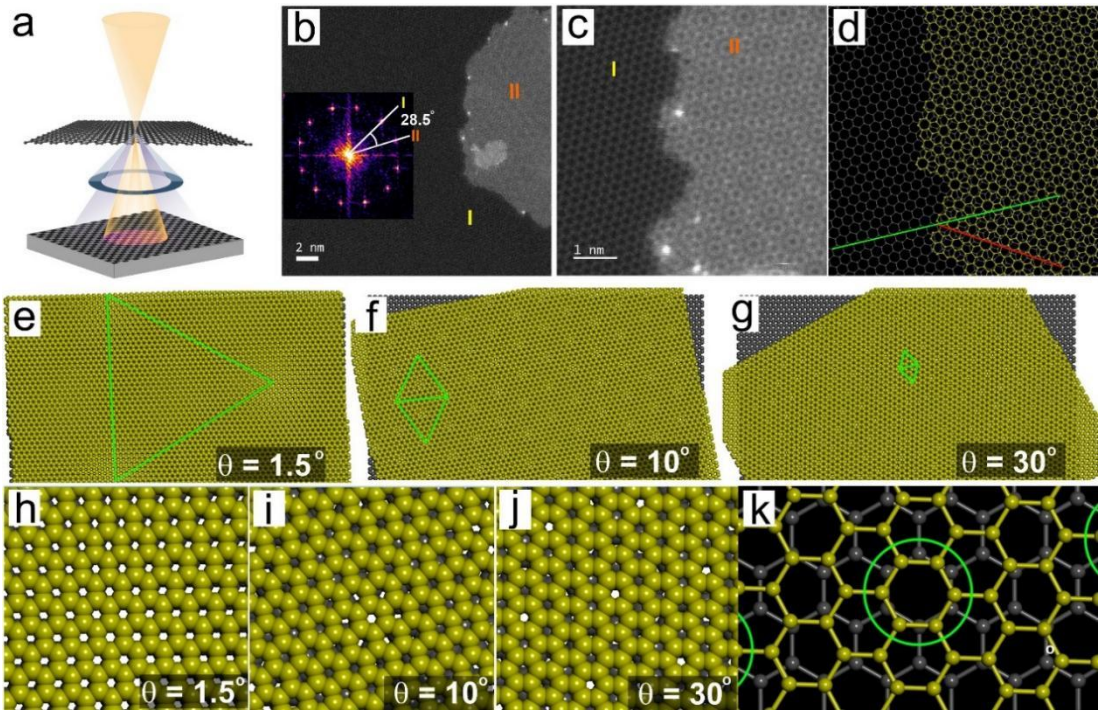


Figure 5.1. (a) Schematics of 4D-STEM. (b) medium-angle (MA) ADF-STEM image showing a bottom layer graphene (I) and an epitaxial top layer (II). Inset shows the corresponding fast Fourier transform of the image, where the twist angle between two sets of reflections is 28.4°. False colour LUT is gem. (c) MAADF-STEM image showing the irregular edge, Si atoms attached to the edge, and moiré pattern of the epitaxial layer. (d) crystal model based on panel c. Green (red) line indicates the zigzag direction of the bottom (top) layer. (e-g) Crystal models of bilayer graphene with different twist angles of 1.5°, 10.0° and 30.0°, respectively. Green triangles indicate the size of the periodic patterns. (h-j) enlarged models of panels e-g, respectively. (k) Ball and stick crystal model showing a clearer representation of the moiré pattern. Green circle indicates the centre of the periodic pattern.

To explore the electric field modulations within the large twist angle bilayer moiré superlattice, I performed 4D-STEM analysis on the region in fig. 5.1c. Fig. 5.2a-c shows the simultaneous ADF-STEM image, phase calculated from iCoM, and projected probe-convolved electric field ($|\boldsymbol{E}_{\perp \boldsymbol{PC}}|$) map of the enlarged step-edge region as shown in fig. 5.1b, c. Based on the FFT spectrum in fig. 5.1b, I construct a rigid body crystal model (fig. 5.2d) of two graphene layers with 28.4° rotation and performed multislice simulation of the phase (fig. 5.2e) and the $|\boldsymbol{E}_{\perp \boldsymbol{PC}}|$ map (fig. 5.2f) based on IAM. Both the phase and the $|\boldsymbol{E}_{\perp \boldsymbol{PC}}|$ map are in good accordance with experimental results. The phase imaging in fig. 5.2b and e show the contrast features of a central ring surrounded by twelve pentagons. The central ring contrast is due to the overlapping hexagons and comprises twelve atoms in total, as illustrated in fig. 5.1k. Fig. 5.2g shows a magnified view of the $|\boldsymbol{E}_{\perp \boldsymbol{PC}}|$ map in fig. 5.2c. In the monolayer graphene region on the left in fig. 5.2g, similar hexagonal electric field patterns were observed as previously reported.[33] In the bilayer moiré region on the right in fig. 5.2g, the electric field shows several concentric rings in the centre, followed by twelve pentagons. This feature is indicated by the white circle in fig. 5.2c, f, and g.

To understand the nature of these fluctuations in the $|\boldsymbol{E}_{\perp \boldsymbol{PC}}|$ map, I plotted $\boldsymbol{E}_{\perp \boldsymbol{PC}}$ vector map of the central ring structure (fig. 5.3a). It becomes apparent that the central ring and the first 'crest' are the outward $\boldsymbol{E}_{\perp \boldsymbol{PC}}$ from the dodecagon in the centre, and the 'trough' in between is the position of the twelve carbon atoms. The second 'crest' is the outward $\boldsymbol{E}_{\perp \boldsymbol{PC}}$ from the outer twenty-four carbon atoms, where they cancel out with the first 'crest' and form the second 'trough'. The enhancement observed on central ring should be attributed to the high density of atoms concentrated in the central dodecagon. The charge density map in fig. 5.2h and 5.3b also show a high concentration of negative charges inside the central ring that form

local minima. Simulation of $|\boldsymbol{E}_{\perp \boldsymbol{PC}}|$ (fig. 5.2j) and charge density (fig. 5.3c) based on IAM are in accordance with the experimental results, indicating there is no detectable interlayer coupling as the TBG acted as independent layers, or there may be interactions but is below the sensitivity of this imaging method, between the two graphene layers with rotation of 28.4°, as found in studies with large twist angle TBG.[7,15]

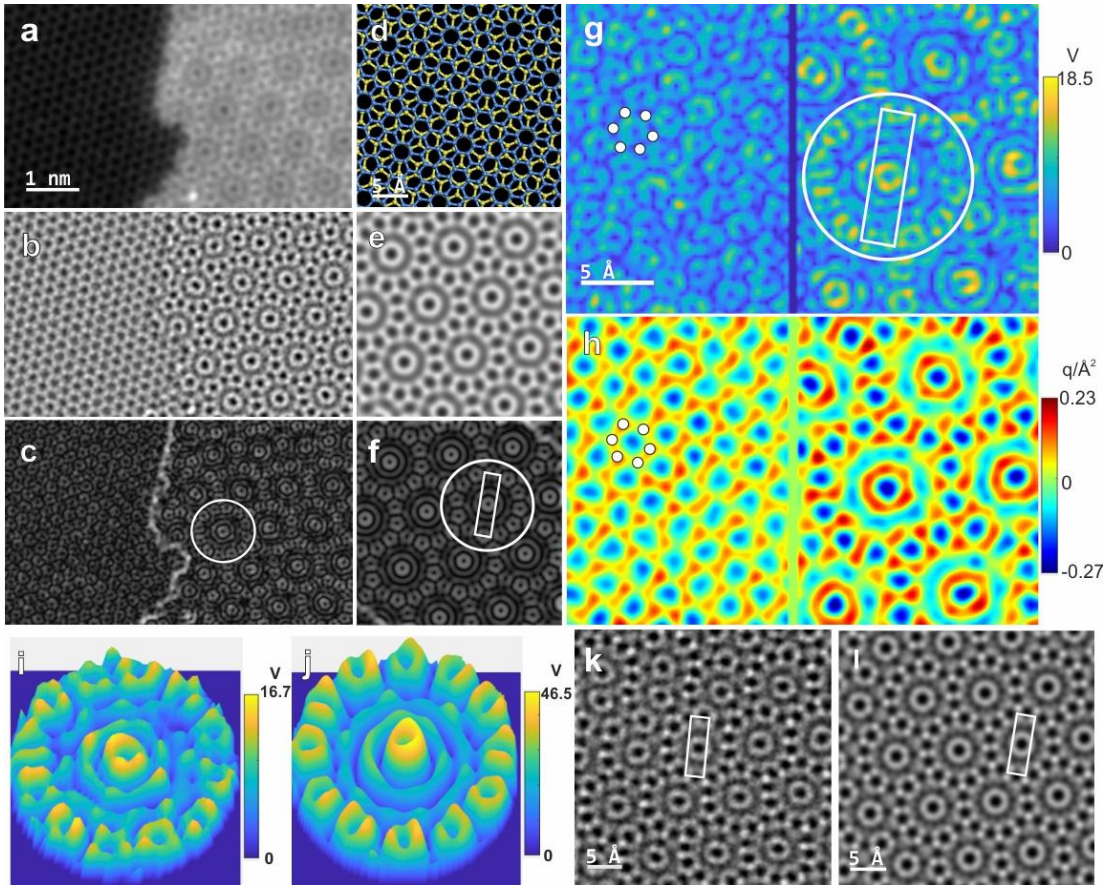


Figure 5.2. (a-c) Simultaneous ADF-STEM image, phase calculated from iCoM, and magnitude of the projected probe-convolved electric field ($|\boldsymbol{E}_{\perp \boldsymbol{PC}}|$) of the step edge region, respectively. White circle in panel c indicates a repetitive pattern. (d) Crystal model of the twisted bilayer region. (e, f) Phase and $|\boldsymbol{E}_{\perp \boldsymbol{PC}}|$ map from multislice-simulated 4D-STEM data based on IAM, respectively. (g, h) Enlarged $|\boldsymbol{E}_{\perp \boldsymbol{PC}}|$ map from panel c and corresponding charge density map. The step edge region is cropped out for better contrast between mono- and bilayer region. White ovals indicate the position of carbon atoms.

Colormap is (g) parula and (h) jet, respectively. (i, j) Three-dimensional surface plot of circled region in panel g and f with smoothing, showing oscillations. Colormap is parula. (k) High resolution MAADF-STEM image and (l) simulated MAADF-STEM image of the bilayer region. Scale bar in panel a applies to panel b and c, scale bar in panel d applies to e and f, scale bar in panel g applies to panel h.

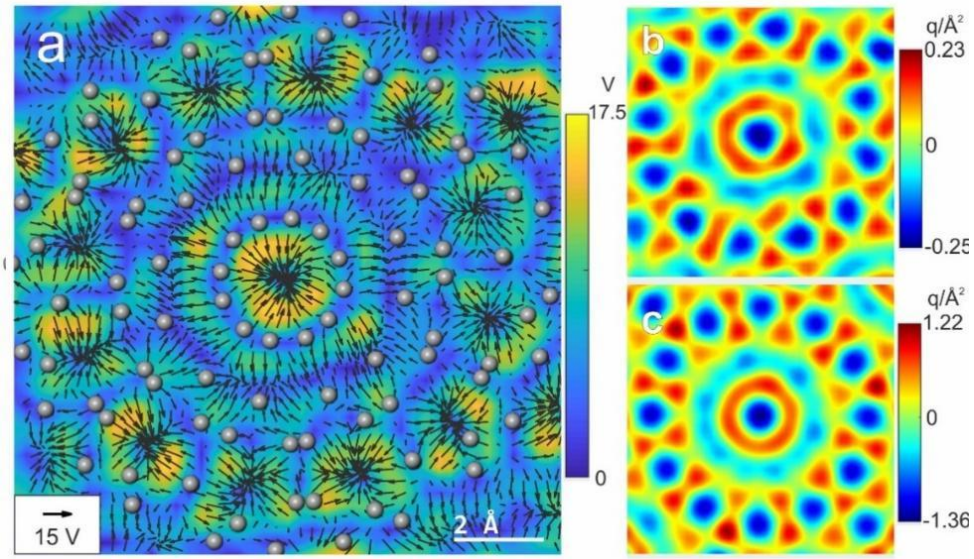


Figure 5.3. (a) $E_{\perp}$ vector (black arrows) map and crystal model (gray ovals) overlaid on the $|\boldsymbol{E}_{\perp \boldsymbol{PC}}|$ map (colormap is parula) of bilayer moiré pattern. (b) Charge density map of the same region in panel a. (c) Multislice-simulated charge density map based on IAM.

Now that the moiré features in typical large angle twist bilayer graphene are well understood, I can study the backfolded graphene, which adds a third layer to the system at low twist angle. Fig. 5.4 shows the backfolding type of turbostratic graphene, where a continuous monolayer graphene first folded backwards and then folded backwards again, rendering a trilayer region amid the monolayer graphene that resembles turbostratic trilayer graphene.[34] Intensity line profile in fig. C1d shows that the trilayer region has a relatively uniform thickness, and low magnification ADF-STEM image in fig. 5.4d shows that there was no grain boundary in any of the layer. The FFT of the trilayer region shows that there are three sets of hexagonally

distributed reflections at 0.21 nm/c, representing three layers of graphene, denoted as 1 (bottom layer), 2 (middle layer), and 3 (top layer), respectively, where $\theta_{12} = 26.3°, \theta_{23} = 23.3°, \theta_{13} = 3.0°$. Equation 1 gives the wavelength of the first order Moiré patterns M_{12}, and M_{23}, where $\lambda_{12} = 0.6\,nm$ and $\lambda_{23} = 0.5\,nm$, and the corresponding lattice vectors marked in fig. 5.3b were deducted from the lattices vectors of the monolayers.[7] The experimentally observed reflections in reciprocal space (fig. 5.4f) were well reproduced in the simulated FFT spectrum (fig. 5.4g). Other reflections beyond the first order moiré patterns seen in fig. 5.4f and g are harmonics that arise from the many Moiré of Moiré periodicities. Some of these are highlighted in shades of blue in fig. 5.4h, i, with spatial periodicities between the 0.6 nm and 2.5 nm region. Each first order moiré generates a hexagon, and a star is constructed when including the second order reflections of the first order moirés that occur at half the periodicity with 30° rotation.

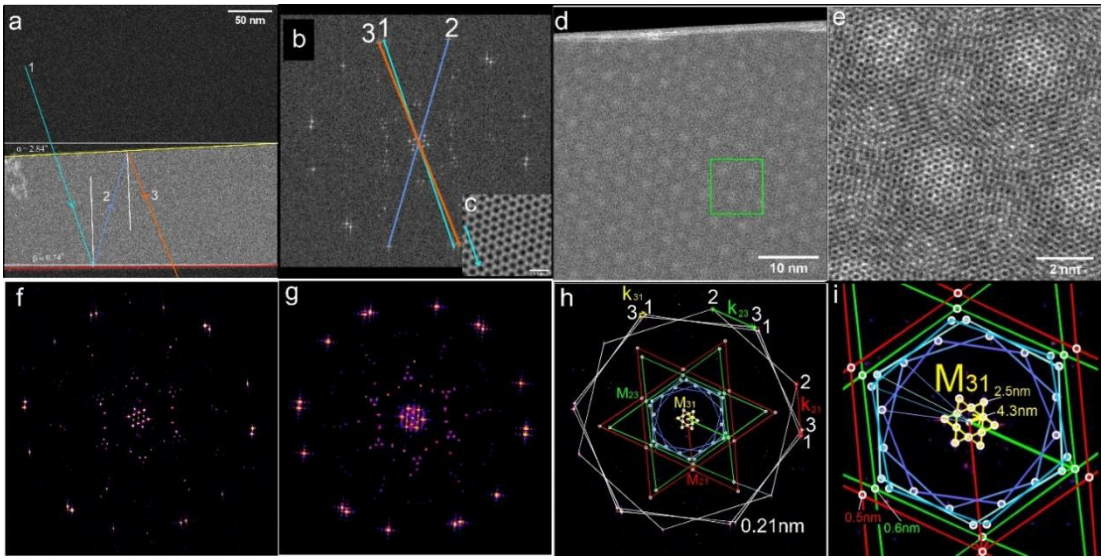


Figure 5.4. (a) ADF-STEM image of a S-bend pleat in graphene. Colour arrows indicate layer orientations after backfolding. Backfolding angles are labelled. (b) Power spectrum calculated by the FFT of the ADF-STEM image in panel d. Colour lines are used to indicate the three graphene layers that match panel a. (c) Atomic resolution ADF-STEM image of the graphene lattice in region 1 (bottom layer) of panel a, with the cyan arrow indicating the

lattice vector direction that matches panel a. (d) Large area ADF-STEM image of the S-bend pleat with atomic information that was used to generate panel b. (e) Atomic resolution ADF-STEM image of the area indicated with the green box in panel d. (f) Power spectrum calculated by a FFT from the image in (d). (g) Power spectrum calculated by a FFT from a multislice image simulation of an equivalent constructed trilayer moiré atomic structure. (h) Indexing of the reflections in the power spectrum shown in panel (f). (i) Higher magnification view of the inner low frequency region of panel h, showing the moiré reflection spacings. Blue hexagons indicate reflections due to moiré of moirés.

Fig. 5.5 shows the comparison of experimental $|\boldsymbol{E}_{\perp \boldsymbol{PC}}|$ and multislice simulation of $|\boldsymbol{E}_{\perp \boldsymbol{PC}}|$ based on the IAM (crystal model shown in fig. C2). Surprisingly, besides the discrepancy in magnitude due to inaccurate simulation of probes, the spatial distribution in experimental and simulated $|\boldsymbol{E}_{\perp \boldsymbol{PC}}|$ are in good accordance. This indicates that this trilayer configuration exhibits similar behaviour as the decoupled bilayer case. This could either be due to the interlayer (layer 2) that screened the interactions between layer 1 and 3,[35] or the coupling effects due to the twist angle of 3.0° may be below the sensitivity of this measurement technique.

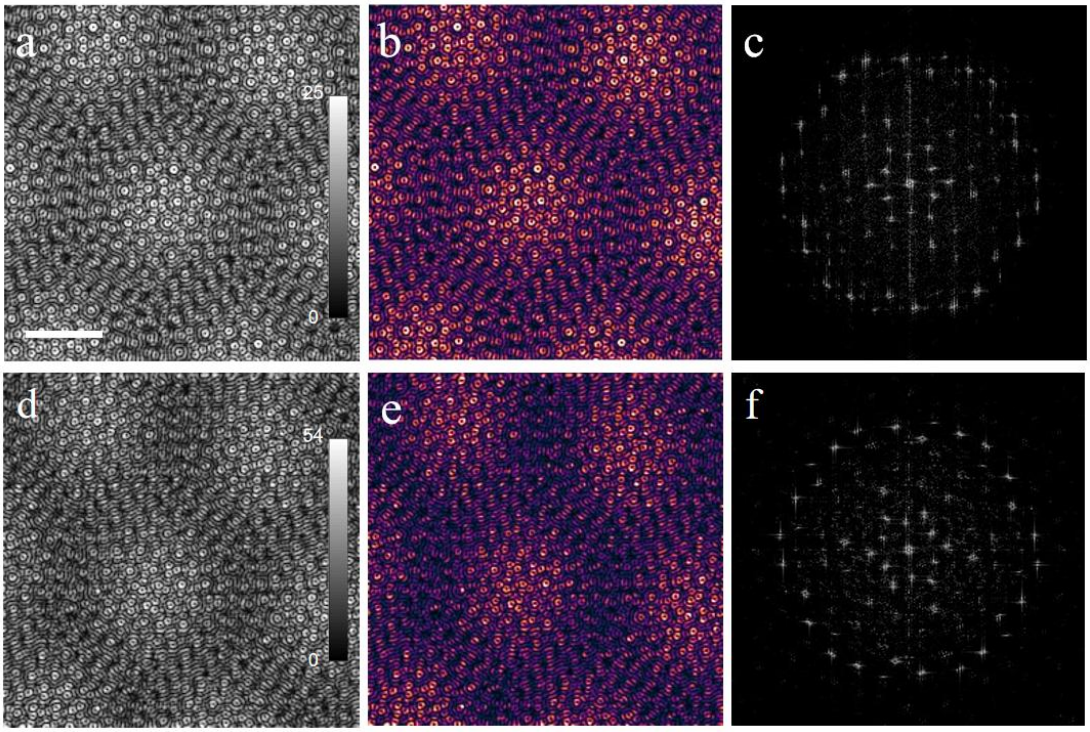


Figure 5.5. Comparison of experimental $|\boldsymbol{E}_{\perp \boldsymbol{PC}}|$ and multislice simulation based on IAM. (a) Experimental $|\boldsymbol{E}_{\perp \boldsymbol{PC}}|$ map of the back-fold trilayer graphene, (b) same figure in panel a with colour for better visualization, and (c) its FFT spectrum. (d) Multislice-simulated $|\boldsymbol{E}_{\perp \boldsymbol{PC}}|$ map based on IAM of the back-fold trilayer graphene, (e) same figure in panel a with colour for better visualization, and (f) its FFT spectrum. False colour LUT in b-d is gem. Scale bar in panel b applies to panel b-f. Scale bar in panel a indicates 2 nm and applies to panel b, d, and e.

5.3 Conclusion

Two types of twisted multilayer graphene were characterized and analysed using 4D-STEM and it showed that the projected electric field in the moiré superlattices depends strongly on the twist angle. Large twist angle generates sub-nanometer concentric fluctuations due the near-12-fold symmetry of the Moiré lattices, while small twist angle generates long-range periodic $|\boldsymbol{E}_{\perp \boldsymbol{PC}}|$ maxima. Both cases showed a good match with IAM simulations, no abnormal $|\boldsymbol{E}_{\perp \boldsymbol{PC}}|$ or charge density fluctuations were observed. This is either due to possible decoupling behaviour for

large twist angle, where graphene layers can be treated as individual layers; or, the fluctuations present were below the sensitivity of current 4D-STEM technique. This work provides an insight into the *in situ* observation of TBG moiré superlattices and connected the superstructure with the local electric field, which can be extended to other twisted 2D materials and heterostructures. Further investigations on 4D-STEM study of TBG and TTG with small twist angle are still intriguing, e.g., by combining the atomic-resolution 4D-STEM characterization with fabrication of TBG/TTG devices and varying operating temperature.

References

1. Zhang, C. et al. Interlayer couplings, Moiré patterns , and 2D electronic superlattices in MoS_2 / WSe_2 hetero-bilayers. *Sci. Adv.* **3**, e1601459 (2017).
2. Cao, Y. *et al.* Correlated insulator behaviour at half-filling in magic-angle graphene superlattices. *Nature* **556**, 80–84 (2018)
3. Seyler, K. L. *et al.* Signatures of moiré-trapped valley excitons in $MoSe_2$/WSe_2 heterobilayers. *Nature* **567**, 66–70 (2019)
4. McGilly, L. J. *et al.* Visualization of moiré superlattices. *Nat. Nanotechnol.* **15**, 580–584 (2020).
5. Liao, M. *et al.* Precise control of the interlayer twist angle in large scale MoS_2 homostructures. *Nat. Commun.* **11**, 1–8 (2020).
6. Hou, Y. *et al.* Preparation of Twisted Bilayer Graphene via the Wetting Transfer Method. *ACS Appl. Mater. Interfaces* **12**, 40958–40967 (2020).
7. Deng, B. *et al.* Interlayer Decoupling in 30° Twisted Bilayer Graphene Quasicrystal. *ACS Nano* **14**, 1656–1664 (2020).
8. Omambac, K. M. *et al.* Temperature-Controlled Rotational Epitaxy of Graphene. *Nano Lett.* **19**, 4594−4600 (2019).
9. Kim, K. *et al.* Multiply folded graphene. *Phys. Rev. B* **83**, 245433 (2011).
10. Rode, J. C. *et al.* Linking interlayer twist angle to geometrical parameters of self-assembled folded graphene structures. *2D Mater.* **6**, 15021 (2019).
11. Brihuega, I. *et al.* Unraveling the Intrinsic and Robust Nature of van Hove Singularities in Twisted Bilayer Graphene by Scanning Tunneling Microscopy and Theoretical Analysis. *Phys. Rev. Lett.* **109**, 196802 (2012).
12. Cao, Y. *et al.* Superlattice-Induced Insulating States and Valley-Protected Orbits in Twisted Bilayer Graphene. *Phys. Rev. Lett.* **117**, 116804 (2016).
13. Cao, Y. *et al.* Unconventional superconductivity in magic-angle graphene superlattices. *Nature* **556**, 43–50 (2018).
14. Bistritzer, R. & MacDonald, A. H. Moiré bands in twisted double-layer graphene. *Proc. Natl. Acad. Sci. U. S. A.* **108**, 12233–12237 (2011).
15. Pezzini, S. *et al.* 30°-Twisted Bilayer Graphene Quasicrystals From Chemical Vapor Deposition. *Nano Lett.* **20**, 3313–3319 (2020).
16. Zhu, Z., Carr, S., Massatt, D., Luskin, M., & Kaxiras, E. Twisted Trilayer Graphene: A Precisely Tunable Platform for Correlated Electrons. *Phys. Rev. Lett.* **125**, 116404 (2020).
17. Park, J. M., Cao, Y., Watanabe, K., Taniguchi, T., & Jarillo-herrero, P. Tunable strongly coupled superconductivity in magic-angle twisted trilayer graphene. *Nature* **590**, 249–255 (2021).
18. Ma, Z. *et al.* Topological flat bands in twisted trilayer graphene. *Sci. Bull.* **66**, 18–22 (2021).
19. Shen, C. *et al.* Correlated states in twisted double bilayer graphene. *Nat. Phys.* **16**, 520–525 (2020).

20. Cao, Y. *et al.* Tunable correlated states and spin-polarized phases in twisted bilayer–bilayer graphene. *Nature* **583**, 215–220 (2020).
21. Lee, K. *et al.* Ultrahigh-resolution scanning microwave impedance microscopy of moiré lattices and superstructures. *Sci. Adv.* **6**, eabd1919 (2020).
22. Havener R.W., Zhuang H., Brown L., Hennig R.G., Park J. Angle-resolved raman imaging of interlayer rotations and interactions in twisted bilayer graphene. *Nano Lett.* **12**, 3162–3167 (2012).
23. Robinson J.T. *et al.* Electronic hybridization of large-area stacked graphene films. *ACS Nano.* **7**, 637–644 (2011).
24. Han W. *et al.* Resonant Raman spectroscopy of twisted multilayer graphene. *Nat. Commun.* **5**, 5309 (2014).
25. Luican A. et al. Single-layer behavior and its breakdown in twisted graphene layers. *Phys Rev Lett.* **106**, 126802 (2011).
26. Zuo W.J. *et al.* Scanning tunneling microscopy and spectroscopy of twisted trilayer graphene. *Phys Rev B.* **97**, 035440 (2018).
27. Simon S. *et al.* Layer-by-Layer Decoupling of Twisted Graphene Sheets Epitaxially Grown on a Metal Substrate. *Small* **14**, 1703701 (2018).
28. Müller, K. *et al.* Atomic electric fields revealed by a quantum mechanical approach to electron picodiffraction. *Nat. Commun.* **5**, 5653 (2014).
29. Fang, S. *et al.* Atomic electrostatic maps of 1D channels in 2D semiconductors using 4D scanning transmission electron microscopy. *Nat. Commun.* **10**, 1127 (2019).
30. Warner, J. H., Rümmeli, M. H., Gemming, T., Büchner, B., & Briggs, G. A. D. Direct imaging of rotational stacking faults in few layer graphene. *Nano Lett.* **9**, 102–106 (2009).
31. Lu, C. C. *et al.* Twisting bilayer graphene superlattices. *ACS Nano* **7**, 2587–2594 (2013).
32. Miller, D. L. *et al.* Structural analysis of multilayer graphene via atomic moiré interferometry. *Phys. Rev. B - Condens. Matter Mater. Phys.* **81**, 125427 (2010).
33. Ishikawa, R. *et al.* Direct electric field imaging of graphene defects. *Nat. Commun.* **9**, 3878 (2018).
34. Robertson, A. W. *et al.* Structural Distortions in Few-Layer Graphene Creases. *ACS Nano* **5**, 9984–9991 (2011).
35. Zachman M.J. *et al.* Interferometric 4D-STEM for Lattice Distortion and Interlayer Spacing Measurements of Bilayer and Trilayer 2D Materials. *Small* **17**, 2100388 (2021).

Chapter 6 Simultaneous Identification of Low and High Atomic Number Atoms

6.1 Introduction

2D TMDs, including MoS_2 and WS_2, have shown potential use in ultrathin electronic devices due to their tunable band structure, flexibility, transparency, and scalable production using CVD methods.[1-3] These materials form atomically thin crystals with surface areas up to centimetre scale, making them suitable for applications that require a large specific surface area. This includes for example, loading of catalytically active particles, edge-decorated and surface-bound functional groups for sensors and the use of nanopores in a membrane for desalination and DNA translocation.[4-8] The nanopores in 2D crystals can be created by electrochemical reactions, oxygen plasma etching, ion beam irradiation and in-situ electron beam engineering.[9-15] However, even under the high vacuum conditions in the electron microscope, 2D materials are often covered with some amount of amorphous carbon surface residue arising from the organic solvents and polymers used in the processing, and/or by impurity atmospheric adsorbates. Importantly, if a nanopore is completely blocked, it is no longer useful and if a nanopore is only partially blocked this will reduce the nanopore size giving rise to a different behaviour when used as a separation membrane. Therefore, the ability to image both low atomic number elements such as carbon, as well as high atomic number elements such as Mo or W in TMDs is essential for future nanopore design in TMD materials.

ADF-STEM has been used extensively to discriminate metal and chalcogen atom columns and to provide structure details of S vacancies and edge terminations in 2D TMDs. However, it is challenging to simultaneously image light atoms in the presence of heavy ones using this geometry. BF phase contrast imaging is sensitive

to the presence of light atoms, but the intensity is strongly dependent on specimen thickness and inner electrostatic potential.

Collecting far field electron diffraction patterns from a set of STEM probe positions using a fast 2D pixelated direct electron detector allows the recording of datasets suitable for both ptychographic and ADF-STEM reconstruction simultaneously. This requires the pixelated detector to have fast-readout and high dynamic range with single electron sensitivity.[16,17] Fig. 6.1a shows the geometry of a typical 4D-STEM data acquisition, in which the pixelated detector operates in conjunction with an ADF detector. The benefit of capturing the full CBED pattern is that it allows various post-acquisition reconstructions (fig. 6.1b-g), including BF-, ABF-, ADF-STEM, electric field maps, phase retrieval (ptychography), DPC, and iDPC. In turn, this wide variety of signals that can be synthesised enables the construction of interpretable elemental maps which are essential for differentiating sublattice sites, vacancies and dopants, and the local projected electric field, giving insight into the local electrostatic properties.[18-21] Phase contrast images, which have been used extensively in both optical and transmission electron microscopy, represent the local projected potential. Ptychographic phase reconstruction has been successfully applied using various algorithms including WDD[22-24] and ePIE.[25] In this chapter, I demonstrate the use of 4D-STEM for imaging light elements in form of carbon surface adatoms and monolayer films within TMDs, providing the possibility for real-time imaging of defect evolution based on DPC.

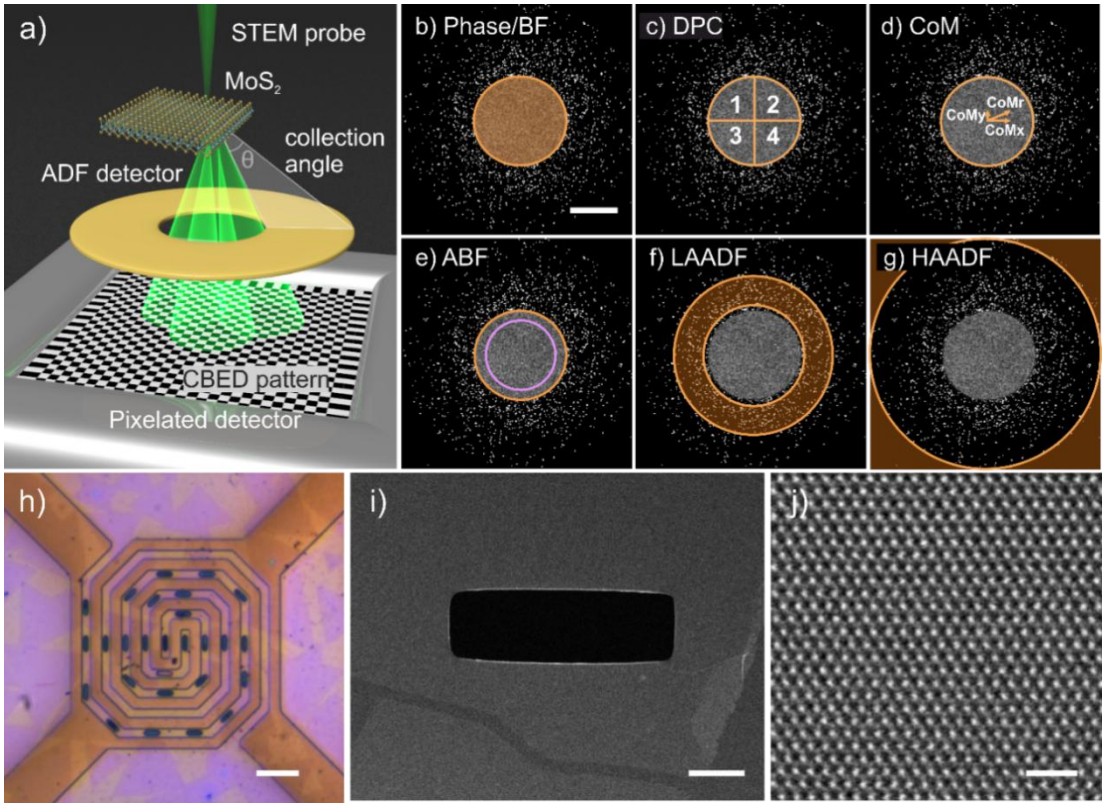


Figure 6.1. (a) Schematic of 4D-STEM data acquisition. (b-g) Various reconstructions from a 4D data set, superimposed on an ED pattern, where the circles indicate virtual detector inner and outer collection angles and shadowed regions indicate summed areas. (h) Optical image of CVD-grown MoS_2 (purple triangular-shaped domains) on an in-situ heating chip. Scale bar indicates 40 μm. (i) ADF-STEM image of a MoS_2 crystal covering a slit on a Si_3N_4 support film. Scale bar indicates 1 μm. (j) ADF-STEM image of a monolayer MoS_2 lattice. Scale bar indicates 1 nm.

6.2 Results and discussion

Surface carbon residues are typically found on all 2D materials and can further increase locally during STEM imaging.[30] This carbon-based contamination is either due to residue from the transfer process (organic solvent) or from the microscope vacuum. There is some evidence from previous studies to suggest that the latter is important, where it was shown that surface carbon redeposits on samples subject to heating and subsequent cooling in the TEM vacuum. [31,32] Fig. 6.2a shows a typical image of MoS_2 with monolayer regions of surface carbon adsorbate. Two nanopores have been drilled in this region using the STEM probe. However, it is hard to detect if the amorphous carbon covers these nanopores or if they are open. For pores that are partially covered (fig. 6.2b, c), the amorphous carbon within the pores shows slightly higher intensity than the vacuum. In addition, multi-frame averaging helps to resolve the carbon lattice because of the improved signal to noise (fig. 6.2d, e). Fig. 6.2f shows a schematic illustration of a nanopore in MoS_2 covered with carbon monolayer.

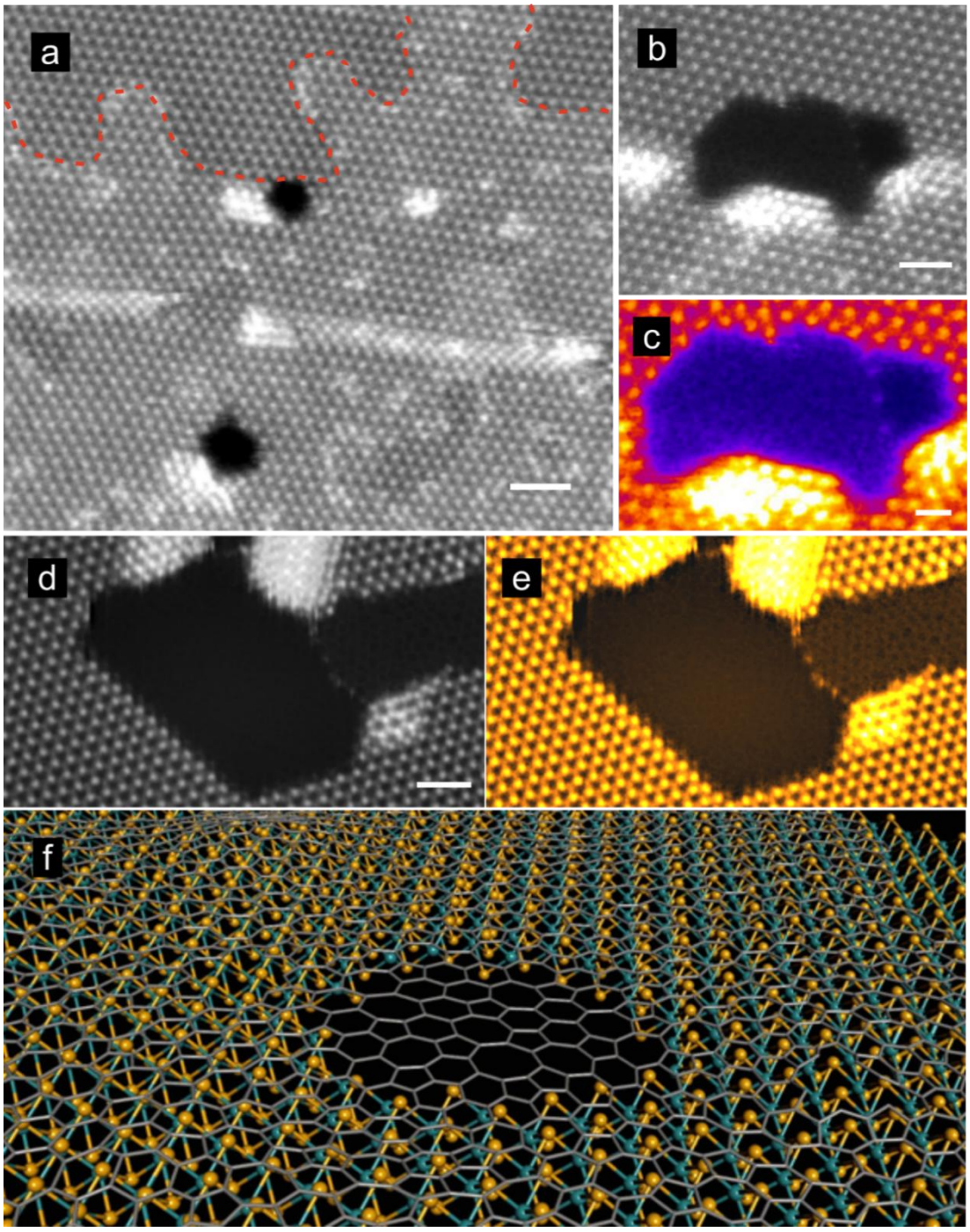


Figure 6.2. Low-magnification ADF-STEM images of MoS_2 with carbon contamination. (a) Drilled nanopores surrounded by amorphous carbon contamination. To aid visualization, regions with carbon (higher contrast) are delineated from clean regions by red dotted lines. The convergence semi-angle used was 31.5 mrad, camera length 16 cm, detector collection angle 49.5-198 mrad, probe size is estimated to be 1.9 Å. (b) Nanopore partially covered with a carbon layer and c) magnified view of this pore in false colour showing internal atoms.

(d) Multi-frame ADF-STEM images showing a nanopore partially covered with a carbon layer and (e) the same region displayed with false colour, for visualisation of the carbon lattice. (f) Schematic 3D view of surface carbon covering a nanopore in MoS_2. For panel a), b), d) and e), the scale bar indicates 1 nm, for panel c), the scale bar indicates 0.5 nm.

Fig. 6.3 shows reconstructions from 4D data sets of MoS_2 and WS_2 with nanopores (reconstruction details are given in the supporting information). In the reconstructed LAADF-STEM images (fig. 6.3a, e), both lattices are clearly resolved with atomic sites in bright contrast and regions inside the holes as dark contrast. Reconstructed BF images (fig. 6.3b, f) show reversed contrast, but provide similar information. However, in the reconstructed ABF image, regular features are observed inside the MoS_2 hole (fig. 6.3b), which are more pronounced in the reconstructed phase (fig. 6.3d). In contrast, the WS_2 hole (fig. 6.3h) is apparently clean.

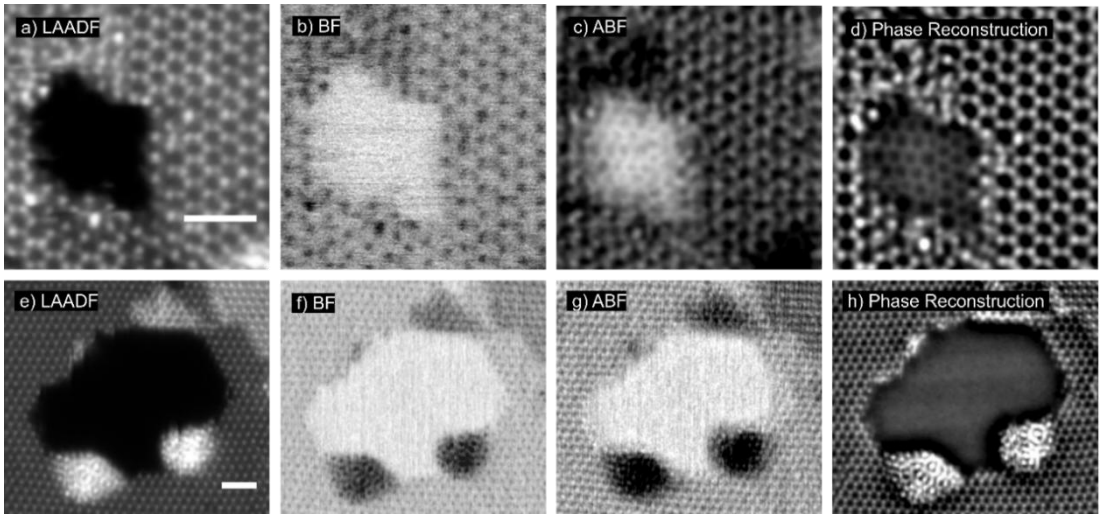


Figure 6.3. 4D-STEM reconstructed data recorded at 700°C from MoS_2 (a-d) and WS_2 (e-h) both with a hole. For MoS_2, the convergence semi-angle used was 39.1 mrad, camera length 6 cm, probe size is estimated to be 1.5 Å, (a) LAADF-STEM image reconstructed using a 40-60 mrad collection angle, (b) BF using a 0-39 mrad collection angle (c) ABF using a 27-39 mrad collection angle. For WS_2, a convergence of 30.6 mrad was used, camera length 6 cm, probe size is estimated to be 1.9 Å, (e) LAADF-STEM image reconstructed using a 40-60 mrad collection angle, (f) BF using a 0-30 mrad collection angle, (g) ABF using a 30

mrad collection angle. Scale bar indicates 1 nm and applies to (a-c) and (d-f) respectively.

The structure visible within the MoS_2 nanopore is due to residual surface carbon and is confirmed by measuring the bond length (0.15nm) using the MoS_2 lattice as a reference (fig. 6.4a), which gives a value close to that for a C-C bond in a hexagonal carbon ring (0.14 nm). A similar defective carbon monolayer lattice has also been observed in a conventional aberration corrected phase contrast TEM image (fig. 6.4g). Multislice simulations of the reconstructed phase (fig. 6.4b)[33,34] qualitatively agree with the experimental data (fig. 6.4a). The ABF reconstruction also shows sensitivity to light elements, but it fails to reach sufficient resolution low magnification (fig. D1b).[35] Simulations of the BF, ABF and div(DPC) are shown in fig. 6.4d-f. The div(DPC) simulation, fig. 6.4f, shows simultaneous imaging of both the carbon lattice and the MoS_2, with phase values qualitatively similar to those in the reconstructed phase shown in fig. 6.4b.

The presence of carbon lattice has been observed repetitively during imaging (fig. D2), and the divergence of the CoM shift (div(CoM)), or div(DPC) is also capable of resolving the carbon lattice comparable to the reconstructed phase (fig. 6.5). The CoM shifts obtained by DPC and pixelated detector share some similarities as they both quantify the distribution of the electrons inside the BFD and can be directly related to the local electromagnetic field,[36] though CoM shift from pixelated detector should be more sensitive to the electron distribution in the detector, as explained in section 2.3.4.Thus, both div(DPC) and div(CoM) are linearly related to the local charge density through Poisson's equation, [21] whereas the reconstructed phase is related to the projected electrostatic potential and is an indication of local charge distribution.

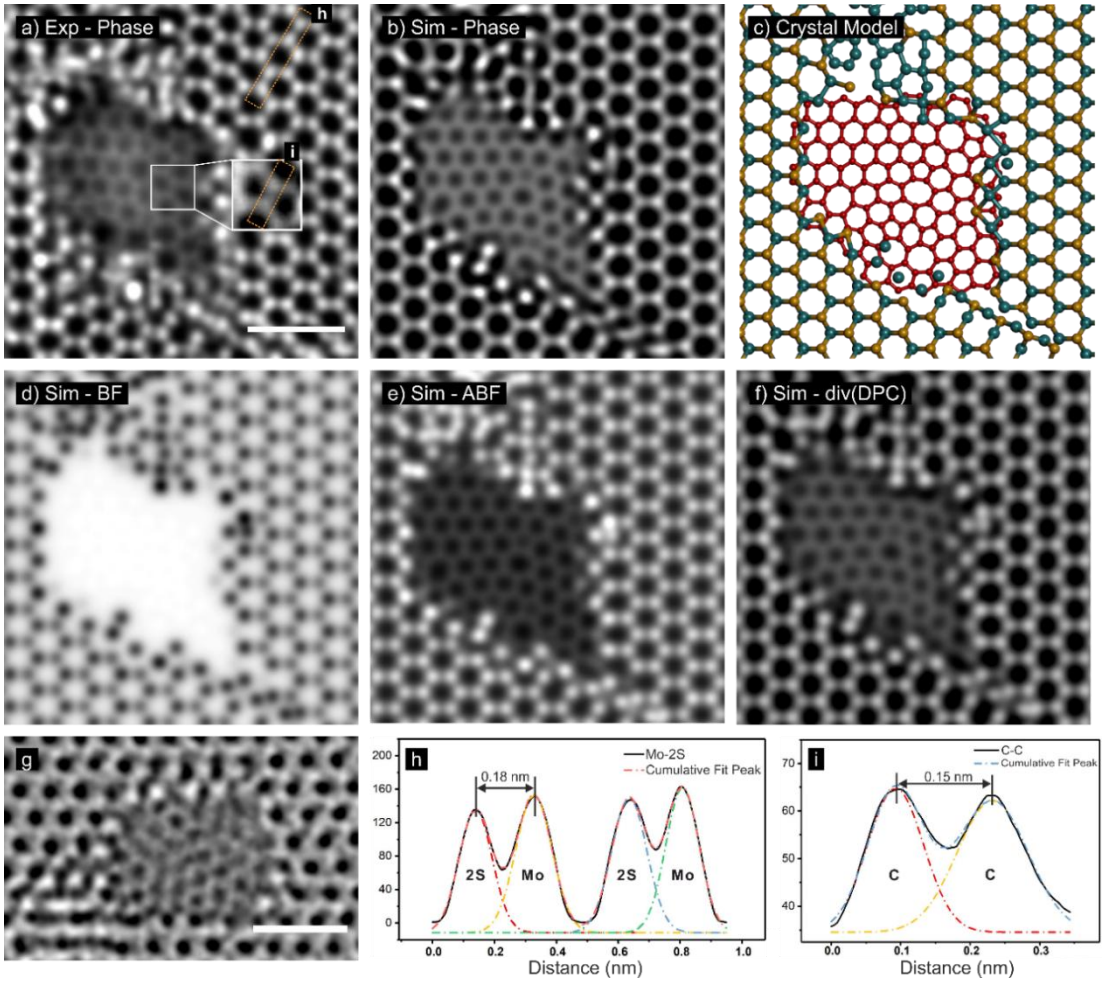


Figure 6.4. (a) Reconstructed Ptychographic phase from 4D-STEM data. (b) Multislice simulation of the reconstructed phase based on the atomic model in (c). (d)-(f) Multislice simulations of BF, ABF, and div(DPC) based on the atomic model in (c). (g) BF phase contrast TEM image of a nanopore in MoS_2 filled with a defective carbon monolayer. (h) Line profile of the intensity taken from the boxed region indicated in (a), fitted with Gaussian functions to locate the peak centres used to measure the Mo-2S distance. (i) Line profile taken from the boxed region indicated in (a) with the C-C distance measured. All the scale bars indicate 1 nm. Convergence semi-angle is 39.1 mrad, camera length 6 cm, probe size is estimated to be 1.5 Å.

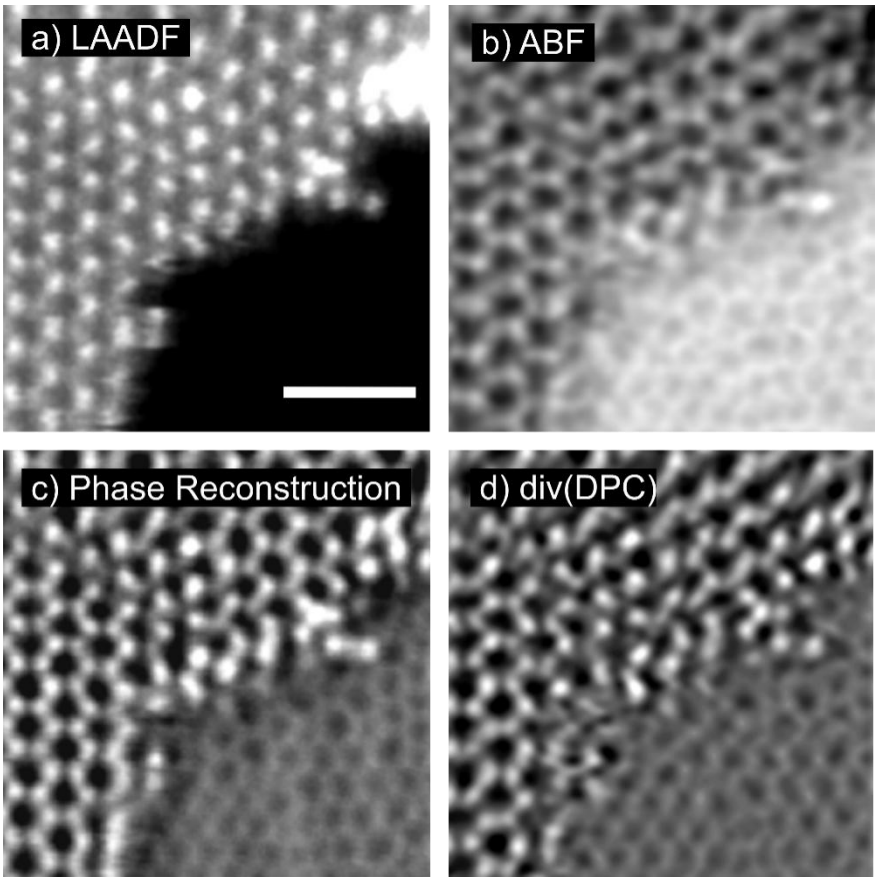


Figure 6.5. A nanopore in MoS_2 filled with a carbon layer reconstructed from 4D-STEM data. (a) LAADF-STEM image reconstructed using a 40-60 mrad collection angle, (b) ABF using a 27-39 mrad collection angle. (c) Ptychographic reconstruction of the phase. (d) Div(DPC). Scale bar indicates 1 nm and applies to (a-d). Convergence semi-angle is 39.1 mrad, camera length 6 cm, probe size is estimated to be 1.5 Å.

Next, I examine light atoms on the surface of TMDs. HAADF-STEM imaging shows contrast that is quantitative in Z, if the collection angle is sufficiently high. However, this makes the imaging of light atoms challenging, especially in the presence of heavy elements. To overcome this whilst maintaining high resolution, LAADF-STEM has been used extensively in detecting defect structures e.g., oxygen vacancies in $SrTiO_3$, Ce^{3+} in CeO_2, light dopants and vacancies with depth sensitivity in the presence of strain contrast.[37-41]

4D-STEM is ideal for exploring the angular dependence of ADF-STEM image contrast as capturing the whole ED pattern allows post-acquisition reconstruction. From fig. 6.6a, for monolayer MoS_2, an extra atom is located at a 2S site, most likely as a surface adatom or dopant and appears brighter in the reconstructed LAADF-STEM image than the adjacent Mo atom. However, the intensity at this site intensity drops significantly with increasing detector angular range (fig. D3 b-e), until it is not detected under HAADF conditions (fig. 6.6b). The presence of such an adatom is also not obvious in the reconstructed phase (fig. 6.6c), where the column shows only slightly higher contrast.

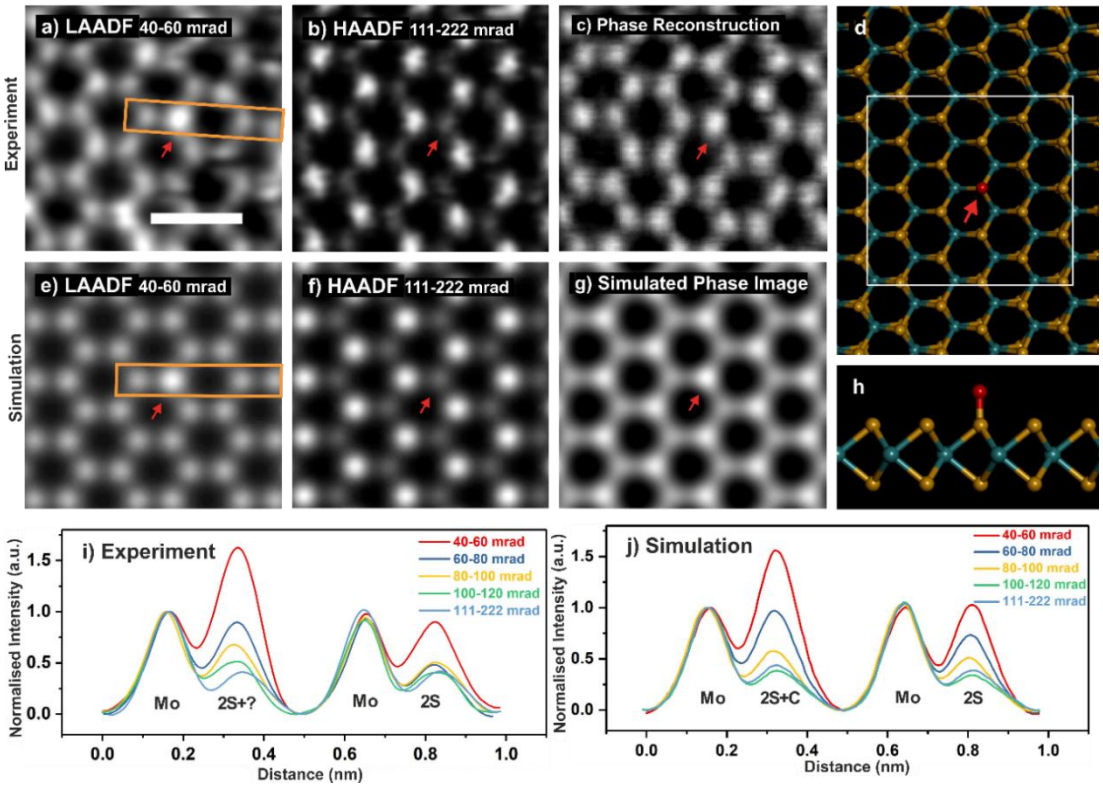


Figure 6.6. A surface adatom (indicated by red arrows) on 2S site in a MoS_2 lattice. (a) LAADF-STEM image reconstruction using a 40-60 mrad collection angle. (b) Simultaneous HAADF-STEM image. (c) Phase reconstruction (method in SI). (d) Crystal model of a C adatom on 2S site where the red arrow indicates the adatom position. (e) Simulated LAADF-STEM and f) HAADF-STEM images and g) phase contrast image based on the boxed regions in the crystal model in (d). (h) Side view of crystal model in (d). (i) Line profiles of the boxed region in (a) and corresponding regions in (b) and fig. D3b-d

(intensities were normalised to the peak intensity of the Mo atom). (j) Line profiles of the boxed region in the simulated ADF-STEM images in (e, f, and fig. D3h-j) (intensities were also normalised to the peak intensity of first Mo atom). (j) Side view of the model shown in (d). Scale bar indicates 0.5 nm and applies to (a-d). Convergence semi-angle is 39.1 mrad, camera length 6 cm, probe size is estimated to be 1.5 Å.

Other bright adatoms/dopants have been observed in LAADF-STEM image at both the 2S site (fig. 6.7a) and Mo site (fig. 6.8a). However, in these images the difference in contrast varies less as a function of increasing collection angle (fig. D4, D5), suggesting different adatom species to those shown in fig. 6.6. To understand this, I simulated images of structures with both light surface adatoms including C, N, and O, which are common contaminates inside the microscope column, and heavy surface adatoms. Fig. 6.6e, f and fig. D3g-l, show simulations of a C adatom sitting on top of a 2S site demonstrating good qualitative agreement with the experimental data, (fig. 6.6i, j), in which the site of the adatom adsorption exhibits lower contrast compared to the Mo atom under HAADF conditions, but higher contrast under LAADF conditions. For the second case where a O adatom is located on top of a Mo atom (fig. 6.7) the experimental and simulated data show that the HAADF-STEM contrast never drops below that due to a single Mo site, but under LAADF conditions the contrast increases significantly. Finally, for the third case where a heavy adatom sits on top of a heavy Mo atom, (fig. 6.8 and D5), the experimental and simulated data show that the contrast from the adatom site is always higher than that due to a single Mo atom, under both LAADF and HAADF conditions. Overall, these three cases show that it is possible to use 4D-STEM and the angular dependency of the LAADF/MAADF conditions to discriminate atomic columns with light-light, light-heavy and heavy-heavy adatom combinations.

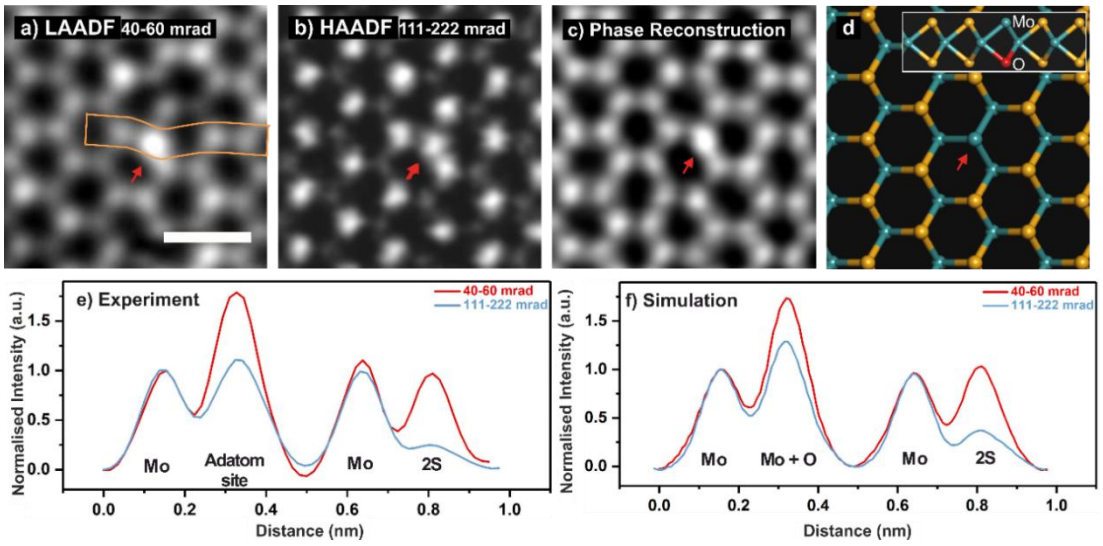


Figure 6.7. Surface adatom (indicated by red arrows) at a 2S site in MoS_2 showing a different intensity trend compared to fig. 6.7. (a) Reconstructed LAADF-STEM image and b) HAADF-STEM image with collection angles indicated. (c) Phase reconstruction. (d) Crystal model showing a Mo atom and a C atom at a 2S site with inset the side view of this model. (e) Line profiles from the boxed region in (a) and (b) (normalised to the peak intensity of a Mo atom). (f) Line profiles of boxed regions shown in simulated ADF-STEM images (fig. D4 f and j) (normalised to the peak intensity of a Mo atom) based on the crystal model in (d). Convergence semi-angle is 39.1 mrad, camera length 6 cm, probe size is estimated to be 1.5 Å. Scale bars indicates 0.5 nm and applies to (a-d).

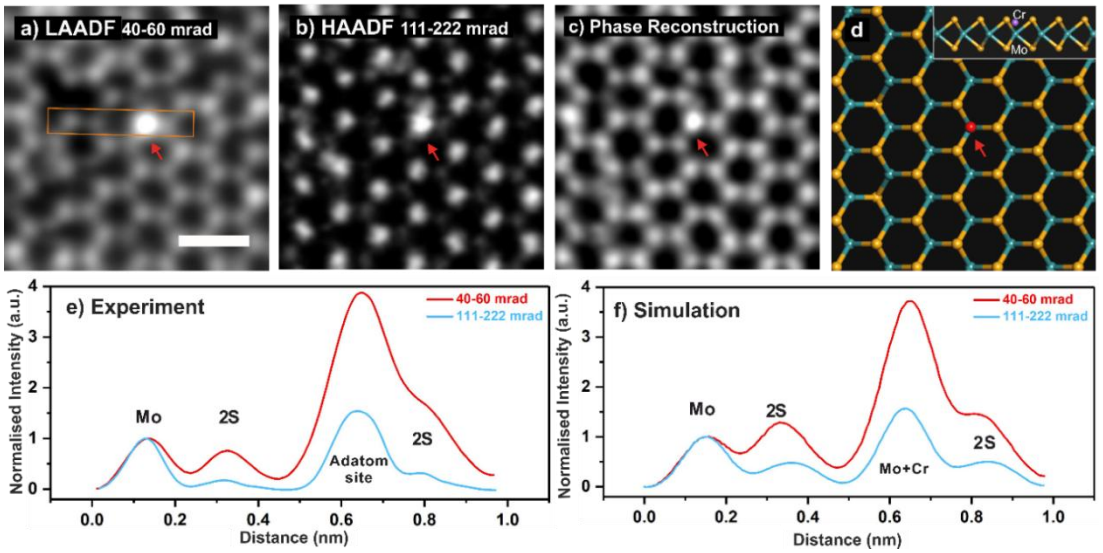


Figure 6.8. A surface adatom (indicated by red arrows) at a Mo site in MoS_2 showing different intensity behaviour comparing to the data in fig. 6.7. (a) Reconstructed LAADF-STEM image and b) HAADF-STEM image with collection angles indicated. (c) Phase reconstruction. (d) Crystal model showing an adatom at a Mo site with inset the side view of this model. (e) Line profiles of boxed region in (a) and (b) (normalised to the peak intensity of a Mo atom). (f) Line profiles of the boxed region shown in simulated ADF-STEM images (fig. D5 f and j) (normalised to the peak intensity of a Mo atom) based on crystal model in panel d. Convergence semi-angle is 39.1 mrad, camera length 6 cm, probe size is estimated to be 1.5 Å. Scale bar indicates 0.5 nm and applies to (a-d).

Finally, I explored the potential for the probe-convolved projected electric field ($|\boldsymbol{E}_{\perp \boldsymbol{PC}}|$) imaging around atoms reconstructed from 4D-STEM data to differentiate adatoms on TMDs. Prior work on 4D-STEM of MoS_2 and WS_2 has demonstrated $|\boldsymbol{E}_{\perp \boldsymbol{PC}}|$ imaging around single atoms and its sensitivity.[26,42] Fig. 6.9a shows the 2D projected $|\boldsymbol{E}_{\perp \boldsymbol{PC}}|$ map of the adatom, which is compared to DFT calculated $|\boldsymbol{E}_{\perp \boldsymbol{PC}}|$ maps based on a carbon and an oxygen adatom respectively (fig. 6.9b and 6.9c, DFT method described in SI). Although the DFT results provide an accurate prediction of the shape and magnitude of the $|\boldsymbol{E}_{\perp \boldsymbol{PC}}|$, they are unable to differentiate C and O adatoms, whilst on the basis of simulations, LAADF-STEM imaging can distinguish these (fig. D6). Furthermore, two adatoms as seen in fig. 6.7 and fig. 6.8 can be detected in ADF-STEM data (fig. 6.9e), and their respective low magnification electric field maps are shown in fig. 6.9h, where the adatom site appears brighter compared to the equivalent lattice sites. However, analysis of the $|\boldsymbol{E}_{\perp \boldsymbol{PC}}|$ signals for these two adatoms, (fig. 6.9 i, j) shows minimal difference and they cannot be differentiated. This indicates that whilst $|\boldsymbol{E}_{\perp \boldsymbol{PC}}|$ can provide sufficient contrast to identify the presence of adatoms, it is unable to differentiate columns with similar total atomic numbers arising from different combinations of light and heavy atoms.

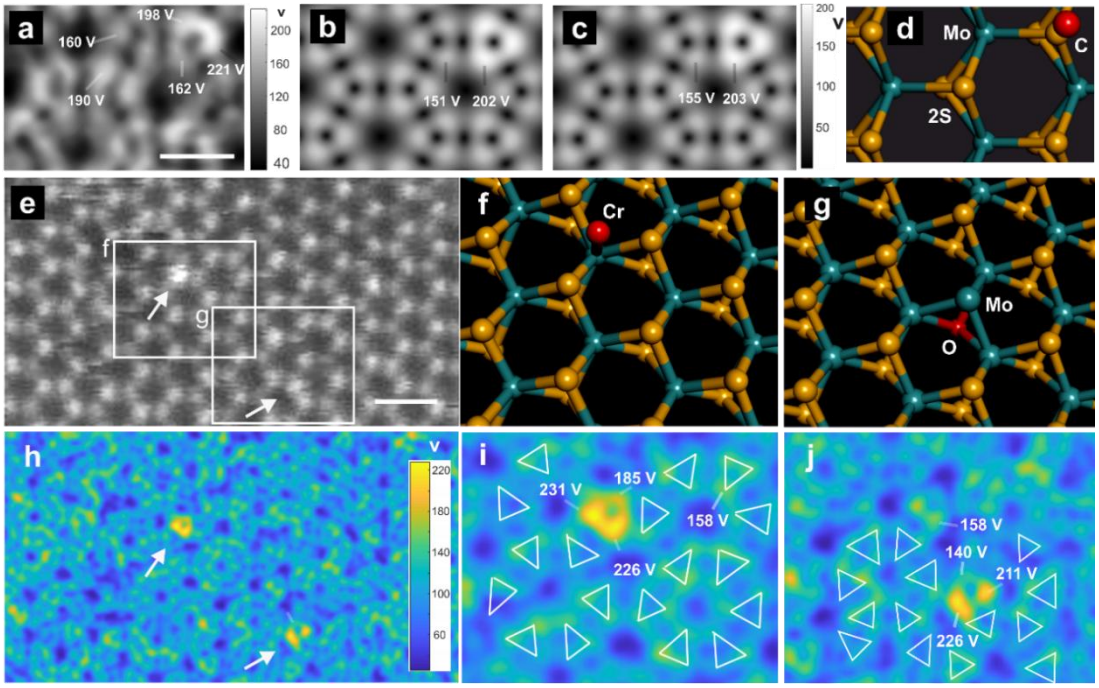


Figure 6.9. ADF-STEM images and electric field maps reconstructed from a 4D-STEM data set compared with DFT calculations. The probe-convolved projected electric field ($|\boldsymbol{E}_{\perp \boldsymbol{PC}}|$) maps were scaled to match the value from pristine area to that of DFT calculations. (a) $|\boldsymbol{E}_{\perp \boldsymbol{PC}}|$ map of a light adatoms at a 2S site compared with a DFT calculation of the electric field due to (b) carbon and (c) oxygen adatom on a 2S site, based on the model in (d). Scale bar indicates 0.25 nm and applies to panel a-d. (e) ADF-STEM image reconstructed with a 60-200 mrad collection angle. Scale bar indicates 0.5 nm and applies to (e and h). (f-g) Models of the boxed regions in (e). (h-j) $|\boldsymbol{E}_{\perp \boldsymbol{PC}}|$ maps corresponding to the marked region in (e) and to the models in f and g respectively, with false colour used to emphasize the higher $|\boldsymbol{E}_{\perp \boldsymbol{PC}}|$ intensities at adatom sites. The triangular shaped electric fields around each atom are indicated in (i) and (j). Convergence semi-angle is 39.1 mrad, camera length 6 cm, probe size is estimated to be 1.5 Å.

6.3 Conclusions

4D-STEM was used to reconstruct multiple imaging contrast methods for the detection and identification of single light and heavy atoms in 2D monolayer samples.

Using ptychographic phase reconstructions, combined with LAADF- and HAADF-STEM images, allows the detection of both C contaminants along with heavier Mo and W atoms. I have further showed how analysis of the angular dependent scattering can differentiate the chemical nature of surface adatom sites. This imaging approach is generally applicable to studies of organic-metal interfaces and molecules and provides a mechanism for mapping bonding between graphene and other inorganic 2D crystals containing heavy elements. In addition, the ability to detect carbon filling of nanopores will assist in future studies of edges and nanopores for applications in membranes and other devices.

References

1. Das, S., Chen, H. Y., Penumatcha, A. V., & Appenzeller, J., High performance multilayer MoS_2 transistors with scandium contacts, *Nano Letts.* **13**, 100–105 (2013).
2. Wang, H. *et al.* Integrated Circuits Based on Bilayer MoS_2 Transistors, *Nano Letts*. **12**, 4674–4680 (2012).
3. Lee, G. H. *et al.* Flexible and transparent MoS_2 field-effect transistors on hexagonal boron nitride-graphene heterostructures, *ACS Nano* **7**, 7931–7936 (2013).
4. Zhai, C. *et al.* Two dimensional MoS_2/graphene composites as promising supports for Pt electrocatalysts towards methanol oxidation, *J. Power Sources*, 275, 483–488 (2015).
5. Hou, D. *et al.* Pt nanoparticles/MoS_2 nanosheets/carbon fibers as efficient catalyst for the hydrogen evolution reaction, *Electrochim. Acta*, **166**, 26–31 (2015).
6. Wang, T. *et al.* Direct Detection of DNA below ppb Level Based on Thionin-Functionalized Layered MoS_2 Electrochemical Sensors, *Anal. Chem.* **86**, 12064–12069 (2014).
7. Heiranian, M., Farimani, A. B., & Aluru, N. R. Water desalination with a single-layer MoS_2 nanopore, *Nat. Commun.* **6**, 1–6 (2015).
8. Schneider, G. F. *et al.* DNA translocation through graphene nanopores, *Nano Letts.* **10**, 3163–3167 (2010).
9. Feng, J. *et al.* Electrochemical reaction in single layer MoS_2: Nanopores opened atom by atom, *Nano Letts*. **15**, 3431–3438 (2015).
10. Surwade, S. P. *et al.* Water desalination using nanoporous single-layer graphene, *Nat. Nanotechnol.* **10**, 459–464 (2015).
11. O'Hern, S. C. *et al.* Selective ionic transport through tunable subnanometer pores in single-layer graphene membranes, *Nano Letts.* **14**, 1234–1241 (2014).
12. Boutilier, M. S. H. *et al.* Molecular Sieving Across Centimeter-Scale Single-Layer Nanoporous Graphene Membranes, *ACS Nano*, **11**, 5726–5736 (2017).
13. Song, B. *et al.* Atomic-Scale Electron-Beam Sculpting of Near-Defect-Free Graphene Nanostructures, *Nano Letts.* **11**, 2247–2250 (2011).
14. Robertson, A. W. *et al.* Atomic Structure of Graphene Subnanometer Pores, *ACS Nano* **9**, 11599–11607 (2015).
15. Wang, S. *et al.* Atomic structure and formation mechanism of sub-nanometer pores in 2D monolayer MoS_2, *Nanoscale* **9**, 6417–6426 (2017).
16. Krajnak, M., McGrouther, D., Maneuski, D., O'Shea, V., & McVitie, S. Pixelated detectors and improved efficiency for magnetic imaging in STEM differential phase contrast, *Ultramicroscopy* **165**, 42–50 (2016).
17. Jiang, Y. *et al.* Electron ptychography of 2D materials to deep sub-Angström

resolution, *Nature* **559**, 343–349 (2018).
18. Krivanek, O.L. *et al.* Atom-by-atom structural and chemical analysis by annular dark-field electron microscopy, *Nature* **464**, 571–574 (2010).
19. Close, R., Chen, Z., Shibata, N., & Findlay, S.D. Towards quantitative, atomic-resolution reconstruction of the electrostatic potential via differential phase contrast using electrons, *Ultramicroscopy* **159**, 124–137 (2015).
20. Lazić, I., Bosch, E.G.T., & Lazar, S. Phase contrast STEM for thin samples: Integrated differential phase contrast, *Ultramicroscopy* **160**, 265–280 (2016).
21. Müller-Caspary, K. *et al.* Measurement of atomic electric fields and charge densities from average momentum transfers using scanning transmission electron microscopy, *Ultramicroscopy* **178**, 62–80 (2017).
22. Bates, R.H.T. & Rodenburg, J.M. Sub-Angström transmission microscopy: A fourier transform algorithm for microdiffraction plane intensity information, *Ultramicroscopy* **31**, 303–307 (1989).
23. Rodenburg, J.M. & Bates, R.H.T. The theory of super-resolution electron microscopy via Wigner-distribution deconvolution, *Philos. Trans. R. Soc. London Ser. A Phys. Eng. Sci* **339**, 521–553 (1992).
24. Yang, H. *et al.* Simultaneous atomic-resolution electron ptychography and Z-contrast imaging of light and heavy elements in complex nanostructures, *Nat. Commun*. **7**, 12532 (2016).
25. D'Alfonso, A.J. et al. Deterministic electron ptychography at atomic resolution, *Phys. Rev. B - Condens. Matter Mater. Phys.* **89**, 064101 (2014).
26. Shibata, N. *et al*. Electric field imaging of single atoms, *Nat. Commun*. **8**, 15631 (2017).
27. Müller, K. *et al.* Atomic electric fields revealed by a quantum mechanical approach to electron picodiffraction, *Nat. Commun.* **5**, 5653 (2014).
28. Hachtel, J. A., Idrobo, J. C., & Chi, M, Sub-Ångstrom electric field measurements on a universal detector in a scanning transmission electron microscope, *Adv. Struct. Chem. Imag.* **4**, 10 (2018).
29. Ishikawa, R. *et al.* Direct electric field imaging of graphene defects, *Nat. Commun*. **9**, 3878 (2018).
30. Griffiths, A.J.V. & Walther, T. Quantification of carbon contamination under electron beam irradiation in a scanning transmission electron microscope and its suppression by plasma cleaning, *J. Phys. Conf. Ser.* **241**, 012017 (2010).
31. Ennos, A.E. The origin of specimen contamination in the electron microscope, *Br. J. Appl. Phys.* **4**, 101–106 (1953).
32. Ennos, A. E. The sources of electron-induced contamination in kinetic vacuum systems. *Br. J. Appl. Phys.* **5**, 27–31 (1954).
33. Cowley, J.M. & Moodie, A.F. The scattering of electrons by atoms and crystals. I. A new theoretical approach, *Acta Crystallogr.* **10**, 609–619 (1957).
34. Goodman, P. & Moodie, A.F. Numerical evaluations of N -beam wave functions in electron scattering by the multi-slice method, *Acta Crystallogr. Sect. A.* **30**, 280–290 (1974).

35. Ishikawa, R. *et al.* Direct imaging of hydrogen-atom columns in a crystal by annular bright-field electron microscopy, *Nat. Mater.* **10**, 278–281 (2011)
36. Shibata, N. *et al.* Direct Visualization of Local Electromagnetic Field Structures by Scanning Transmission Electron Microscopy, *Acc. Chem. Res.* **50**, 1502−1512 (2017).
37. Muller, D.A., Nakagawa, N., Ohtomo, A., Grazul, J.L., & Hwang, H.Y. Atomic-scale imaging of nanoengineered oxygen vacancy profiles in $SrTiO_3$, *Nature* **430**, 657–661 (2004).
38. Johnston-Peck, A.C. *et al.* Oxidation-state sensitive imaging of cerium dioxide by atomic-resolution low-angle annular dark field scanning transmission electron microscopy, *Ultramicroscopy* **162**, 52–60 (2016).
39. Johnson, J.M., Im, S., Windl, W., & Hwang, J. Three-dimensional imaging of individual point defects using selective detection angles in annular dark field scanning transmission electron microscopy, *Ultramicroscopy* **172**, 17–29 (2017).
40. Yu, Z., Muller, D.A., & Silcox, J. Study of strain fields at a-Si/c-Si interface, *J. Appl. Phys.* **95**, 3362–3371 (2004).
41. Grillo, V. & Rossi, F. A new insight on crystalline strain and defect features by STEM-ADF imaging, *J. Cryst. Growth* **318**, 1151–1156 (2011).
42. Fang, S. *et al.* Atomic electrostatic maps of 1D channels in 2D semiconductors using 4D scanning transmission electron microscopy, *Nat Commun.* **10**, 1–9 (2019).

Chapter 7 Conclusion and Outlook

7.1 Conclusion

2D materials have shown great potential in future electronics due to their superior properties while being atomic-thick. However, the intrinsic defects formed during synthesis and extrinsic defects formed during handling and characterization alter the properties, thus a full understanding on these atomic defect structures is essential for the application of 2D materials. Current characterization methods have their own advantages and drawbacks, and 4D-STEM is a novel technique that has been used in virtual detectors, orientation and strain mapping, DPC imaging, and ptychography that reach sub angstrom resolution, which are enabled by the recent instrumental development in high-speed pixelated detectors.

In this doctoral thesis, 4D-STEM was used to characterize prototype 2D materials with atomic resolution and quantitative electric field measurements. In chapter 4, I started by calculating the electric field and charge density in monolayer MoS_2 and WS_2 with sub-atomic resolution, then I studied the change in these electronic properties arise from crystal defective structures e.g., point and line sulphur vacancies, atomically flat zigzag edges, and MoS nanowire. Study on monolayer MoS_2 and WS_2 crystal provided basis for the subsequent quantitative study on simple point defects, one-dimensional TMD edge and nanowire, and twisted multilayer graphene. In the case of double sulphur vacancy, charge density map identified a substitutional atom at the vacancy site, while under my imaging conditions, I was not able to differentiate the filled and unfilled vacancies in ADF-STEM images, indicating the sensitivity and improved contrast of charge density map. Line sulphur vacancy was found to have a higher electron density, which is supported by DFT calculations, but further investigation with higher SNR is needed. The abnormal edge

effect in TMDs was discussed, and unlike previous study on graphene edge which shows that the edge enhancement is from unsaturated coordination on edge atoms, in MoS_2 the edge Mo atoms are saturated by adsorbed sulphur, as identified in reconstructed phase image. The electric field vector plot of edge Mo atoms showed that the positive field emitting from edge atoms is much higher compared to bulk atoms, which may be due to the partial coherence of the probe.

Chapter 5 is focusing on turbostratic graphene, where multilayer graphene system with different layer and twist angle are studied. I analysed the abnormal electric field associated with Moiré superlattices in the twisted graphene, assigned the Moiré pattern to the spots shown in FFT spectrum, and analysed the effect of twist angle. I found that, at large twist angles, the twisted graphene layers were decoupled and exhibited as individual layers, supported by simulation based on IAM, which showed good match with experimental results, indicating no detectable interlayer coupling was observed, or the fluctuation due to interlayer coupling was below the sensitivity of current 4D-STEM technique.

Chapter 6 discusses and compares the possible reconstruction modes from one set of 4D-STEM data. I showed how ABF, phase and div(DPC) can identify low and high atomic number atoms simultaneously with high resolution (e.g., amorphous carbon lattice in MoS_2 lattice hole), which cannot be achieved under regular ADF-STEM mode. I also showed how the post-reconstructed LAADF-STEM images can help locate and identify surface adsorbed atoms (adatoms), as each adatom shows different intensity profile as a function of LAADF-STEM reconstruction angular range (e.g., from 40-60 mrad, 60-80 mrad, 80-100 mrad, to 100-120 mrad). This finding showed a new pathway to atomic resolution adatom identification when other elemental mapping is not available.

To sum up, this thesis has explored the possibility for 4D-STEM technique to

characterize the change in the electronic properties and contrast of 2D materials due to defective structures. Novel

were found in various structures,
but certain drawbacks, e.g., long acquisition time,

7.2 Outlook

My doctoral research can be further investigated in two aspects. The first one is to improve 4D-STEM electric field mapping as a characterization technique, apparently it still has a few limitations before it can be a universal characterization method: (1) inability to realize real-time observation. The longer dwell time and the need for post-acquisition calculation makes it impossible to image the in-situ evolution of electric field map. (2) Resolution and sensitivity depend on the coherence of probe. The measured electric field is still inherently convolved with the probe intensity, which not only determines the spatial resolution of the electric field map, but may also introduce imaging artefact to the interpretation of the results. Approaches to deconvolve the probe has been developed and implementation of such approaches into real-time imaging process is underway. (3) Need for a reference CoM, preferably from the vacuum region. This limits the region of interest to near lattice edge, in order to record part of the vacuum region in the same data set. However, if the microscope is stable, this could be solved by using the same set of data of vacuum region for subsequent acquisition. (4) Accumulation of contamination. Long exposure time often leads to build-up of hydrocarbons especially when they preferentially attached to defective structure. They obscure the quantitative understanding of the defects thus in practice, pre-session cleaning process, beam shower, and *in situ* annealing are necessary, but they may not be applicable to materials that undergo phase change at elevated temperature. (5) The price of

pixelated detector hinders its widespread, and the DPC detector cannot replace all its functions.

The second one is to explore more complex structures and other materials. One limitation is that the conversion between momentum transfer and electric field only applies to thin samples of 1-2 nm, e.g., the thickness of bilayers MoS_2 is 1.28 nm. Another limitation of the 2D projected electric field map is that if the structure become complicated, e.g., multilayer, it becomes difficult to locate atoms or attribute change in electric field to certain defect structure. It would be possible to apply tomography or multiple acquisition at a focal series that may generate a 3D electric filed mapping, but still, accurate interpretation of defective structure requires DFT calculation and IAM simulation.

Appendix A

Supplementary Information for Chapter 3

In this chapter, a simplified excerpt of the Matlab code used to calculate the phase and to find the relative rotation between STEM scan coil and pixelated detector was presented, as it would be trivial to elaborate in section 3.5.3 and 3.5.5. The code first rotated the axes of CoM_x and CoM_y by a test angle, then integrated the CoM to obtain phase, which was then used to calculate the mean angular error. When changing the test angle, the error value changed, and when the smallest error is reached, the rough rotation angle was defined.

```
% Roate CoM matrices
comxr = comx.*cos(rt)-comy.*sin(rt);
comyr = comx.*sin(rt)+comy.*cos(rt);

% Make Fourier coordinates
[sy,sx] = size(comxr);
nx = sx;
ny = sy;

% Integrate in the Fourier space
if mod(nx,2) == 0
    kx = circshift((-nx/2:nx/2-1)/(nx),[0 -nx/2]);
    ky = circshift((-ny/2:ny/2-1)/(ny),[0 -ny/2]);
else
    kx = circshift(((1-nx)/2:(nx-1)/2)/nx,[0 (1-nx)/2]);
    ky = circshift(((1-ny)/2:(ny-1)/2)/ny,[0 (1-ny)/2]);
end

[kxa,kya] = meshgrid(kx,ky);
kp2 = kxa.^2+kya.^2;
kp2 = kp2 + 0.000001;% add 0.000001 to eliminate kp = 0
kxop = kxa./(4*pi*1i*kp2);
kyop = kya./(4*pi*1i*kp2);
icomx = (fft2(comx)).*kxop;
icomy = (fft2(comy)).*kyop;
icom = ifft2((icomx+icomy),'symmetric'); % integrated CoM
```

```
% Calculate mean angular error

for i = 10:1:sy-10
    for j = 10:1:sx-10
        phasegy(i,j) = (icom(i+1,j)-icom(i-1,j))/2;% phase gradient y
        phasegx(i,j) = (icom(i,j+1)-icom(i,j-1))/2;% phase gradient x
        phasegth(i,j) = atan2(phasegy,phasegx);% phase gradient theta
        phasegm(i,j) = sqrt(phasegx.^2+phasegy.^2);% phase gradient magnitude
        comth = atan2(comxr(i,j),comyr(i,j));% CoM theta
        diffth = abs(phasegth - comth);
    end
end
maerr = sum(diffth(:).*phasegm(:))/sum(phasegm(:))*180/pi;% mean angular error
in degree
```

Appendix B

Supplementary Information for Chapter 4

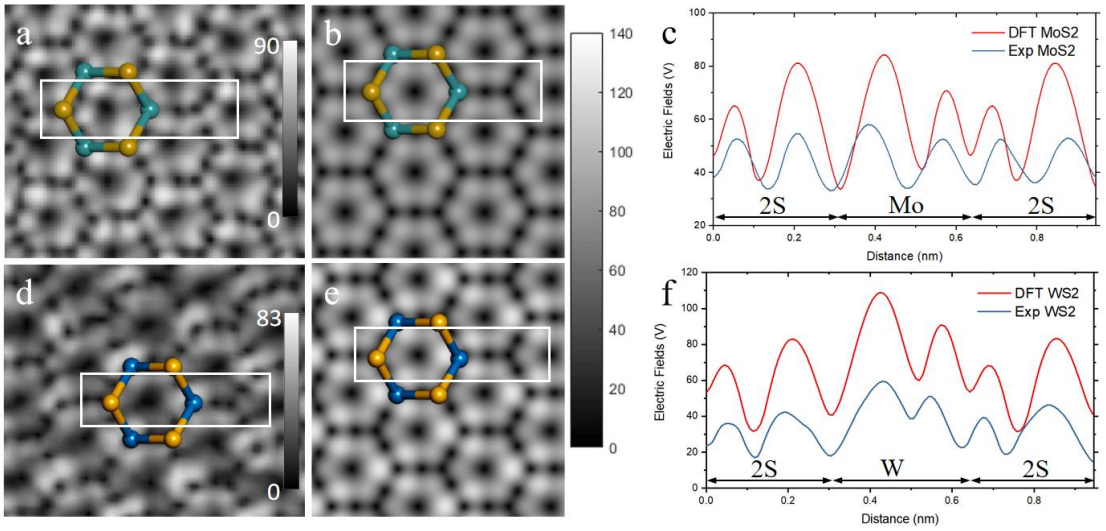


Figure B1. Comparison between experimentally measured $|\boldsymbol{E}_{\perp \boldsymbol{PC}}|$ and DFT calculated $|\boldsymbol{E}_{\perp \boldsymbol{PC}}|$. (a) Experimental and (b) DFT calculated $|\boldsymbol{E}_{\perp \boldsymbol{PC}}|$ of monolayer MoS_2, overlaid with crystal model of MoS_2 hexagon, where green ovals indicate Mo atoms, yellow ovals indicate 2S column. (c) Intensity line profile of boxed region in panel a and b, from left to right. (d) Experimental and (e) DFT calculated $|\boldsymbol{E}_{\perp \boldsymbol{PC}}|$ of monolayer WS_2, overlaid with crystal model of WS_2 hexagon, where blue ovals indicate W atoms, yellow ovals indicate 2S column. (c) Intensity line profile of boxed region in panel d and e, from left to right. Calibration bar unit is V.

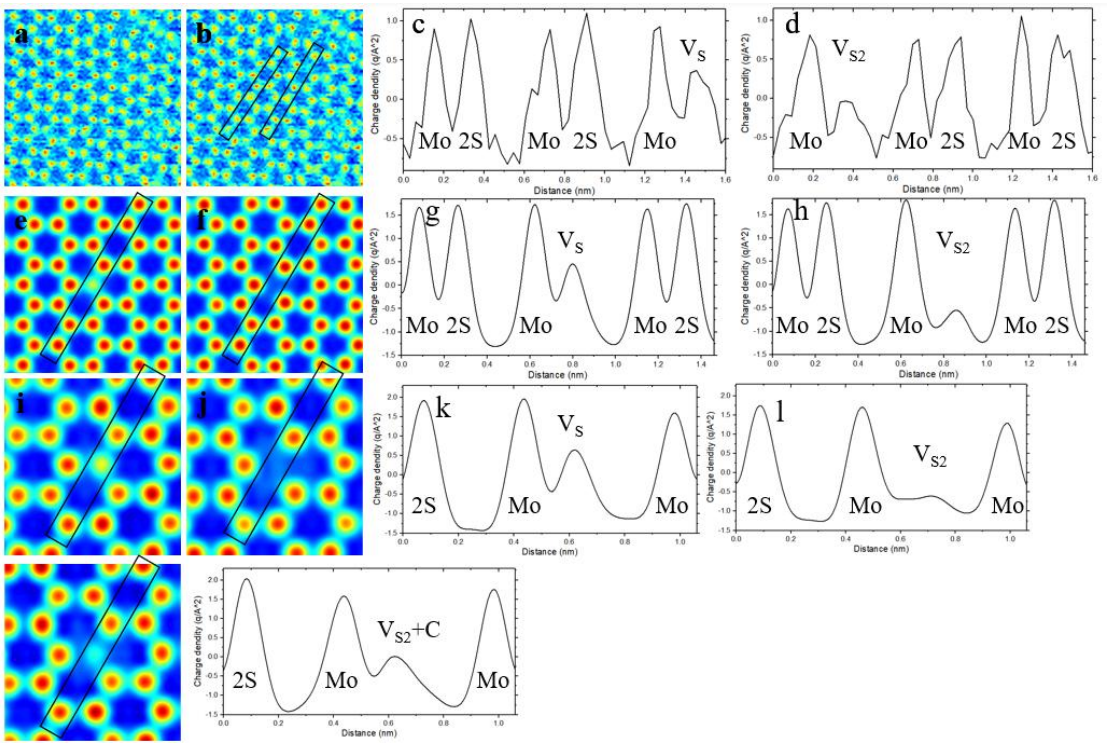


Figure B2. Charge density maps of V_S and V_{S2} in monolayer MoS_2 from experiment, DFT calculation, and IAM multislice simulation, and charge density maps of V_{S2} with C substitution from IAM multislice simulation. (a) Charge density map calculated from raw CoM_x and CoM_y data, where V_S and V_{S2} are circled out by solid and dashed ovals, respectively. (b) Same charge density map with rectangles indicating line profiles of V_S in panel c and V_{S2} in panel d. (e-f) DFT-calculated total charge density map of V_S and V_{S2} and corresponding line profiles in panel g and h, respectively. (i-j, n) IAM multislice simulation of charge density map of V_S, V_{S2}, and V_{S2} with C substitution (based on crystal model in panel m), rectangles indicate their corresponding line profiles in panel k, l, and o, respectively. All the line profiles are measured from the top of rectangle to the bottom.

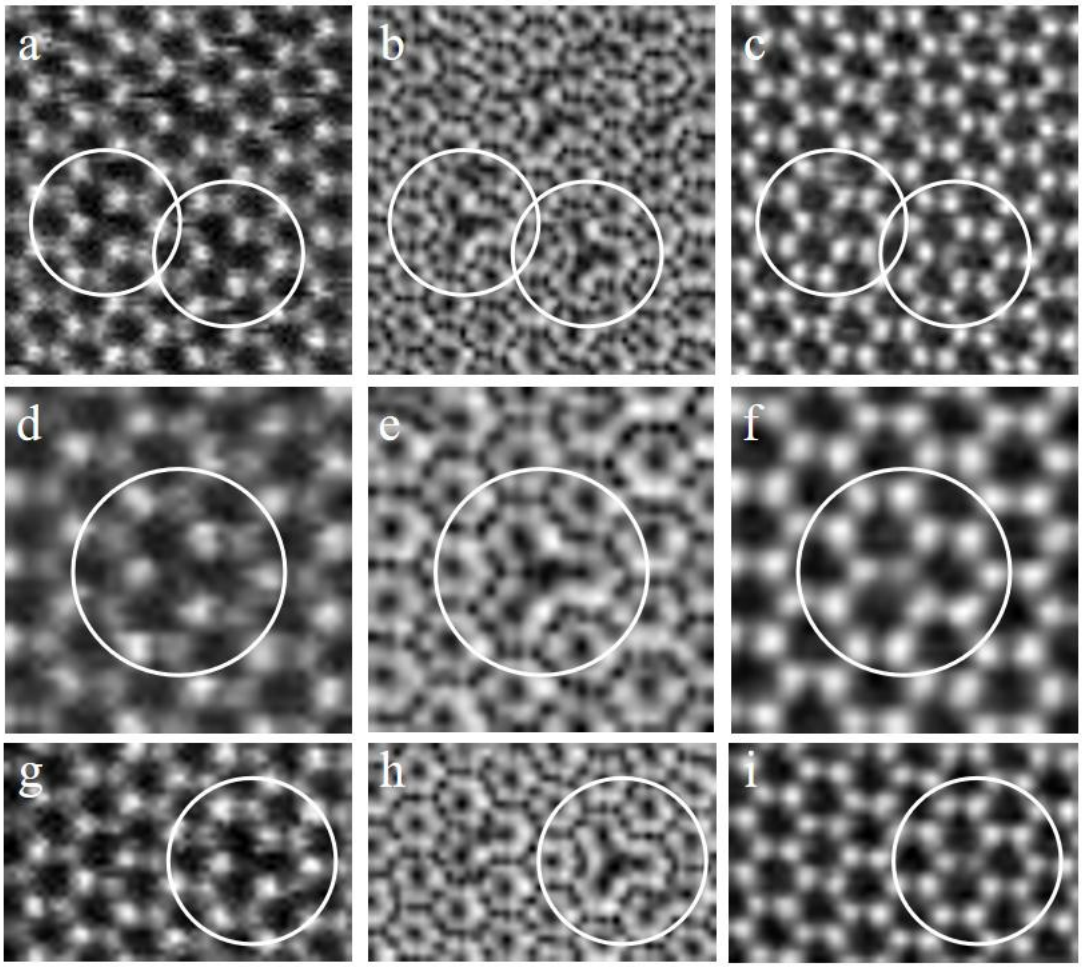


Figure B3. Repetitive observation of carbon substitution at V_{S2}. (a,d,g) Reconstructed LAADF-STEM images from different 4D-STEM data sets, reconstructed from 60-150 mrad. The structures similar to V_{S2} were circled out. (b,e,h) $|\boldsymbol{E}_{\perp \boldsymbol{PC}}|$ of the corresponding region in panel a, d, and g, respectively. (c,f,i) Charge density maps of the corresponding region in panel a,d,g, respectively, showing C substitution at V_{S2}.

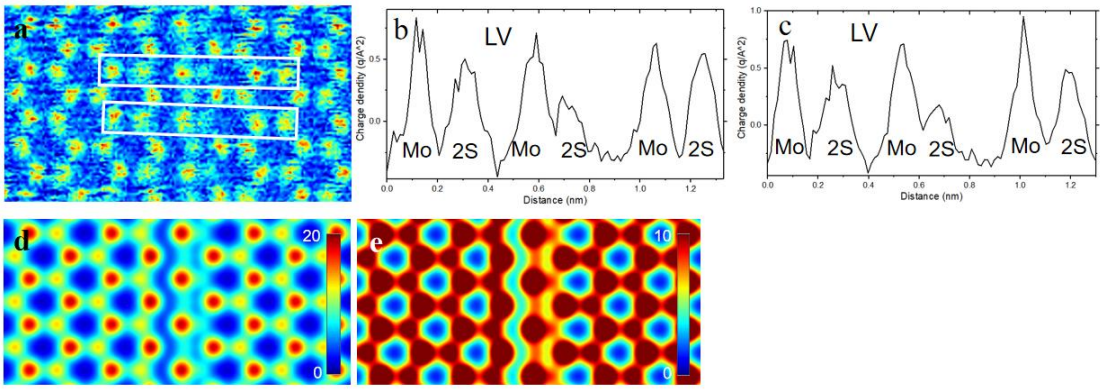


Figure B4. Charge density maps of line sulphur vacancy (LV) in monolayer MoS_2

from experiment and DFT calculation. (a) Charge density map calculated from raw CoM_x and CoM_y data, with rectangles indicating intensity line profiles across the LV in panel b and c, and a more negative charge density was found at LV in both line profiles. (d) DFT calculated electron density and (e) the same figure as panel d but saturated to emphasize the electron-rich region along LV. For charge density, calibration bar unit is $q \cdot A^{-2}$, for electron density, calibration bar unit is $e \cdot A^{-2}$. All the line profiles are measured from the left side of rectangle to the right side.

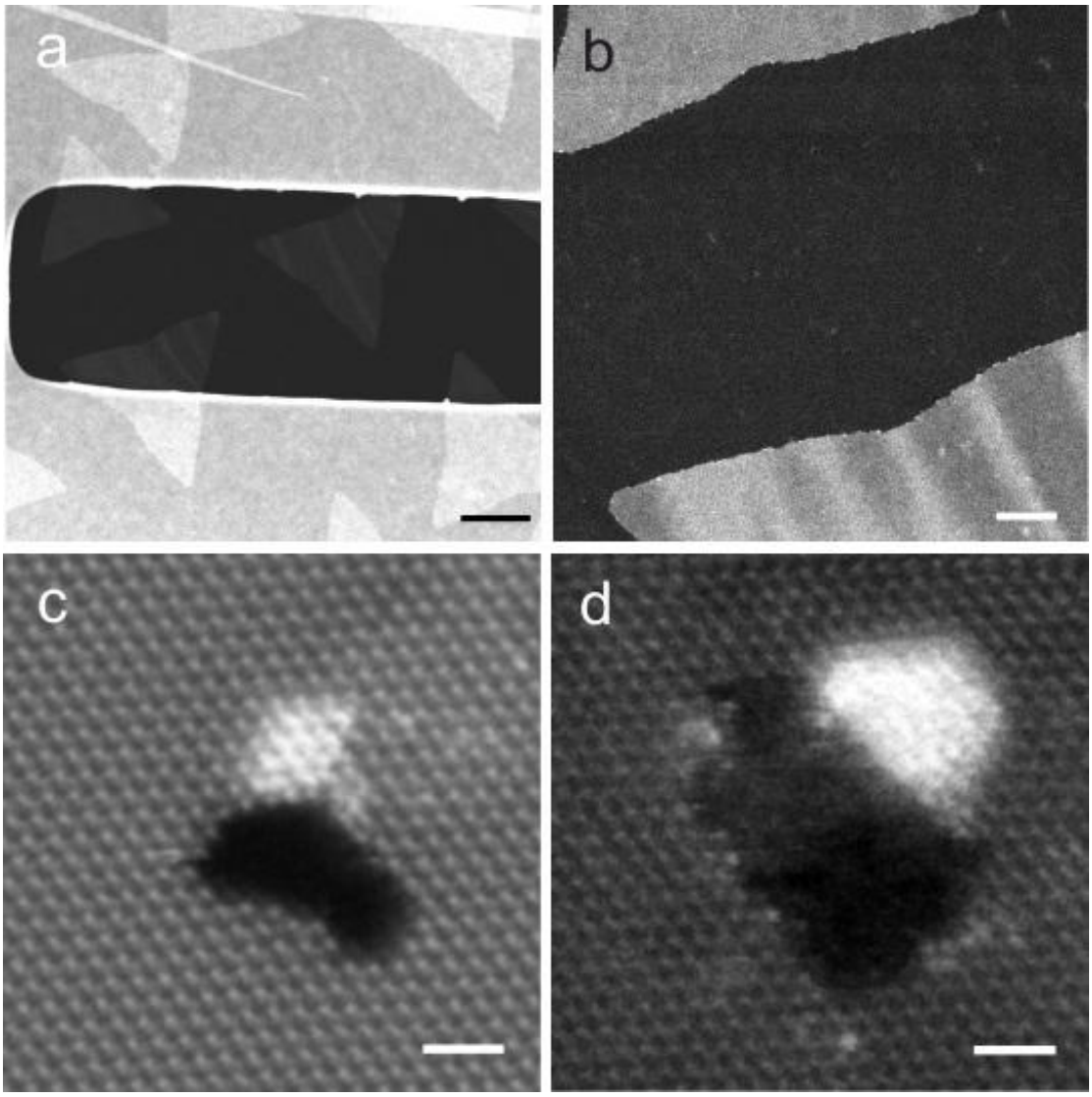


Figure B5. Low magnification (a, b) and high magnification (c, d) ADF-STEM images of MoS_2 transferred onto a heating chip. (a) MoS_2 monolayer and bilayer islands are visible through the slits. (b) Monolayer region between bilayer islands.

(c-d) ADF-STEM images acquired at room temperature. Without thermal annealing, the hole edges are rough and easily contaminated with carbon. Scale bars in panel a, b, c, and d indicate 200 nm, 50 nm, 1 nm, and 1 nm, respectively.

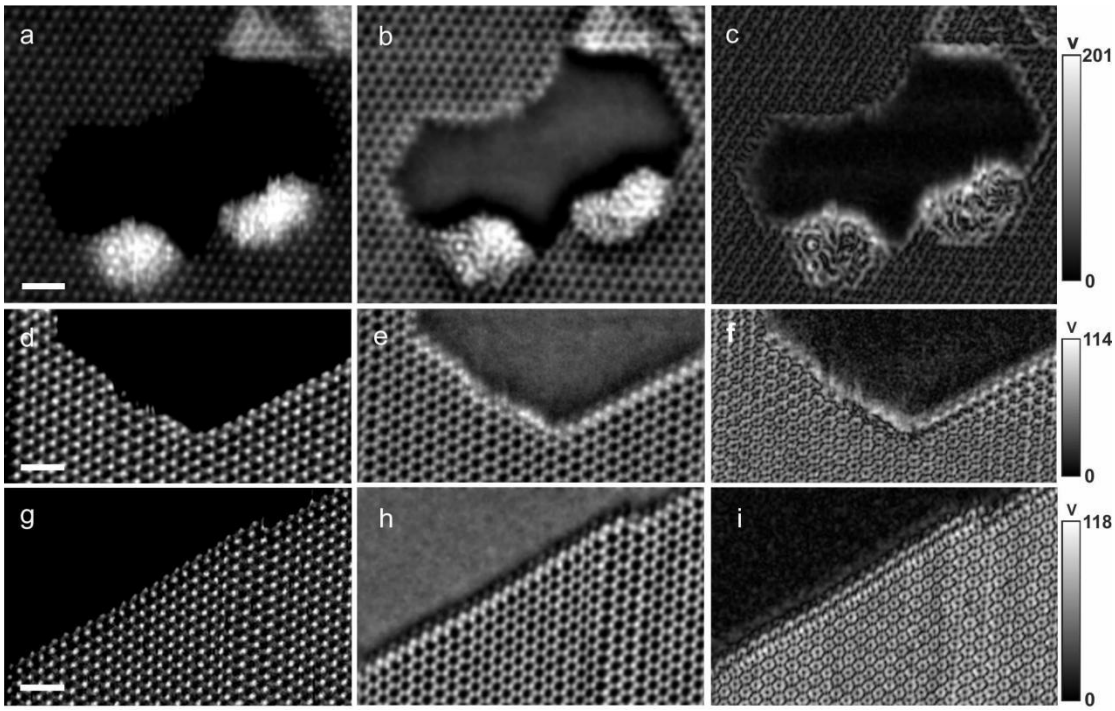


Figure B6. Multiple examples of reconstructed edge and edge enhancement. (a-c) are WS_2 examples, and (d-i) are MoS_2 examples. Panels a, d, and g are ADF-STEM images, b, e, and h are corresponding reconstructed phase, c, f, i are corresponding $|E_\perp|$ map. Panels a-c show a thermally created hole in WS_2, the hole edges are flat but not on a large scale. In contrast to MoS_2, not all edges are covered with additional S atoms. Panels d-f show an intersection between Mo zigzag edges and Mo-replaced zigzag edge; the former is not stable, so it was not captured clearly. Panels g-i show a Mo-replaced zigzag edge, the right side of the edge is starting to deteriorate. Scale bars in panel a indicates 1 nm and applies to panel b and c; scale bars in panel d indicates 1 nm and applies to panels e and f; scale bar in panel g indicates 1 nm and applies to panels h and i.

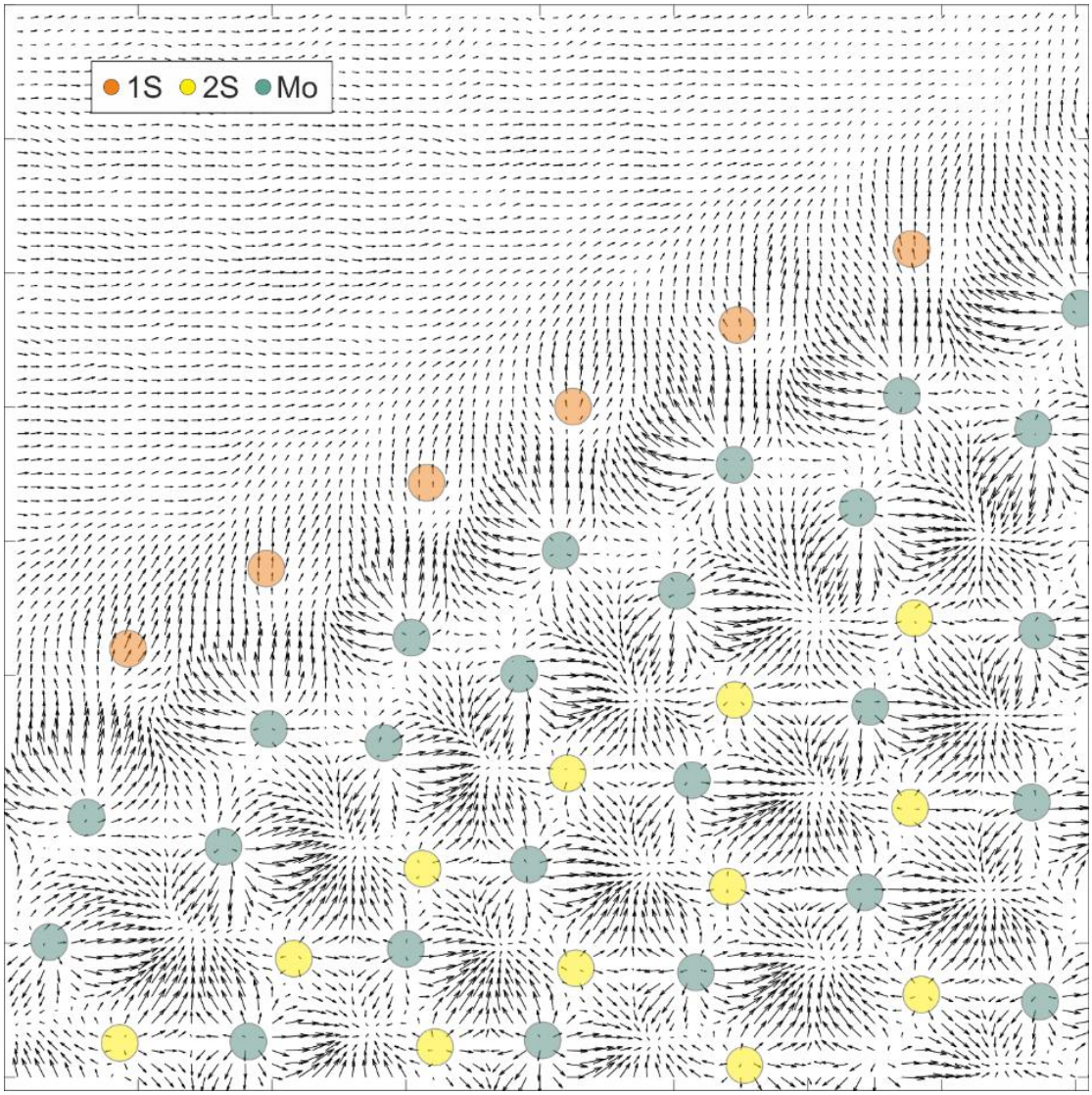


Figure B7. Vector map of electric field of a MoS_2 Mo-replaced zigzag edge. The centre of the outward field lines indicates the position of an atom. Note that the field around a bulk atom is three-fold symmetrical, while those around the edge Mo and S atoms are not.

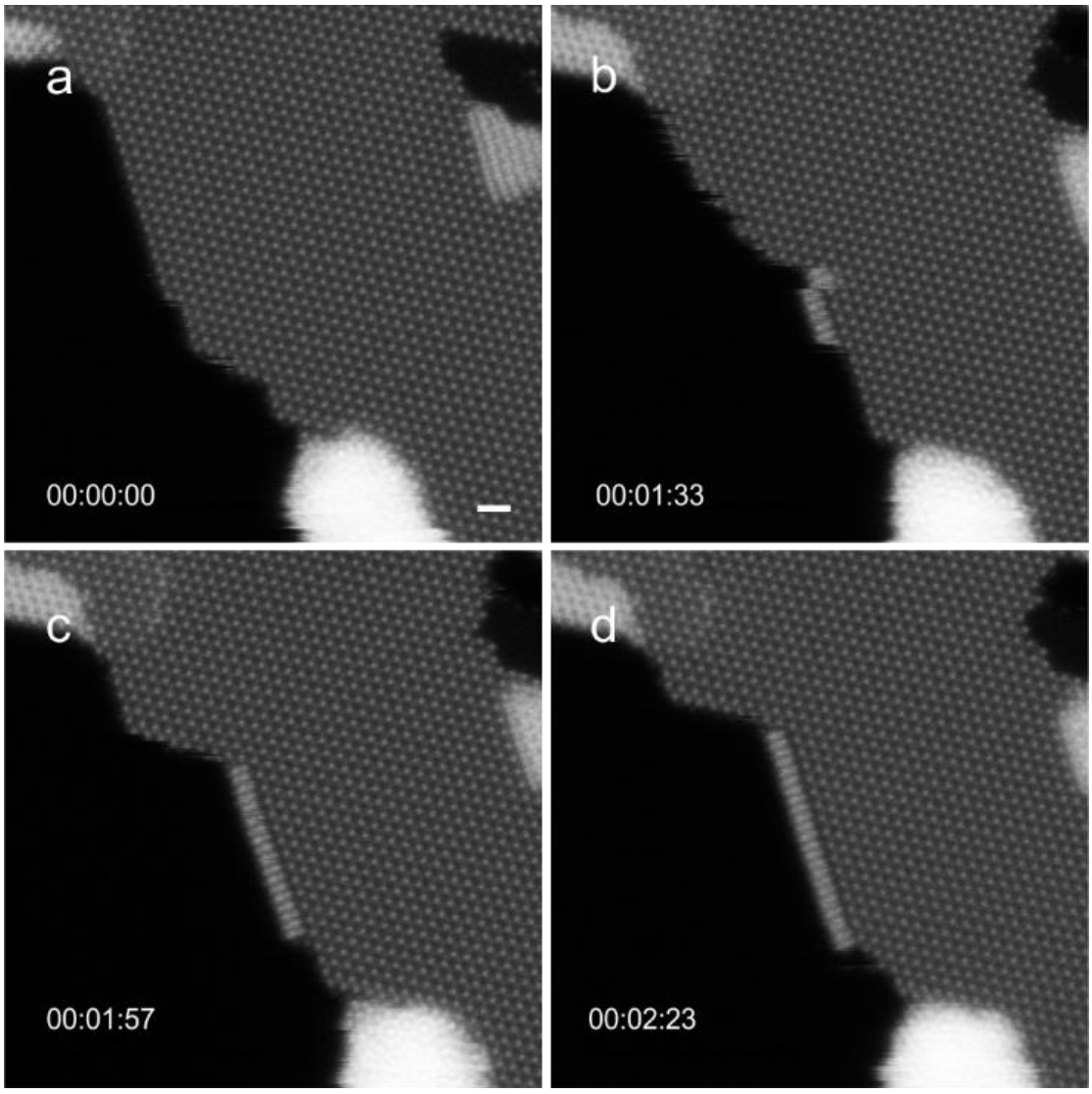


Figure B8. (a-d) Time series of ADF-STEM images showing the evolution of a nanowire from a MoS_2 lattice edge. Scale bar in panel a indicates 0.5 nm and applies to panels b-d.

Appendix C

Supplementary Information for Chapter 5

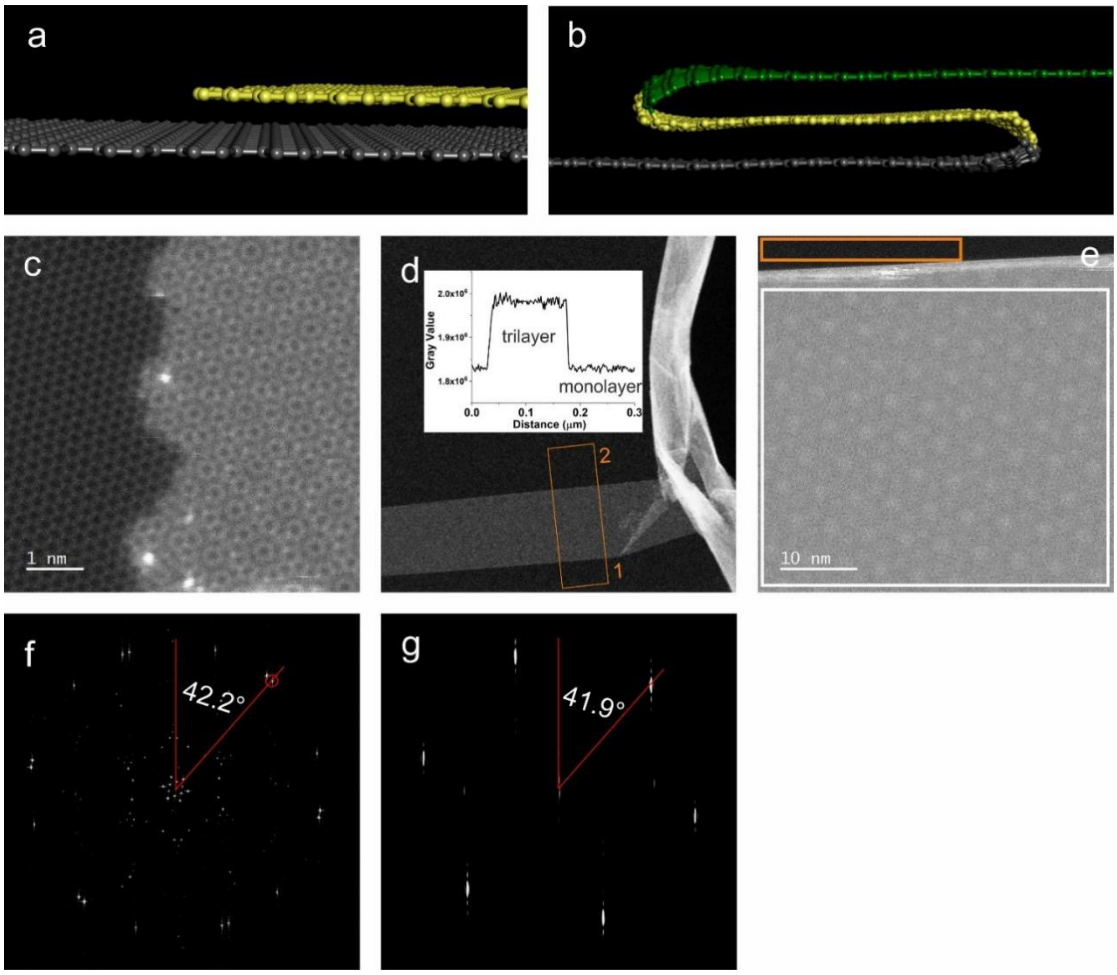


Figure C1. ADF-STEM image of (a) step edge of a TBG, (b) a backfolded monolayer graphene forming a trilayer region (inset shows the intensity line profile over boxed region from 1 to 2), and (c) enlarged backfolded trilayer, white box indicates the region used for FFT of solely trilayer region. (d-e) crystal models based on panel a and c respectively.

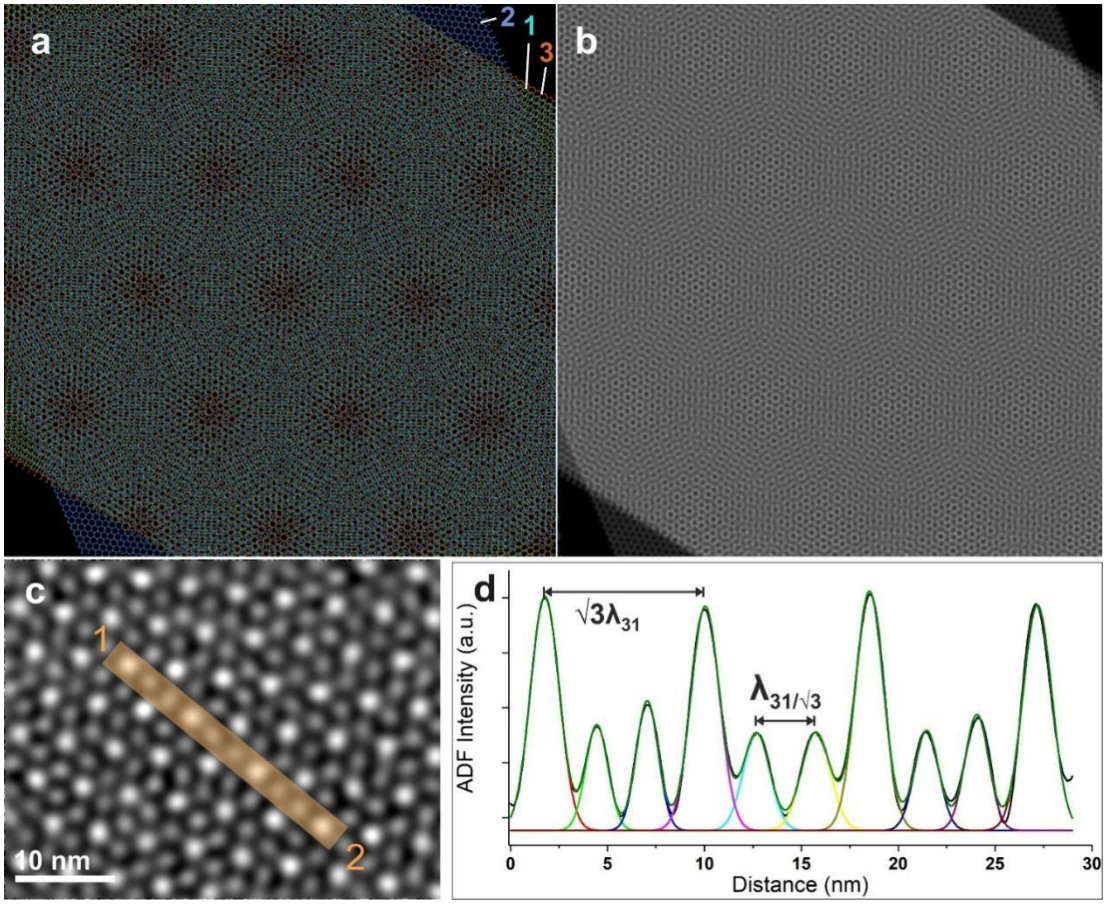


Figure C2. (a) Crystal model of a TTG, analogues to the backfolded trilayer graphene. 1 (top), 2 (middle), and 3 (bottom) denotes three layers. (b) Simulated ADF-STEM image based on panel b. (c) Filtered (remove low frequencies), inversed FFT, and gaussian blurred ADF-STEM image from fig. 5.4d, showing two moiré patterns M_{31} (brighter spots) and $M_{31}/\sqrt{3}$ (smaller, dimmer spots). Boxed region indicates where line profile was measured (from 1 to 2). (d) Fitted intensity line profile measured from panel c. High peaks indicate signal from M_{32}, lower twin peaks indicate signal from $M_{31}/\sqrt{3}$.

Appendix D

Supplementary Information for Chapter 6

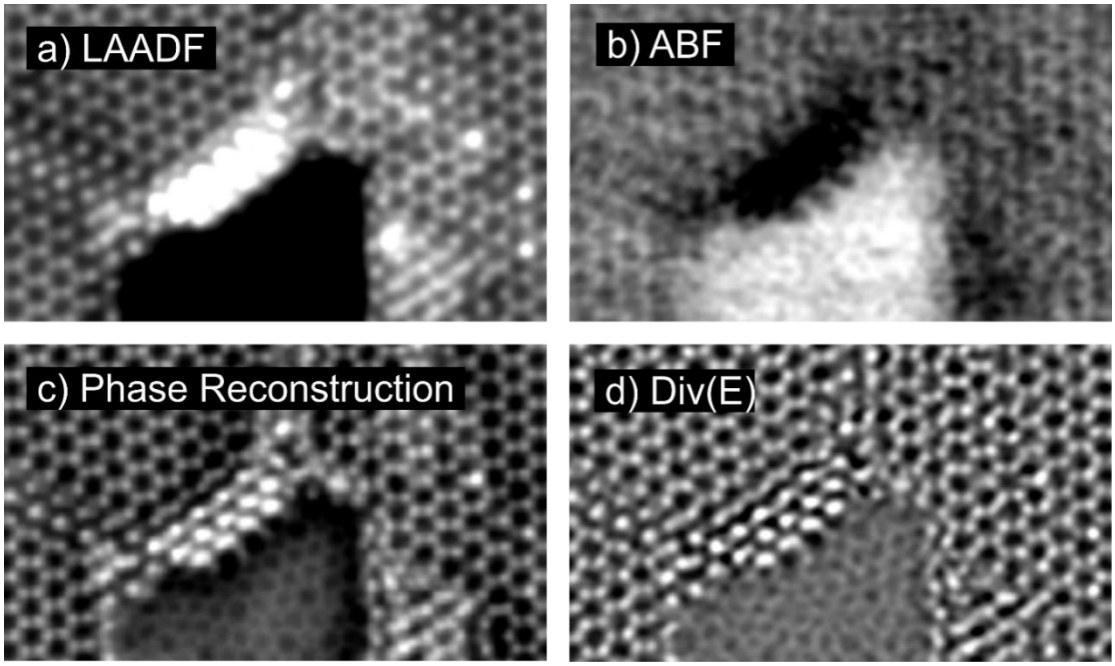


Figure D1. MoS_2 lattice hole with carbon contamination in several reconstruction modes from a 4D data set. Scale bar indicates 1 nm.

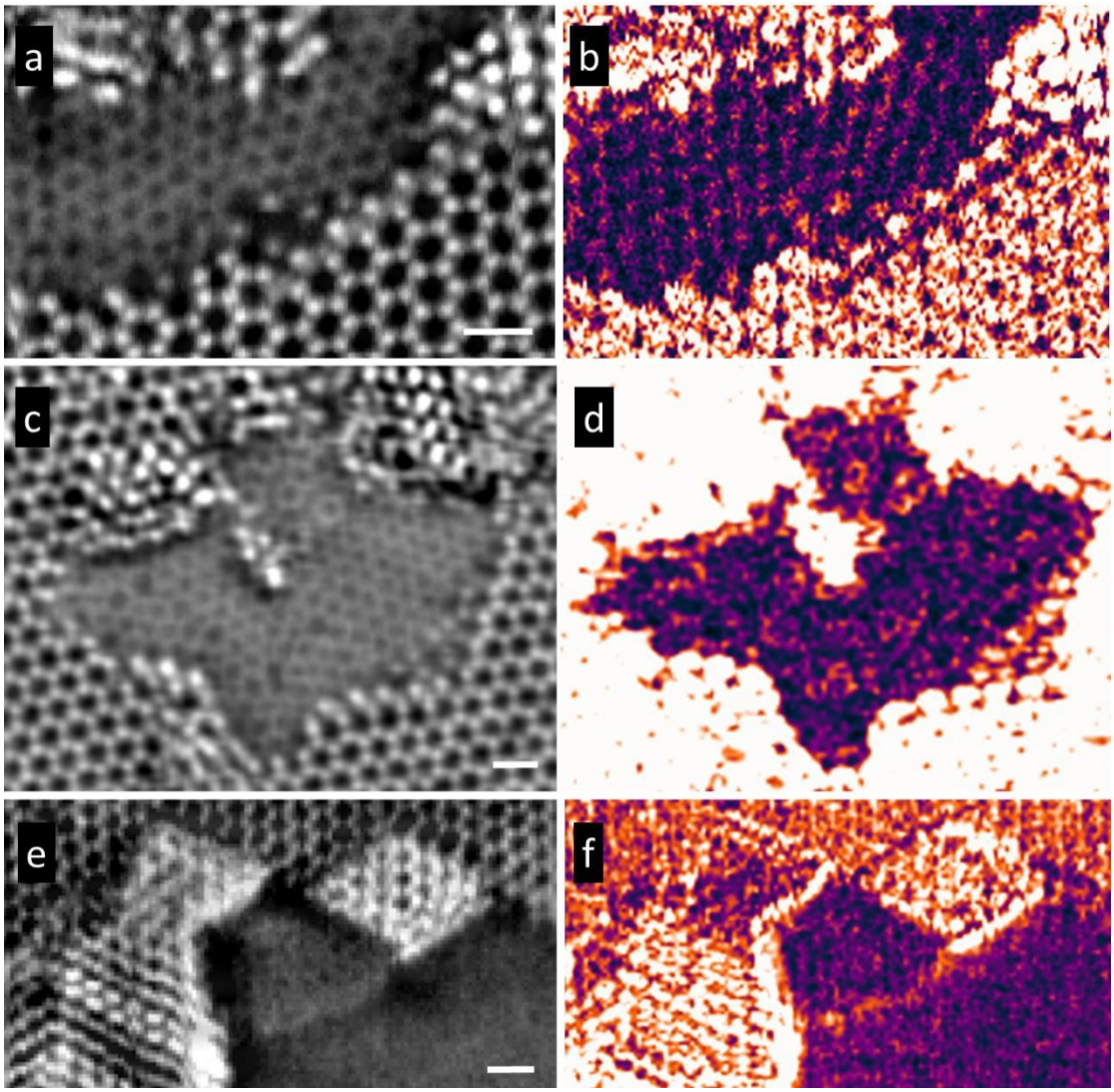


Figure D2. Repetitive capturing of carbon lattice within MoS_2 hole. (a), (c) and (e) Ptychographic phase images and (b), (d) and (f) corresponding CoM shift reconstructed from 4D-STEM data set. Scale bars in (a), (c), and (e) indicate 0.5 nm and applies to corresponding electric field map.

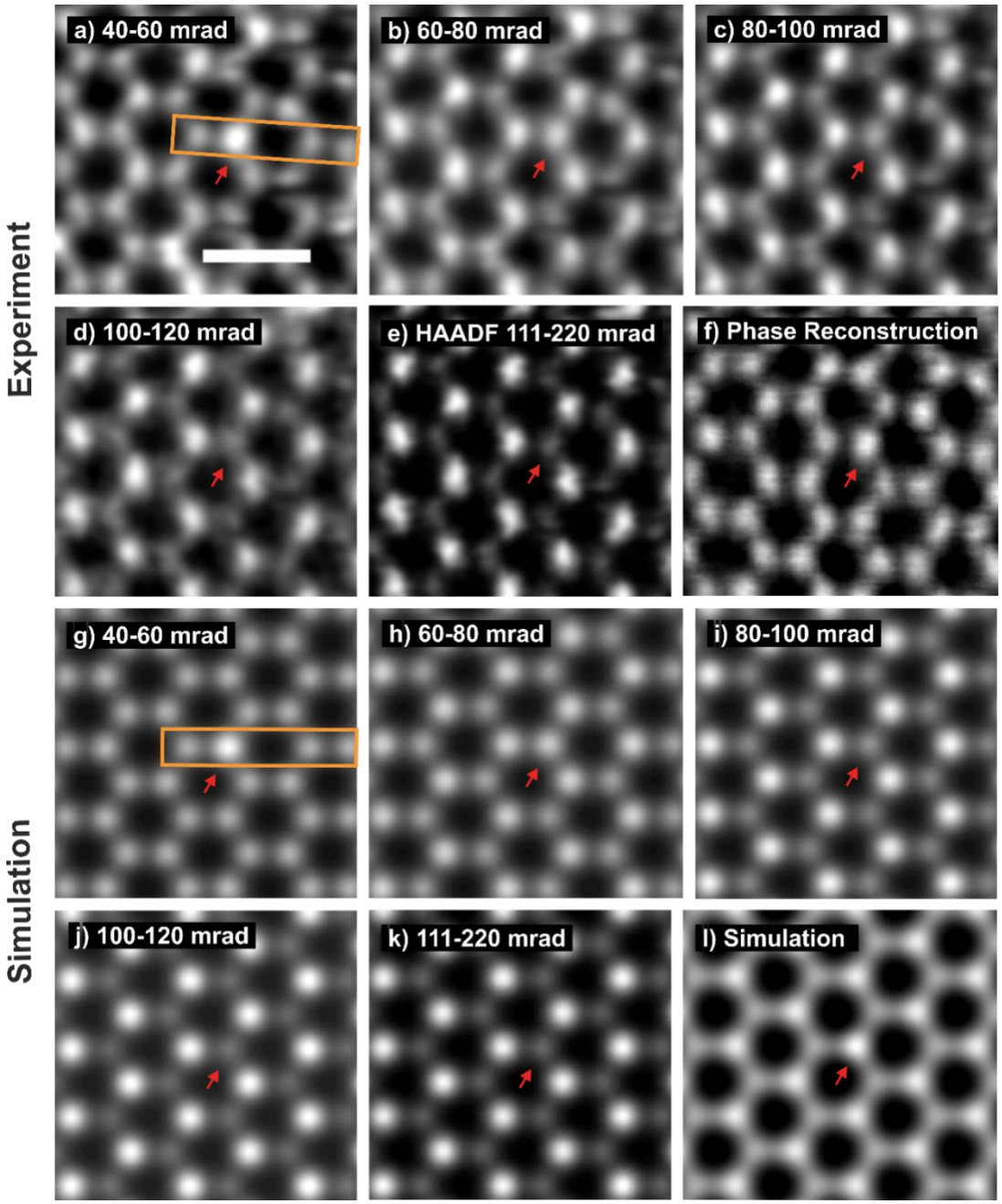


Figure D3. (a-d) Series of ADF-STEM images reconstructed with increasing annular detector collection angles from the same 4D-STEM data set (as in fig. 6.6). (e) Simultaneous HAADF-STEM image recorded using the conventional ADF detector. (f) corresponding phase reconstruction. (g-k) Simulated ADF-STEM images with increasing annular detector collection angles and simulated phase contrast image both based on the crystal model in fig. 6.6d. Red arrows indicate an adatom at a S site, scale bars indicate 0.5 nm and apply to (a-l).

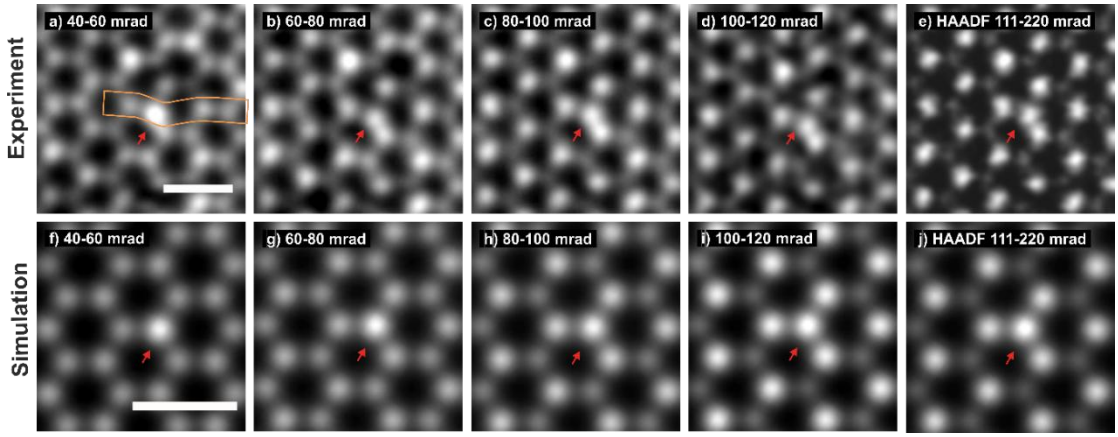


Figure D4. (a-d) ADF-STEM images reconstructed with increasing annular detector collection angles from the same 4D-STEM data set (as in fig. 6.7). (e) Simultaneous HAADF-STEM image recorded using the conventional ADF detector. (f-j) Simulated ADF-STEM images with increasing annular detector collection angles based on the crystal model in fig. 6.7d. Red arrows indicate an adatom at a S site, scale bars indicate 0.5 nm and apply to (a-e) and (f-j) respectively.

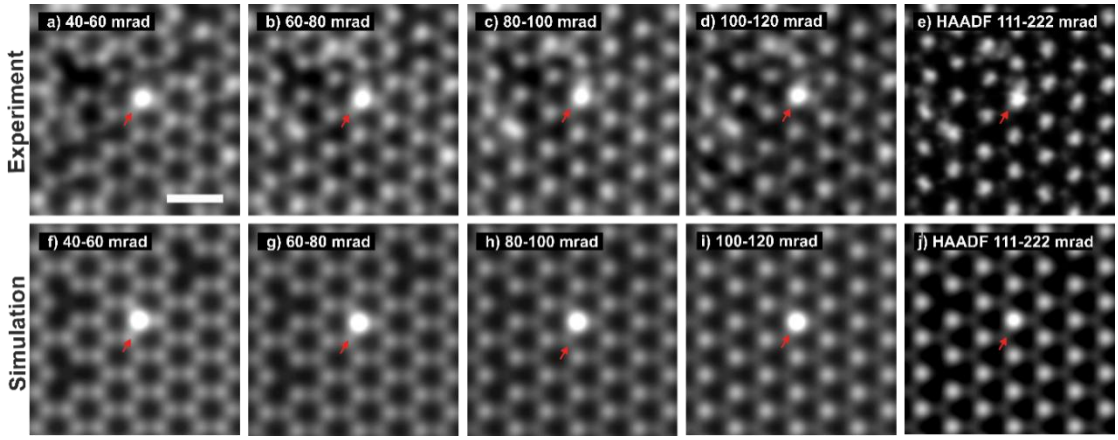


Figure D5. (a-d) Series of ADF-STEM images reconstructed with increasing annular detector collection angles from the same 4D-STEM data set (as in fig. 6.8). (e) Simultaneous HAADF-STEM image recorded using the conventional ADF detector. (f-j) Simulated ADF-STEM images with increasing annular detector collection angles based on the crystal model in fig. 6.8d. Red arrows indicate an adatom at a S site, scale bars indicate 0.5 nm and apply to (a-j).

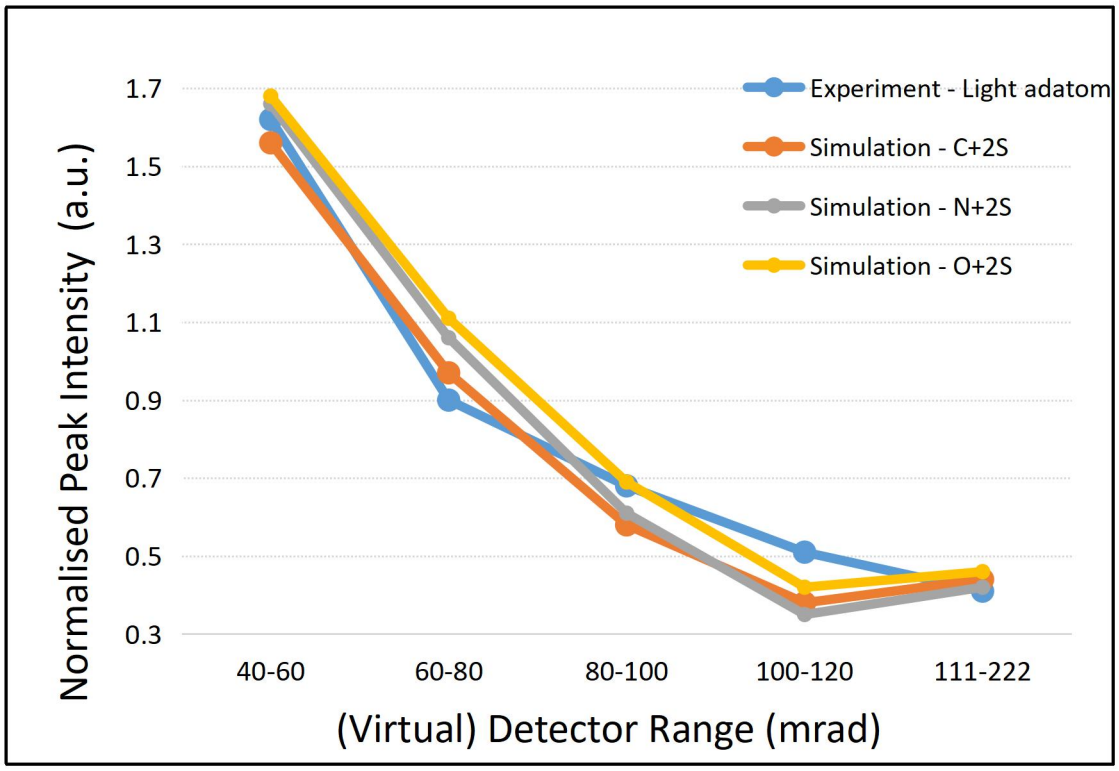


Figure D6. Normalised experimental and simulated peak intensities of a light adatom at a double-S site (intensities were normalised to that of the closest Mo atom), showing cases of C, N and O adatoms respectively. Experimental data is taken from Fig. 6.6 as a function of (virtual) detector range.

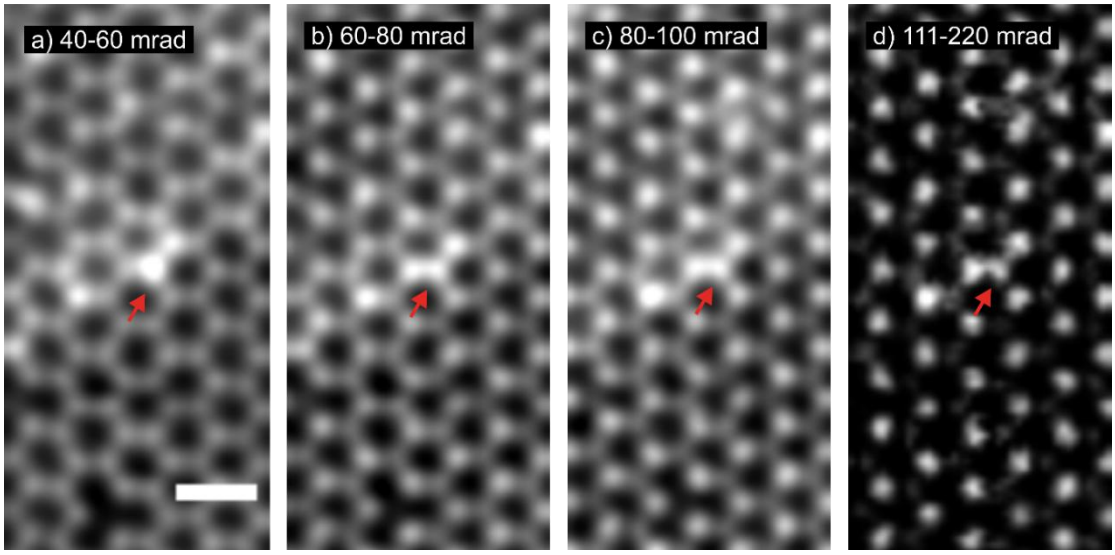


Figure D7. Surface adatom (indicated by red arrows) on a MoS_2 lattice with carbon contamination in several reconstruction modes taken from a 4D data set. The carbon contamination appears as brighter contrast in the top half of the figure. Scale bar indicates 0.5 nm and applies to (a-d).